The Pennsylvania State University

The Graduate School

Department of Mechanical Engineering

NONLINEAR ROBUST CONTROL DESIGN FOR A HIGH-SPEED SUPERCAVITATING VEHICLE

A Dissertation in

Mechanical Engineering

by

Xiaofeng Mao

Submitted in Partial Fulfillment
of the Requirements
for the Degree of

Doctor of Philosophy

December 2010

The dissertation of Xiaofeng Mao was reviewed and approved* by the following:

Qian Wang
Associate Professor of Mechanical Engineering
Dissertation Advisor
Chair of Committee

Joseph F. Horn
Associate Professor of Aerospace Engineering

Christopher D. Rahn
Professor of Mechanical Engineering

Alok Sinha
Professor of Mechanical Engineering

Karen A. Thole
Professor of Mechanical Engineering
Head of Department of Mechanical Engineering

*Signatures are on file in the Graduate School

ABSTRACT

Considerable skin friction drag on the hull limits the speed that traditional underwater vehicles are capable of achieving. However, it is possible to design a vehicle such that the front of it, the *cavitator*, can induce and maintain a single gaseous cavity, referred to as *Supercavitation*. The cavity can envelop most of the vehicle so that only the cavitator and the partial rear control fins are in contact with the water. And, such a design, can thereby dramatically reduce the skin friction drag acting on the vehicle. Vehicles with this feature are called *High-Speed Supercavitating Vehicles* (*HSSVs*) and can achieve high speeds of up to 300 m/s compared with 40 m/s of traditional vehicles in water.

One of the biggest challenges for control designs comes from the nonlinearity in the modeling of the planing force, which forms during planing condition that occurs when the vehicle's tail penetrates the cavity. Though planing force can be used to counteract the force of gravity when there are no other actuators such as the cavitator and fins available, it could also cause limit cycle of the vehicle, that is, substantial oscillation of the vehicle can happen. In this dissertation, we consider the supercavitating vehicles that are equipped with cavitator and fins, and the objective of our control designs is to eliminate the undesirable planing force for the purpose of drag reduction, stabilize the vehicle and further achieve satisfactory tracking performance.

Besides nonlinearity, another research challenge caused by the planing force comes from its strong memory effect because supercavitation involves complicated physics in the cavity-vehicle interaction. Yet, it is difficult to accurately model the hydrodynamic forces of the control surfaces (cavitator and fins) in supercavitation.

Additionally, the planing force exhibits strong memory effect because the computation of the planing force depends on the cavity shape, which is a function of the vehicle's motion history. In the past few years, many important advances have been made in the modeling and control designs for supercavitating vehicles. However, very few studies have explicitly addressed how to handle the uncertainties in the system parameters, the hydrodynamic coefficients, and the size of the time-delay. In this dissertation, the author focuses on handling these uncertainties by exploring advanced robust control design methodologies.

This dissertation considers the pitch-plane motion control of a high-speed supercavitating vehicle. Control designs are based on two major nonlinear approaches: the sliding-model control and the Quasi-Linear-Parameter-Varying control (Quasi-LPV). The sliding-mode controller emphasizes robustness with respect to the uncertainties in the system parameters and the hydrodynamic coefficients. The proposed Quasi-LPV formulation of the nonlinear supercavitating vehicle and the resulting H_∞ control provide performance optimization and also address the time delay due to the cavity-vehicle iteration. Simulations of different model-controller configurations provide insight into the robustness capabilities of the controllers.

In order to better understand the benefits that accrue from including the planing force memory effect into the control design, two delay-dependent Quasi-LPV controllers are compared with a Quasi-LPV controller based on a simplified non-time-delay model. Insight is thereby gained especially by comparing pitch-angle tracking performance using constrained control inputs.

Given that only a partial set of state variables are measurable, a high-gain observer is designed to estimate the state variable that is not directly available for feedback. The high-gain observer is selected because it is robust to uncertainties in modeling the nonlinear functions. In addition, each controller is also evaluated in terms of the impact of sensor measurement noise on closed-loop system performance.

TABLE OF CONTENTS

LIST OF FIGURES

LIST OF TABLES

NOMENCLATURE

R = radius of cylindrical section, m

R_n = radius of the cavitator, m

R_c = the cavity radius at the planing location, m

$\dot{R}_c$ = contraction rate of the cavity radius, m/s

R' = normalized difference between cavity and body diameter, dimensionless

h' = normalized immersion, dimensionless

ρ_b = vehicle density, kgm^{-3}

ρ = fluid (water) density, kgm^{-3}

m = ratio of ρ_b to ρ, dimensionless

m_v = vehicle mass, kg

F_{cav} = cavitator hydrodynamic force, N

F_{fin} = fin (elevators) hydrodynamic force, N

F_{grav} = gravity force, N

F_{plane} = planing force, N

F_{plane}^{z} = z-component of F_{plane}, N

F_{plane}^{Λ} = normalized planing force, ratio of F_{plane}^{z} to $\pi\rho mR^2L$, dimensionless

n = effectiveness of fins relative to the cavitator, dimensionless

I_{yy} = moment of inertia relative to the body-fixed reference frame, kgm^2

x_g = the location of the center of gravity in the body-fixed reference frame, m

V = forward speed, m/s

z = vehicle depth in the water at the cavitator center, m

θ = pitch angle of the vehicle, rad

w = vertical speed of cavitator center in the body-fixed reference frame, m/s

q = pitch rate, rad/s

F_{bz} = z-axis total force in the body-fixed reference frame, N

M = total moment at the center of pressure of the cavitator, Nm

α_c = cavitator angle of attack, rad

α_f = fin angle of attack, rad

α_{plane} = angle of attack at the planing location, rad

δ_c = cavitator deflection angle (counter-clockwise direction is positive), rad

δ_f = fin deflection angle (counter-clockwise direction is positive), rad

σ = cavitation number, a measure of the tendency of cavity to occur, dimensionless

C_{x0} = drag coefficient of cavitator at zero angle of attack, dimensionless

C_x = drag coefficient of cavitator, $C_{x0}(1+\sigma)$, dimensionless

ACRONYMS

HSSV	high-speed supercavitating vehicle
LPV	linear parameter varying
QLPV	quasi linear parameter varying
SC	saturation compensation
UC	unlimited control
SMC	the sliding-mode controller
QLPVHC	the quasi-LPV H_∞ controller
DNHC	the delay-dependent nominal LPV-H_∞ controller
DRHC	the delay-dependent robust LPV-H_∞ controller
BEM	boundary element method
CFD	computational fluid dynamics
LMI	linear matrix inequality

ACKNOWLEDGEMENTS

I wish to thank my advisor, Professor Qian Wang, for her guidance and patience throughout my study at Pennsylvania State University. Her assistance and encouragement during the preparation of this dissertation is especially appreciated. I am also grateful and indebted to all of my labmates, for inspiration and enlightening discussions on a wide variety of topics.

I thank my other committee members, Professor Joseph F. Horn, Professor Christopher D. Rahn and Professor Alok Sinha for their insightful commentary on my work.

Finally, I am indebted to my family who provided so much encouragement and support at every step of the way.

Chapter 1

Introduction

1.1 Introduction to Supercavitating Vehicles

It is highly desirable for many applications, underwater transportation and torpedoes among them, that underwater vehicles are capable of traveling at a very high speed. However, limited by the considerable drag due to skin friction on the hull, traditional underwater vehicles can travel at up to 40 m/s only and thus cannot meet performance requirements of these applications. Water produces up to 1,000 times more friction drag than air does [3]. Therefore, streamlining the hull, improving the propulsion system, or taking both these steps, will not render a vehicle capable of achieving significantly higher speed.

However, when a vehicle moves through water at a sufficiently high speed, as the fluid pressure drops locally below a level that can sustain the liquid state, cavitation bubbles appear at the trailing edges of the body's sharp corners [1, 3, 4]. If the speed increases, bubbles gather and form a single low-density gaseous cavity that envelops the entire vehicle. This hydrodynamic process in which an undersea body becomes entirely contained in a layer of gas is called *supercavitation*. Therefore, when supercavitation is applied to the design and control of underwater vehicles (known as *supercavitating vehicles*), they achieve extremely low drag and are thus able to reach a very high speed [1, 3, 4].

Fig. 1-1 shows a schematic diagram of a supercavitating vehicle. When a supercavitating vehicle travels through water above a certain speed limit, the *cavitator* at the vehicle's nose induces a gaseous cavity, known as a *supercavity*. This supercavity contains the vehicle's body, with the exception of the control surfaces such as the cavitator and the small outer portion of the fins and it separates from the surrounding water. As a result, the skin friction drag is substantially reduced to be almost negligible, which allows the supercavitating vehicle to achieve high-speed performance.

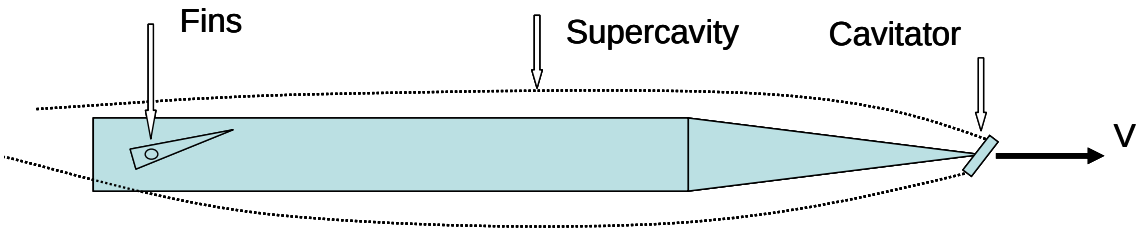

Fig. 1-1: Schematic diagram of a supercavitating vehicle.

Several supercavitating high-speed bodies have already been developed, e.g., the Rapid Airborne Mine Clearance System (RAMICS), the Adaptable High-speed Undersea Munitions (AHSUM) and the Russian Shkval [10]. The first two are uncontrolled small-range supercavitating projectiles. The RAMICS targets near-surface mines and is fired from a gun carried by a helicopter and travels in both air and water. The AHSUM, which targets incoming torpedoes, is fired from a submerged gun carried by ships and submarines and travels underwater at extremely high speed (~1500 m/s) [16]. The Shkval, developed in 1977, is considered the foremost example of supercavitating torpedo design,

and has been reported to attain underwater speeds in the order of 100 m/s. However, the Shkval lacks control surfaces, which are desirable for balance and control.

1.2 Planing Force due to Cavity-vehicle Interaction

As shown in Fig. 1-1, the aft end of the vehicle may be forced into contact with water by the weight of the vehicle or by initial perturbations in the vehicle's velocity. When contact happens, a large restoring force will bounce the aft end back into the cavity in a very short time, due to the large velocity difference between the vehicle and the surrounding water. The restoring force is always referred to as the *planing force*. This cavity-vehicle interaction can be described according to two basic modes: tail-slap and planing. During tail-slap conditions, the vehicle undergoes an oscillatory motion with periodic impacts with the cavity, whereas during planing the vehicle comes into contact with the lower internal surface of the cavity [16]. In the planing mode, the planing force may replace the fins in order to balance the vehicle. By doing so the planing force supports the vehicle's aft end and thus improves maneuverability for which the fins might not be needed. However, the planing force also leads to undesired increased drag and even stable nonlinear oscillations (limit cycles) under certain conditions [1].

The planing force shows a strong memory effect. Note that the cavity is formed by numerous small bubbles induced at the trailing edge of the cavitator so that the cavity shape is a function of the vehicle's motion history [18]. The magnitude of the planing force depends on the cavity shape, as the cavity shape impacts both the immersion depth

of the aft end and the planing angle of attack. More detailed description and modeling of the memory effect of the planing force will be given in Chapter 2.

1.3 Related Research

Research on supercavitating vehicles can be traced back as early as 1900s. Early stages of research mainly focused on the modeling and dynamic analysis for supercavitation and supercavitating vehicles. In the past several years, considerable research effort has been dedicated to developing control design methodologies, and guidance and control strategies for supercavitating vehicles.

1.3.1 Modeling

A. Cavity-vehicle Interaction

Reference 9 presents extensive experimental data to characterize hydrodynamic forces corresponding to different shapes of supercavitating vehicles, where lift and drag coefficients are plotted using table lookup values for shapes like disks, cones, ogives and wedges. The forces on the cavitators and fins of the supercavitating vehicle are also available in a CFD database provided in [2, 60]. This database contains values for coefficients of lift and drag for conical cavitators and wedge-shaped fins.

Based on the assumption that each cavity section expands independently of adjacent sections without viscous effects (or Logvinovich independence principle), the cavity radius and radial expansion rate are formulated in [59]. Moreover, the prediction

of cavity shape is conducted through modified forms of this formulation based on the experimental data in [59]. For the modeling of the planing force, the solution for a circular profile immersed in a plane and circular fluid surface can be found in [56] based on the inviscid flow theory. This solution is further extended by adding the skin friction force induced by fluid viscosity in [61]. Forces and centers of pressure are calculated in [61] for two special cases: circular cylinder planing on a flat surface, and circular cylinder planing on a curved surface.

Recently, two main methods have been widely used in the literature, Computational Fluid Dynamics (CFD) and the Boundary Element Method (BEM). The CFD approach requires a higher computation time; however, it is capable of capturing cavitation behavior more accurately than the BEM approach [51, 52]. The BEM approach has been improved to a level such that it can capture the overall cavity behavior at a much lower computational cost than the CFD approach, and it has been used to predict the behavior of supercavitating vehicles in various maneuvering conditions [2, 4, 50].

B. Control-oriented Modeling

Most of the research on control-oriented models has been focused on developing rigid body models to characterize the complex interactions between the vehicle and the surrounding cavity.

Dynamic behavior with tail-slaps is investigated in [5, 10] using a simplified model to describe the motion of the vehicle with respect to a horizontal cavity. However, this model does not account for the gravity of the vehicle and assumes that the vehicle

rotates about the nose. The results indicate that the tail-slap leads to a harmonic motion at frequencies that depend mostly on the vehicle's velocity in the considered configuration.

A benchmark control problem for a supercavitating torpedo is formulated in [1]. The authors also develop a simplified pitch-plane dynamical model for a torpedo. The model is linear when the planing force is not induced (or when the vehicle is not in contact with the cavity). Based on the solution for a circular profile immersed in a plane and circular fluid surface in [56], a formula to calculate the planing force is also proposed in [1]. The formula is based on the assumption that the centerline of the cavity is always along the velocity direction of the cavitator instead of being dependent on the vehicles' motion history. Thus, this model offers a time-independent approximation form of the planing force.

A more sophisticated model of the fins is used in [4], such that the hydrodynamic forces and moments acting on the fins are functions of dimensionless fin immersion and the angle of attack. This is unlike the model in [1], which assumes the relative effectiveness of the fins to be a constant value. In [4], the fin functions are nonlinear and their values are available in lookup tables, which are computed based on a fully three-dimensional BEM analysis supplemented with a viscous drag correction for a specific wedge-shaped fin. For the planing force, the authors emphasize the impact of the memory effect on system behavior but do not give a mathematical model to describe the memory effect explicitly.

As discussed in [12, 16, 17], neglecting the cavity-vehicle memory effect could substantially degrade the control performance of a supercavitating vehicle. As an extension to [1], the model proposed in [12, 18] redefines the planing condition and

offers a delay-dependent model that takes into account the memory effect of the cavity-vehicle interaction. In these two references, the vehicle model is described as a switched, bimodal system in which the cavity boundary, as the switching surface, is delay-dependent.

1.3.2 Control Design Methodologies and Simulations

A state feedback controller that uses only cavitator feedback is presented in [1]. Because the weight of the aft part of the body is not supported, gravity forces the body outside the cavity so that the response rapidly stabilizes to a limit cycle. A feedback linearization controller that uses both cavitator and fins feedback is also designed in [1], which removes the oscillation in the vertical speed. However, in general, feedback linearization is not robust with respect to system uncertainties.

In [4], a Linear Quadratic Regulator (LQR) based feedforward-feedback control is designed for a straight and level flight and a bank-to-turn maneuvering. Trajectory stability and dynamic behavior is investigated. The results show that the system eigenvalues strongly depend on the type of afterbody support (fins or planing force), and the proposed controller eliminates the most undesirable behavior in either case.

A switching controller that switches between two LQR controllers is presented in [11]. One of the LQR controllers is designed for a linear model with the planing force, and the other is for a linear model without the planing force. As a follow-up to [11], the same authors presented in [12, 13] another switching control law between feedback

linearization controllers; this law is designed for models with and without planing force and is based on the delay-dependent planing force model proposed in [12, 18].

In [14], several inner-loop controllers that provide absolute stability for the nominal supercavitating system are designed by modeling the planing force as sector-bounded uncertainties. The study offers a comparison between a switching feedback control and a backstepping controller in terms of the achieved region of attraction and magnitude of the needed control effort.

Based on a strong assumption that the cavity is fixed and the vehicle is situated symmetrically in the cavity, the authors in [15] designed an LQR controller for a linearized model to achieve pitch rate and roll rate controls without considering the planing force. The robustness analysis of the LQR controller is carried out by calculating the gain and phase margins.

In [12] and [18], the delay-dependent model is used in control designs to take into account the memory effect of the cavity-vehicle interaction. The design controllers consist of a dynamic-inversion controller and a pole-placement or model-predictive-control outer-loop controller. Since the control designs are based on the assumption that the delay in the equations of motion can be directly cancelled, the control performance is sensitive to the imperfect knowledge of the delay, i.e., the system becomes unstable at error levels of approximately 15-20% in the time delay.

1.3.3 Trajectory Planning, Guidance and Control

Trajectory optimization computes maneuvers based on a set of requirements. Computing a maneuver is to determine the time histories of controls and the associated time histories of the states. The controls are optimized to minimize some cost function and yet satisfy a number of path and boundary conditions. There are essentially two alternative strategies used in the field of trajectory optimization: indirect methods and direct methods. The indirect methods give extremely accurate results but require a lot of effort to incorporate changes of a problem to existing solutions; in contrast, with direct methods, suboptimal solutions can be achieved without additional work for complicated mathematical analysis of each individual problem [3].

So far a few studies have been conducted on the trajectory optimization for the supercavitating vehicle. In [3], in-plane dive maneuvers and turn maneuvers are optimized with direct methods for two different types of objective functions, one involving minimization of control effort, and the other involving minimization of control velocity. The physical and operational requirements for the supercavitating vehicle are translated to constraints and bounds on the states and controls. In a developed simulator, the maneuverability of the vehicle is also studied by investigating its ability to avoid an infinitely long cylindrical obstacle.

A framework for the optimization of trajectories of supercavitating vehicles is presented in [57]. The general framework could be applied to a variety of other complex scenarios. Configuration parameters could be cast as design variables to be optimized together with the maneuvers. Representative three dimensional maneuvers involving

dives, turns and target-tracking were investigated with direct methods. It should be noted that the memory effect from cavity-vehicle interaction is not considered.

Featuring time delays on the states of the system, a mathematical model governed by a particular class of delay differential equations is formulated in [58]. The optimal control problem is solved using a novel direct multiple shooting approach which properly handles conditions dictated by the delay differential equation formulation. Dive maneuvers and turn maneuvers are used to demonstrate the effectiveness of the proposed methodology. The results are also compared with those in [57] to highlight the difference and demonstrate the need for its formulation.

1.4 Motivations and Objectives

Supercavitation involves complicated physics in the cavity-vehicle interaction. And, the hydrodynamic forces of control surfaces (cavitator and fins) in supercavitation are hard to model accurately. Additionally, the planing force exhibits strong memory effects, as the computation of the planing force depends on the cavity shape, which is a function of the vehicle's motion history. In the past few years, many important advances have been made in modeling and control designs for supercavitating vehicles. However, few studies of control designs explicitly handle uncertainties in terms of system parameters, hydrodynamic coefficients, or the size of the time delay. The objective of this dissertation is to establish a way to handle these uncertainties by exploring advanced robust control design methodologies.

Following most of the control design literature, the dissertation considers the pitch-plane motion control of a high-speed supercavitating vehicle. Although the planing force can be used to counteract the force of gravity and improve maneuverability, in this dissertation, we consider that the control actuators such as cavitator and fins are available, the objective of control designs herein is to remove the planing force as possible for the purpose of drag reduction, stabilize the vehicle, and further achieve satisfactory tracking performance in the presence of uncertainties.

The main contributions of the dissertation are as follows:

- Control designs based on two major nonlinear approaches are developed in this dissertation: the sliding-model control and the Quasi-Linear-Parameter-Varying control (Quasi-LPV). The sliding-mode controller emphasizes robustness with respect to the uncertainties in the system parameters and hydrodynamic coefficients. The proposed Quasi-LPV formulation of the nonlinear supercavitating vehicle and the resulting H_∞ control optimizes performance and also addresses the time delay due to the cavity-vehicle iteration. Simulations of different model-controller configurations provide insight into the robustness capabilities of the controllers.
- To better understand the benefits that accrue from including planing force memory effect in the control design, the dissertation compares two delay-dependent Quasi-LPV controllers with a Quasi-LPV controller that is designed based on a simplified non-time-delay model. Significant insight is thereby gained

especially by comparing pitch-angle tracking performance using constrained control inputs.

- Since only a partial set of state variables are measurable, the dissertation offers a high-gain observer designed to estimate the state variable that is not directly available for feedback. The high-gain observer is selected, as it is robust to uncertainties in modeling nonlinear functions. In addition, each controller is evaluated in regard to the impact of sensor measurement noise on closed-loop system performance.

1.5 Organization of the Dissertation

Following this introductory chapter, Chapter 2 presents the equations that govern the pitch-plane dynamic behavior of a supercavitating vehicle, and introduces the two major models used for control designs in this dissertation: the Benchmark Model and the Time-Delay Benchmark Model. The difference between these two models lies in the characterization of the planing force between the vehicle and the cavity: the Time-Delay Benchmark Model takes into the memory effect of the cavity-vehicle interaction.

Chapter 3 describes a sliding-mode control design based on the Benchmark Model, in which stabilization and tracking problems are solved by designing sliding manifolds that take tracking trajectories into account. Since the structured uncertainties of the model are taken into account in designing the sliding-mode controller, the closed-loop systems implemented with the controller have provable robust stability subject to the assumed uncertainties in the system parameters and hydrodynamic coefficients. The

sliding-model controller is further evaluated by using the Time-Delay Benchmark Model. As one state variable may not be directly measurable for feedback control in practice, a high-gain observer is designed to estimate the particular state in terms of output measurement. Chapter 3 presents a detailed description of the high-gain observer design.

In Chapter 4, we reformulate the Benchmark Model into a Quasi-LPV form, and then design an LPV H_∞ controller. Note that the planing force is the only nonlinear function in the Benchmark Model. We recast the expression of the planing force as an affine function of a scheduling variable, which is defined as a function of part of the state variables of the supercavitating vehicle model. This leads to the reformulation of the Benchmark Model into a Quasi-LPV system. The resulting LPV H_∞ controller is designed by solving a set of linear matrix inequalities (LMIs) that are derived to optimize quadratic H_∞ performance.

By extending the widely cited Benchmark Model for the pitch-plane dynamics of a supercavitating vehicle, references [12] and [18] propose the Time-Delay Benchmark Model, which includes the delay-dependent interaction of the supercavitating vehicle and the cavity. Based on this new model, in Chapter 5, we develop delay-dependent controllers that explicitly address the cavity memory effect of the supercavitating vehicle dynamics. The pitch-plane dynamics of the supercavitating vehicle are first reformulated as a time-delay Quasi-LPV system, and then delay-dependent H_∞ controllers are developed. Simulations have been conducted for both initial and tracking responses to evaluate the performance and robustness of the proposed delay-dependent controllers.

The simulation results in this chapter are compared with those in Chapter 4 to highlight the benefits by handling the memory effect explicitly.

It is a well-known concern regarding the performance of high-gain observers in the presence of measurement noise. At the end of Chapters 3, 4 and 5, we present simulations that show how the high-gain observer behaves for each designed controller under the sensor measurement noise. In general, letting the eigenvalues of the dynamic matrix of estimation error go farther left on the left half plane will reduce the state estimation error in the absence of noise, but it will also amplify the noise. Therefore, an appropriate set of eigenvalues is needed to achieve the balance between minimizing the state estimation error and minimizing the error bound due to the measurement noise.

Finally, Chapter 6 presents concluding remarks and recommendations for future research.

Chapter 2

Modeling of Supercavitating Vehicles

The current literature on the control of supercavitating vehicles offers three main models [1, 4, 18] to compute the forces and moments of the cavitator and fins, as well as the planing force and moment. For convenience, models from [1], [18], and [4] will be referred to as the Benchmark Model, the Time-Delay Benchmark Model, and the High-Fidelity Model, respectively.

The Benchmark Model is a two degrees-of-freedom (DOF) longitudinal axis model that is linear when the planing force is not induced (or when the vehicle is not in contact with the cavity). Based on the solution for a circular profile immersed in a plane and circular fluid surface in [56], reference [1] proposes a formula to calculate the planing force. The assumption of the formula is that the centerline of the cavity is always along the velocity direction of the cavitator instead of being dependent on the vehicle's motion history. Thus, a time-independent approximation form of the planing force is used in the Benchmark Model. The Time-Delay Benchmark Model from [18] is relatively new, and the only difference from the Benchmark Model lies in the planing force. The Time-Delay Benchmark Model redefines the planing condition by taking into account the memory effect of the cavity-vehicle interaction. In keeping with most of the recent work, e.g., [1, 3, 6-8, 14, 15], the control designs given in Chapters 3 and 4 are based on the Benchmark Model from [1]. We further address the memory effect explicitly in the control designs given in Chapter 5, based on the Time-Delay Benchmark Model.

In this chapter, the Benchmark Model will be introduced first, and then the Time-Delay Benchmark Model with delay-dependent planing force will be presented. At the end of the chapter, the High-Fidelity Model will be briefly introduced through a comparison with the Benchmark Model. In addition, other effort dedicated to the structural modeling and buckling analysis of the supercavitating vehicle body is also briefly introduced.

2.1 Benchmark Model

As shown in Fig. 2-1, the Benchmark Model considers the longitudinal dynamics of a supercavitating vehicle expressed in a body-fixed reference frame (the same as that used in [1]). This frame originates at the cavitator's center of pressure, with the x-axis pointing forward along the vehicle axis of symmetry, y-axis to the starboard and z-axis pointing down. It is assumed that the vehicle body studied in [1] consists of a cylindrical section of length $2L/3$ and a conical section of length $L/3$, which approximates the shape of an actual HSSV, where L denotes the entire vehicle length.

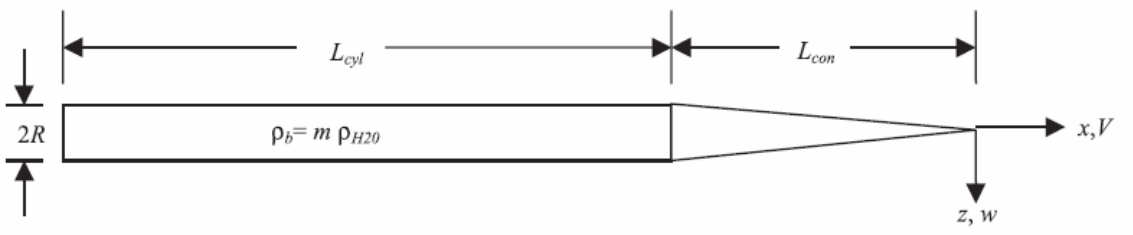

Fig. 2-1: Schematic diagram of the model showing reference frame and symbols [1].

2.1.1 Equations of Motion

Assuming that the body-axis forward speed V is constant, the equations of motion are given as follows:

$$m_v(\dot{w} - x_g\dot{q} - qV) = F_{bz} \tag{2.1}$$

$$I_{yy}\dot{q} = M + m_v x_g(\dot{w} - qV) \tag{2.2}$$

where $x_g\dot{q}$ in the force equation and $m_v x_g(\dot{w} - qV)$ in the moment equation are due to the origin of the reference frame specified at the cavitator's center of pressure. The dynamic equations can be rewritten in the following compact form:

$$\begin{bmatrix} m_v & -m_v x_g \\ -m_v x_g & I_{yy} \end{bmatrix} \begin{bmatrix} \dot{w} \\ \dot{q} \end{bmatrix} = qV \begin{bmatrix} m_v \\ -m_v x_g \end{bmatrix} + \begin{bmatrix} F_{bz} \\ M \end{bmatrix} \tag{2.3}$$

The kinematic equations in the inertial coordinates are given as,

$$\dot{z} = w\cos\theta - V\sin\theta$$
$$\text{or } \dot{z} = w - V\theta \tag{2.4}$$

with small angle approximations for trigonometric functions, and

$$\dot{\theta} = q \tag{2.5}$$

The system parameters in Eqs. 2.1-2.5 are given as follows:

$$m_v = \frac{7}{9}\rho_v \pi R^2 L = \frac{7}{9} m \rho \pi R^2 L \tag{2.6}$$

$$x_g = -\frac{17}{28} L \tag{2.7}$$

$$I_{yy} = I_{yy}(cone) + I_{yy}(cylinder) = \frac{11}{60}\rho_v \pi R^4 L + \frac{133}{405}\rho_v \pi R^2 L^3 \tag{2.8}$$

In Eq. 2.3, the body-axis force in the *z*-direction, F_{bz}, consists of z-components of the body-axis gravity force F_{grav}, the force of the elevator fin F_{fin}, the cavitator force F_{cav}, and the planing force F_{plane}; i.e.,

$$F_{bz} = F^z_{grav} + F^z_{fin} + F^z_{cav} + F^z_{plane} \tag{2.9}$$

where F^z_* denotes the z-component of force $*$. The body-axis pitching moment M consists of moments due to the gravity force M_{grav}, the elevator fin M_{fin}, and the planing force M_{plane}; i.e.,

$$M = M_{grav} + M_{fin} + M_{plane} \tag{2.10}$$

Each individual force and moment is described in the following sections.

2.1.2 Gravity Force and Moment

In the body-fixed reference frame, the *z*-component of the gravity force is

$$F_{grav}^{z} = m_v g \cos\theta \tag{2.11}$$

and the corresponding pitching moment (with respect to the center of pressure of the cavitator) due to gravity is,

$$M_{grav} = m_v g \cos\theta \cdot (-x_g) \tag{2.12}$$

2.1.3 Cavitator Force and Moment

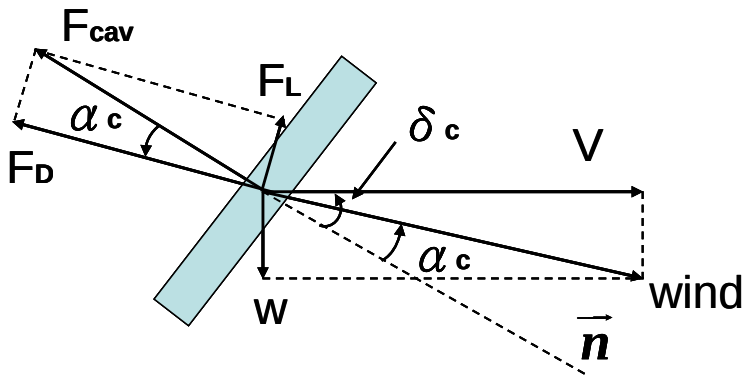

Figure 2-2: Hydrodynamic forces acting on the cavitator, where $\vec{n}$ denotes normal vector of the cavitator plane.

Considering a disk cavitator in this dissertation, the lift and drag forces acting on the cavitator are illustrated in Fig. 2-2. They are computed as follows:

$$F_L = \frac{1}{2}\rho V^2(\pi R_n^2)C_{x0}(1+\sigma)\cos\alpha_c \sin\alpha_c \qquad 2.13$$

$$F_D = \frac{1}{2}\rho V^2(\pi R_n^2)C_{x0}(1+\sigma)\cos^2\alpha_c \qquad 2.14$$

with the angle of attack α_c calculated as (note that δ_c is defined as positive in the counter-clockwise),

$$\alpha_c = \tan^{-1}(\frac{w}{V}) + \delta_c \qquad 2.15$$

Then, the body-axis *z*-component of the cavitator force is

$$\begin{aligned} F_{cav}^z &= F_L \cos(\alpha_c - \delta_c) - F_D \sin(\alpha_c - \delta_c) \\ &= \frac{1}{2}\rho V^2 \pi R_n^2 C_{x0}(1+\sigma)\cos\alpha_c \sin\delta_c \\ &\approx C_{cav}\delta_c \end{aligned} \qquad 2.16$$

where $C_{cav} = \frac{1}{2}\rho V^2 \pi R_n^2 C_{x0}(1+\sigma)$ is referred to as the cavitator effectiveness in [1]. With respect to the center of pressure of the cavitator, the pitching moment due to the cavitator force equals zero.

Remark 2.1.1: It should be noted that the cavitator force in Eq. 2.16 is slightly different from that calculated in [1], where $F_{cav}^z \approx F_L \approx C_{cav}\alpha_c = C_{cav}(w/V + \delta_c)$. The formula proposed here is based on experimental results from [9], p. 2-24, Fig. 2-36, which are also referred to in [10]. The observation of experimental results for a disk cavitator is given as follows. For small angles of attack α_c, the force due to the fluid acting on the cavitator is directed along the cavitator's body axis, which is given by $\vec{n}$. If we consider the case in which $\delta_c = 0$, the cavitator disk plane will be perpendicular to the longitudinal axis of the vehicle; therefore, $\vec{n}$ will also be along the longitudinal axis of the vehicle. According to this observation, the overall fluid force acting on the cavitator

should be along the direction of $\vec{n}$, which suggests that the lift force component along the z-axis of the body-fixed axes should be zero.

2.1.4 Planing Force and Moment

As in [1], it is assumed that the planing force depends entirely on the vertical velocity. The normal pressure force at the transom of a supercavitating vehicle is computed as,

$$F_{plane}^{z} = -\pi\rho R_c^2 V^2 \sin(\alpha_{plane})\cos(\alpha_{plane})\cdot(\frac{1+h'}{1+2h'})\cdot[1-(\frac{R'}{h'+R'})^2] \qquad 2.17$$

$$M_{plane} = F_{plane}^{z} L \qquad 2.18$$

where the cavity radius R_c and its contraction rate $\dot{R}_c$, as well as the parameters h', R', and α_{plane} are defined in the following. First define

$$K_1 = \frac{L}{R_n}(\frac{1.92}{\sigma} - 3)^{-1} - 1 \qquad 2.19$$

$$K_2 = [1-(1-\frac{4.5\sigma}{1+\sigma})K_1^{40/17}]^{1/2} \qquad 2.20$$

Then, the cavity radius at the planing location and its contraction rate can be expressed as

$$R_c = R_n[0.82\frac{(1+\sigma)}{\sigma}]^{1/2}K_2 \tag{2.21}$$

$$\dot{R}_c = -\frac{20}{17}(0.82\frac{1+\sigma}{\sigma})^{1/2}V(1-\frac{4.5\sigma}{1+\sigma})K_1^{(23/17)}\Big/K_2(\frac{1.92}{\sigma}-3) \tag{2.22}$$

The parameters h' and R' in Eq. 2.17 are defined as,

$$R' = (R_c - R)/R \tag{2.23}$$

$$h' = \begin{cases} 0, & (R_c - R)/R > (L/R)\,|w/V| \\ (L/R)\,|w/V| - R', & otherwise \end{cases} \tag{2.24}$$

Note that $\dot{R}_c$ is not the derivative of R_c; instead, $\dot{R}_c$ is used to calculate the increase of the angle of attack due to the cavity radius contraction at the planing location. The angle of attack at the planing location is computed as,

$$\alpha_{plane} = \begin{cases} \tan^{-1}(\frac{w}{V}) - \tan^{-1}(\frac{\dot{R}_c}{V}) & \frac{w}{V} > 0 \\ \tan^{-1}(\frac{w}{V}) + \tan^{-1}(\frac{\dot{R}_c}{V}) & otherwise \end{cases} \tag{2.25}$$

2.1.5 Fin Force and Moment

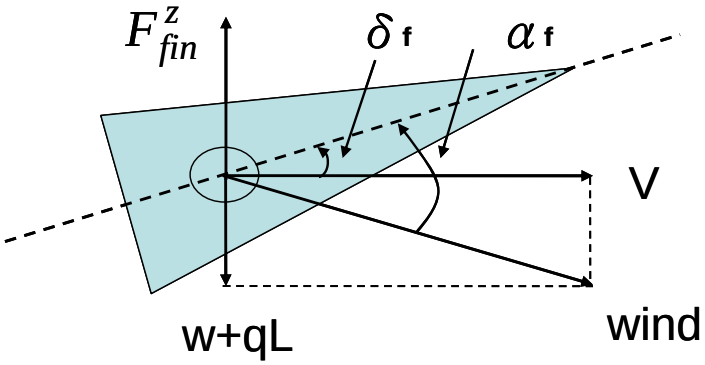

Figure 2-3: The z-component of the hydrodynamic force acting on the fins.

A simplified linear fin model is adopted in the Benchmark Model. Given that the cavitator force is defined in terms of the cavitator effectiveness C_{cav}, a parameter n, as defined in [1], denotes the effectiveness of fins relative to the cavitator, where effectiveness of fins represents the change of the *z*-component force in the body axis due to the unit change of the fin's angle of attack. Then, the *z*-component fin force shown in Fig. 2-3 and the fin-induced pitching moment are computed as,

$$F_{fin}^{z} = -nC_{cav}\alpha_f \qquad 2.26$$

$$M_{fin} = F_{fin}^{z} L \qquad 2.27$$

where α_f and δ_f denote the fin angle of attack and fin deflection angle, respectively. The fin angle of attack α_f can be calculated as,

$$\alpha_f \approx \tan^{-1}(\frac{w}{V}+\frac{qL}{V})+\delta_f \tag{2.28}$$

2.1.6 Final Equations of Motion

Plug all the forces and moments into Eqs. 2.3-2.5, and the final dynamic equations are given as follows,

$$\begin{aligned}
&\dot{z} = w - V\theta \\
&\dot{\theta} = q \\
&\begin{bmatrix} \frac{7}{9} & \frac{17}{36}L \\ \frac{17}{36}L & \frac{11}{60}R^2+\frac{133}{405}L^2 \end{bmatrix}\begin{bmatrix}\dot{w}\\ \dot{q}\end{bmatrix} = CV\begin{bmatrix} \frac{-n}{mL} & \frac{-n}{m} \\ \frac{-n}{m} & \frac{-nL}{m} \end{bmatrix}\begin{bmatrix}w\\ q\end{bmatrix} + V\begin{bmatrix} 0 & \frac{7}{9} \\ 0 & \frac{17}{36}L \end{bmatrix}\begin{bmatrix}w\\ q\end{bmatrix} \\
&\qquad\qquad + CV^2\begin{bmatrix} \frac{-n}{mL} & \frac{1}{mL} \\ \frac{-n}{m} & 0 \end{bmatrix}\begin{bmatrix}\delta_f\\ \delta_c\end{bmatrix} + F^{\wedge}_{grav} + F^{\wedge}_{plane}\begin{bmatrix}1\\ L\end{bmatrix}
\end{aligned} \tag{2.29}$$

where

$$F_{grav}^{\Lambda} = \begin{bmatrix} \frac{7}{9} \\ \frac{17}{36}L \end{bmatrix} g$$

$$F_{plane}^{\Lambda} = \frac{F_{plane}^{z}}{\pi \rho m R^2 L} \qquad 2.30$$

$$C = \frac{1}{2} C_x (\frac{R_n}{R})^2 = \frac{1}{2} C_{x0} (1+\sigma)(\frac{R_n}{R})^2$$

The dynamic equations can also be written in the following compact form for easy reference later in the dissertation.

$$\begin{aligned} &\dot{z} = w - V\theta \\ &\dot{\theta} = q \\ &M_I \begin{bmatrix} \dot{w} \\ \dot{q} \end{bmatrix} = A_I \begin{bmatrix} w \\ q \end{bmatrix} + B_I \begin{bmatrix} \delta_f \\ \delta_c \end{bmatrix} + F_{grav}^{\Lambda} + F_{plane}^{\Lambda} \begin{bmatrix} 1 \\ L \end{bmatrix} \end{aligned} \qquad 2.31$$

where

$$M_I = \begin{bmatrix} \frac{7}{9} & \frac{17}{36}L \\ \frac{17}{36}L & \frac{11}{60}R^2 + \frac{133}{405}L^2 \end{bmatrix},$$

$$A_I = CV \begin{bmatrix} \frac{-n}{mL} & \frac{-n}{m} \\ \frac{-n}{m} & \frac{-nL}{m} \end{bmatrix} + V \begin{bmatrix} 0 & \frac{7}{9} \\ 0 & \frac{17}{36}L \end{bmatrix} \qquad 2.32$$

$$B_I = CV^2 \begin{bmatrix} \frac{-n}{mL} & \frac{1}{mL} \\ \frac{-n}{m} & 0 \end{bmatrix}$$

Remark 2.1.2: When the planing force is not induced, Eq. 2.31 becomes a linear system after canceling out the gravity force part. Based on the vehicle configuration parameters as in Appendix D, the eigenvalues of the state matrix can be shown to be

$$\begin{aligned} \lambda_1 &= 0 \\ \lambda_2 &= 0 \\ \lambda_3 &= \text{-1.5468 +15.5218i} \\ \lambda_4 &= \text{-1.5468 -15.5218i} \end{aligned} \qquad 2.33$$

where the Jordan block for $\lambda = 0$ is of dimension 2, which means the open-loop system is unstable.

2.2 Time-Delay Benchmark Model

The planing force exhibits strong memory effects [4, 12], as the planing force computation depends on the cavity shape, which is a function of the vehicle's motion history. As discussed in [12, 16, 17], neglecting this cavity-vehicle memory effect could substantially degrade the control performance of a supercavitating vehicle. As a modification to the Benchmark Model, [12] and [18] redefined the planing condition and proposed a new planing force model that takes into account the memory effect of the cavity-vehicle interaction.

Due to the memory effect of the cavity-vehicle interaction, the immersion depth h' and planing angle α_{plane} are functions of both instant and delayed state variables, and they are remodeled as follows:

$$h' = \begin{cases} \frac{1}{R}\left[z(t) + \theta(t)L - z(t-\tau) + R - R_c\right] & \textit{bottom contact} \\ 0 & \textit{inside cavity} \\ \frac{1}{R}\left[R - R_c - z(t) - \theta(t)L + z(t-\tau)\right] & \textit{top contact} \end{cases} \quad 2.34$$

$$\alpha_{plane} = \begin{cases} \theta(t) - \theta(t-\tau) + \frac{w(t-\tau) - \dot{R}_c}{V} & \textit{bottom contact} \\ 0 & \textit{inside cavity} \\ \theta(t) - \theta(t-\tau) + \frac{w(t-\tau) + \dot{R}_c}{V} & \textit{top contact} \end{cases} \quad 2.35$$

with the following planing conditions,

$$\begin{cases} \textit{bottom contact} & \textit{if } R_c - R < z(t) + \theta(t)L - z(t-\tau) \\ \textit{inside cavity} & \textit{otherwise} \\ \textit{top contact} & \textit{if } R - R_c > z(t) + \theta(t)L - z(t-\tau) \end{cases} \quad 2.36$$

where $\tau = L/V$ represents the size of the time delay, and $\dot{R}_c$ denotes the contraction rate of the cavity at the planing location, as indicated in Eq. 2.22. With the new definition of h' and α_{plane}, the time-delayed planing force can be calculated using the same formula defined in Eq. 2.17.

2.3 Other Modeling Work

The High-Fidelity Model developed in [4] and related references [3, 11] is a

nonlinear six-DOF model, and shares the same modeling for the cavitator and planing force as the Benchmark Model. The major difference between the two models lies in the calculation of fin force F_{fin}. In the High-Fidelity Model, the hydrodynamic forces and moments acting on the fins are functions of dimensionless fin immersion and the angle of attack. This is different from the Benchmark Model that models the fin force as a linear function with respect to the angle of attack and assumes the fin effectiveness parameter as a constant. Based on a fully three-dimensional Boundary Element Method (BEM) analysis and supplemented with a viscous drag correction for a specific wedge-shaped fin, the nonlinear fin forces in [4] is computed and tabulated in lookup tables for various values of fin immersion and angle of attack.

When the drag force acts on the cavitator axially compresses the supercavitating vehicle body and increases approximately with the square of the vehicle's speed, the drag force may become very high and cause the body to buckle. The buckling condition has been identified as one of the limiting factors for the operating speed of supercavitating vehicles [54]. Hence, extensive work has been dedicated to the structural modeling and buckling analysis of the vehicle body [53, 54], in order to assess the structural safety limits and further extend the vehicles' operating range. Using a simple beam model to represent a supercavitating vehicle and larger diameter sections to represent stiffening rings in the structure, A Finite Element Model in [53] demonstrats how various configurations of these larger diameter sections affect cavity-vehicle interactions. A high-fidelity finite element model in [54] is created by making use of a cylinder model composed of shell elements to perform buckling analysis. The results in [54] indicate the effectiveness of the periodically placed circumferential stiffening rings in extending the

range of stable operating conditions by increasing the critical static buckling loads and reducing the extension of the regions corresponding to dynamic instability.

Chapter 3

Sliding-Mode Control for the Benchmark Model of Supercavitating Vehicles

3.1 Introduction

It is generally recognized that models are imprecise in practice and that this can have strong adverse effects on nonlinear control systems. The imprecision may come from unknown plant parameters or from a simplified representation of the system's dynamics. From a control point of view, modeling inaccuracies can be classified into two major kinds: structured (or parametric) uncertainties and unstructured uncertainties (or unmodeled dynamics) [21, 49]. The first kind often corresponds to insufficient knowledge of the terms actually included in the model, whereas the second kind often corresponds to purposefully underestimating the system order (such as model order reduction or linearization), which is convenient for dynamics analysis and control design. Robust controllers are designed to maintain stability and/or performance in the presence of uncertainties. For nonlinear systems, a robust controller typically comprises a nominal part called equivalent control, similar to feedback linearization or an inverse control law, and additional terms aimed at addressing model uncertainty [49].

Sliding-mode control is an important methodology for the robust control of nonlinear systems. It provides a systematic approach to maintaining stability and consistent performance in the presence of modeling imprecision, including structured and unstructured uncertainties. The methodology is based on the idea of picking up a sliding

manifold (or a well-behaved function of the tracking error), s, and then selecting a control law, such that s^2 remains a Lyapunov-like function of the closed-loop system, despite the presence of model inaccuracies and of disturbances [49]. Given the initial conditions, the problem of tracking is equivalent to that of satisfying the Lyapunov-like function (or sliding conditions); that is, by satisfying the Lyapunov-like function, the sliding manifold is guaranteed to be an attractive and invariant set. Furthermore, the sliding manifold will be reached in a finite time if initial conditions are off-reference signals. Once on the manifold, the tracking error tends exponentially to zero according to the manifold's definition. Thus, a typical motion under the sliding-mode control consists of (1) a reaching phase, during which trajectories start off the sliding manifold, moving toward it and reach it in finite time, followed by (2) a sliding phase, during which the motion is confined to the manifold. The dynamics of this system are represented by a reduced-order model [21]. If the control effort has no limit, arbitrary large disturbances or dynamic uncertainties can be tolerated in principle. Such a performance, however, is obtained at the price of extremely high control activity, e.g., the control laws contain a discontinuous switching part across the desired sliding manifolds. Due to imperfections in switching devices and delays, the discontinuous switching control could lead to the practical issue of chattering. Though this control chattering is acceptable in some specific applications, it is typically at odds with the presence of high-frequency unstructured dynamics, which the high-control activity may excite [49]. One approach to eliminating chattering is to use a continuous approximation of the discontinuous signum nonlinearity in switching control to achieve an effective trade-off between control bandwidth and tracking precision.

The sliding-mode control has been successfully applied to various applications such as robot manipulators, underwater vehicles, automotive transmissions and engines, high-performance electric motors, and power systems [49]. The success of these applications motivates us to apply the sliding-mode control to the supercavitating vehicle model with uncertainties.

In this chapter, we design a sliding-mode control for stabilization and tracking control based on the Benchmark Model. We will also address robustness with respect to parametric uncertainties in the system parameters and hydrodynamic coefficients. We start with the assumption that all state variables (z, θ, w, q) are available for state feedback. Later, we design a high-gain observer for the state variables that are not directly available via measurement. Simulation results for the combination of the sliding-mode controller with the high-gain observer will be shown. We first design the controller for stabilization and then for tracking, where tracking is transformed into a stabilization problem by redefining state variables and sliding manifolds. At the end of the chapter, we also evaluate our sliding-mode controller using the Time-Delay Benchmark Model, although the sliding-mode controller is not designed to deal with the memory effect of the cavity-vehicle interaction.

3.2 Stabilization

Define

$$\eta = \begin{bmatrix} z \\ \theta \end{bmatrix},\ \xi = \begin{bmatrix} w \\ q \end{bmatrix},\ \text{and } u = \begin{bmatrix} \delta_f \\ \delta_c \end{bmatrix} \tag{3.1}$$

then Eq. 2.29 becomes,

$$\dot{\eta} = A\eta + B\xi \tag{3.2}$$

$$\dot{\xi} = f(\xi,\eta) + g(\xi,\eta)u \tag{3.3}$$

where

$$A = \begin{bmatrix} 0 & -V \\ 0 & 0 \end{bmatrix},\ B = \begin{bmatrix} 1 & 0 \\ 0 & 1 \end{bmatrix} \tag{3.4}$$

$$f(\xi,\eta) = M_I^{-1} \cdot (A_I \begin{bmatrix} w \\ q \end{bmatrix} + F_{grav}^{\Lambda} + F_{plane}^{\Lambda} \begin{bmatrix} 1 \\ L \end{bmatrix}) \tag{3.5}$$

$$g(\xi,\eta) = M_I^{-1} \cdot B_I \tag{3.6}$$

with F_{grav}^{Λ}, F_{plane}^{Λ}, M_I, A_I, and B_I defined in Eq. 2.30 and Eq. 2.32.

Noting that in Eq. 3.3, both $f(\xi,\eta)$ and $g(\xi,\eta)$ could be uncertain due to

variations in mass and modeling errors in hydrodynamic coefficients. Thus by separating the nominal and uncertain parts of $f(\xi,\eta)$ and $g(\xi,\eta)$, we have

$$f(\xi,\eta) = \hat{f}(\xi,\eta) + \tilde{f}(\xi,\eta) \tag{3.7}$$

$$g(\xi,\eta) = \hat{g}(\xi,\eta) + \tilde{g}(\xi,\eta) \tag{3.8}$$

where $\hat{*}$ and $\tilde{*}$ denote the nominal and uncertain parts respectively. Then Eq. 3.3 becomes

$$\dot{\xi} = \hat{f}(\xi,\eta) + \tilde{f}(\xi,\eta) + \hat{g}(\xi,\eta)u + \tilde{g}(\xi,\eta)u \tag{3.9}$$

For the η dynamics in Eq. 3.2, the ξ can be viewed as a virtual control, and we can design this virtual control $\xi = \phi(\eta)$ to stabilize the η dynamics; one easy choice for the $\phi(\eta)$ is a state feedback $K\eta$ where the 2×2 design parameter K satisfies that $(A+BK)$ is asymptotically stable. Consequently, we specify the sliding manifold as $s = \xi - K\eta$. Note that if $s \to 0$, $\xi \to K\eta$, and then $\dot{\xi} = (A+BK)\xi$, which gives $\xi \to 0$ asymptotically and $\eta \to 0$ asymptotically. Next, we only need to consider the dynamics of the sliding manifold s.

Taking the derivative of the sliding manifold, we have

$$\begin{aligned} \dot{s} &= \dot{\xi} - K\dot{\eta} \\ &= \hat{f}(\xi,\eta) + \tilde{f}(\xi,\eta) + \hat{g}(\xi,\eta)u + \tilde{g}(\xi,\eta)u - K(A\eta + B\xi) \end{aligned} \tag{3.10}$$

Define the control u as

$$u = \hat{g}^{-1}(\xi,\eta)\cdot[-\hat{f}(\xi,\eta) + K(A\eta + B\xi) + v] \tag{3.11}$$

where v is the new control input vector. Then the sliding manifold dynamics satisfy

$$\dot{s} = \Delta(\xi,\eta,v) + v \tag{3.12}$$

where

$$\begin{aligned} \Delta(\xi,\eta,v) = {} & \tilde{f}(\xi,\eta) + \tilde{g}(\xi,\eta)\hat{g}^{-1}(\xi,\eta)\cdot[-\hat{f}(\xi,\eta) + K(A\eta + B\xi)] \\ & + \tilde{g}(\xi,\eta)\hat{g}^{-1}(\xi,\eta)v \end{aligned} \tag{3.13}$$

Without loss of generality, we assume that there exists a function $\gamma_1(\xi,\eta) > 0$ s.t.

$$\left\| \tilde{f}(\xi,\eta) + \tilde{g}(\xi,\eta)\hat{g}^{-1}(\xi,\eta)\cdot[-\hat{f}(\xi,\eta) + K(A\eta + B\xi)] \right\|_\infty \le \gamma_1(\xi,\eta) \tag{3.14}$$

and a constant $0 < \gamma_2 < 1$ s.t.

$$\left\| \tilde{g}(\xi,\eta)\hat{g}^{-1}(\xi,\eta) \right\|_{\infty} \le \gamma_2 \qquad 3.15$$

then the *ith* element of the uncertainty Δ satisfies,

$$|\Delta_i(\xi,\eta,v)| \le \gamma_1(\xi,\eta) + \gamma_2 \| v \|_{\infty}, \text{ i=1, 2} \qquad 3.16$$

Define the new control input $v = \begin{bmatrix} v_1 & v_2 \end{bmatrix}^T$ as follows,

$$v_i = -\beta(\xi,\eta)\,\mathrm{sgn}(s_i), \text{ i=1, 2} \qquad 3.17$$

$$\beta(\xi,\eta) \ge \frac{\gamma_1(\xi,\eta)}{1-\gamma_2} + \beta_0 \qquad 3.18$$

and β_0 is a positive constant. Then the Lyapunov function $V_i = \frac{1}{2}s_i^2$, where $s = \begin{bmatrix} s_1 & s_2 \end{bmatrix}^T$, satisfies

$$\begin{aligned} \dot{V}_i &= s_i \dot{s}_i = s_i(\Delta_i(\xi,\eta,v) + v_i) \\ &\le |s_i| \cdot (\gamma_1(\xi,\eta) + \gamma_2\beta(\xi,\eta) - \beta(\xi,\eta)) \\ &= |s_i| \cdot (\gamma_1(\xi,\eta) - (1-\gamma_2)\beta) \\ &\le |s_i| \cdot (\gamma_1(\xi,\eta) + (1-\gamma_2) \cdot (\frac{-\gamma_1(\xi,\eta)}{1-\gamma_2} - \beta_0)) \\ &\le -\beta_0 |s_i| \end{aligned} \qquad 3.19$$

Following the proof for a general sliding-mode controller in [21] and using Eq. 3.19, it can be shown that it takes finite time to reach the sliding manifold $s_i = 0$, and then by the arguments behind the definition of the sliding manifold, we have $\xi \to 0$ and $\eta \to 0$ asymptotically. For implementation, we replace $\text{sgn}(s_i)$ in Eq. 3.17 with the continuous function $\frac{2}{\pi}\tan^{-1}(k \cdot s_i)$ with sufficiently large k, in order to reduce the chattering due to the discontinuous sign function. The specific values of the design parameters used in the simulations are given in Section 3.5.

3.3 Tracking

For a given reference signal $r(t)$, assuming that $r(t), \dot{r}(t)$ and $\ddot{r}(t)$ are bounded and available online, we design a sliding-mode controller for the supercavitating vehicle to track $r(t)$. Let z_r and θ_r denote reference signals for states z and θ respectively. Note that once z_r and θ_r are determined, reference signals for w and q are also determined through the first two dynamic equations of Eq. 2.29. Define four new states,

$$\begin{cases} \tilde{z} = z - z_r \\ \tilde{\theta} = \theta - \theta_r \\ \tilde{w} = w - \dot{z}_r - V\theta_r \\ \tilde{q} = q - \dot{\theta}_r \end{cases} \qquad 3.20$$

The derivatives of the new state variables are given as follows,

$$\begin{cases} \dot{\tilde{z}} = \dot{z} - \dot{z}_r = w - V\theta - \dot{z}_r = (w - \dot{z}_r - V\theta_r) - V(\theta - \theta_r) = \tilde{w} - V\tilde{\theta} \\ \dot{\tilde{\theta}} = q - \dot{\theta}_r = \tilde{q} \\ \dot{\tilde{w}} = \dot{w} - \ddot{z}_r - V\dot{\theta}_r \\ \dot{\tilde{q}} = \dot{q} - \ddot{\theta}_r \end{cases} \qquad 3.21$$

Therefore, the sliding manifold is redesigned to stabilize the new state variables $\begin{bmatrix} \tilde{z} & \tilde{\theta} & \tilde{w} & \tilde{q} \end{bmatrix}^T$. Following the design of the sliding manifold in the stabilization problem, we define

$$\tilde{s} = \begin{bmatrix} \tilde{w} \\ \tilde{q} \end{bmatrix} - K \begin{bmatrix} \tilde{z} \\ \tilde{\theta} \end{bmatrix} \qquad 3.22$$

where K is defined as in Eq. 3.10 s.t. $(A + BK)$ is asymptotically stable. Then the dynamics for the new sliding manifold satisfy

$$\dot{\tilde{s}} = f(\xi,\eta) + g(\xi,\eta)u - K(A\eta + B\xi) + \begin{bmatrix} -\ddot{z}_r - V\dot{\theta}_r \\ -\ddot{\theta}_r \end{bmatrix} + K \begin{bmatrix} \dot{z}_r \\ \dot{\theta}_r \end{bmatrix} \qquad 3.23$$

Following a similar design procedure as Eq. 3.11 and Eq. 3.17, we derive a stabilizing controller for the sliding manifold $\tilde{s}$,

$$\begin{bmatrix}\delta_f\\ \delta_c\end{bmatrix} = -\hat{g}^{-1}(\xi,\eta)\cdot(\hat{f}(\xi,\eta) - K(A\eta + B\xi) + \begin{bmatrix}-\ddot{z}_r - V\dot{\theta}_r\\ -\ddot{\theta}_r\end{bmatrix} + K\begin{bmatrix}\dot{z}_r\\ \dot{\theta}_r\end{bmatrix} + \beta\begin{bmatrix}\mathrm{sgn}(s_1)\\ \mathrm{sgn}(s_2)\end{bmatrix}) \quad 3.24$$

where the design parameter β can be designed in a similar way as that in the stabilization problem.

3.4 High-Gain Observer Design

As stated in [1] and [4], the vertical velocity w of a supercavitating vehicle might be difficult to measure, and thus it is often not available for feedback directly. Since the planing force depends on the vertical velocity as shown in Eq. 2.17, it is important to design an observer to estimate the vertical velocity *w*. In this section, a high-gain observer is designed to estimate the vertical velocity w based on the measurement of the vehicle depth z, assuming that the measurements of other state variables such as the pitch angle θ and pitch rate q are accurate and available for feedback. Other interesting observer design and state estimation results can be found in [19] and [20].

High-gain observers work for a wide class of nonlinear systems and guarantee that the output feedback controller recovers the performance of the state feedback controller when the observer gain is sufficiently high [21]. A high gain observer is selected in the dissertation since it is robust to uncertainties in a nonlinear system.

Assuming that state variables θ and q are directly available without any measurement error, we define the following notations in terms of Eq. 2.3,

$$A_1 = J^{-1} \cdot qV \begin{bmatrix} m_v \\ -m_v x_g \end{bmatrix} \tag{3.25}$$

$$A_2 = J^{-1} \cdot \begin{bmatrix} F_{bz}(z, \theta, w, q, u(\hat{z}, \theta, \hat{w}, q)) \\ M(z, \theta, w, q, u(\hat{z}, \theta, \hat{w}, q)) \end{bmatrix} \tag{3.26}$$

$$\hat{A}_2 = J^{-1} \cdot \begin{bmatrix} \hat{F}_{bz}(\hat{z}, \theta, \hat{w}, q, u(\hat{z}, \theta, \hat{w}, q)) \\ \hat{M}(\hat{z}, \theta, \hat{w}, q, u(\hat{z}, \theta, \hat{w}, q)) \end{bmatrix} \tag{3.27}$$

where

$$J = \begin{bmatrix} m_v & -m_v x_g \\ -m_v x_g & I_{yy} \end{bmatrix} \tag{3.28}$$

Note that the state-feedback control u in A_2 is defined in terms of the direct measurements of θ and q, as well as the state estimates $\hat{z}$ and $\hat{w}$. In $\hat{A}_2$, which denotes the estimated A_2, $\hat{F}_{bz}(\hat{z}, \hat{w}, \cdot)$ and $\hat{M}(\hat{z}, \hat{w}, \cdot)$ are defined by replacing (z, w) with the state estimates $(\hat{z}, \hat{w})$ in F_{bz} and M. Let $A_1[1]$, $A_2[1]$ and $\hat{A}_2[1]$ denote the first row of A_1, A_2 and $\hat{A}_2$ respectively. Since we assume that state variables θ and q are directly available,

consider the subsystem consisting of the state variable $[z \quad w]^T$ and output variable $y = z$. A simple observability analysis for this linearized subsystem shows that the observability matrix $O = [1 \quad 0; * \quad *]$ has full rank, where * represents nonzero element. That is, the linearized subsystem is observable, and thus we specify the observer for (z, w) as follows,

$$\dot{\hat{z}} = \hat{w}\cos\theta - V\sin\theta + h_1(y - \hat{z}) \tag{3.29}$$

$$\dot{\hat{w}} = A_1[1] + \hat{A}_2[1] + h_2(y - \hat{z}) \tag{3.30}$$

$$y = z \tag{3.31}$$

where $y = z$ denotes the measurement of the depth z, and h_1, h_2 denote the observer gains to be designed. Define the error variables as

$$e = \begin{bmatrix} e_z \\ e_w \end{bmatrix} = \begin{bmatrix} z - \hat{z} \\ w - \hat{w} \end{bmatrix} \tag{3.32}$$

then we have the error dynamics as,

$$\begin{bmatrix} \dot{e}_z \\ \dot{e}_w \end{bmatrix} = \begin{bmatrix} -h_1 & \cos\theta \\ -h_2 & 0 \end{bmatrix} \begin{bmatrix} e_z \\ e_w \end{bmatrix} + \begin{bmatrix} 0 \\ o(z, w, \hat{z}, \hat{w}) \end{bmatrix} \tag{3.33}$$

with $o(z, w, \hat{z}, \hat{w}) = A_2[1] - \hat{A}_2[1]$. By specifying the observer gain as,

$$h_1 = \frac{2}{\varepsilon_1},\ h_2 = \frac{1}{\varepsilon_2^2} \tag{3.34}$$

where $\varepsilon_1 > 0$ and $\varepsilon_2 > 0$, the high-gain observer dynamic matrix becomes $\begin{bmatrix} -2/\varepsilon_1 & \cos\theta \\ -1/\varepsilon_2^2 & 0 \end{bmatrix}$, and the eigenvalues are placed to $-\frac{1}{\varepsilon_1} \pm \sqrt{\frac{1}{\varepsilon_1^2} - \frac{1}{\varepsilon_2^2}\cos\theta}$, which stay in the left-half complex plane for all $\cos\theta > 0$. A commonly-seen and convenient choice of the design parameters for a high-gain observer is to set $\varepsilon_1 = \varepsilon_2 = \varepsilon$, where $0 < \varepsilon << 1$, and then the eigenvalues become $-\frac{1}{\varepsilon}(1 \pm \sqrt{1 - \cos\theta})$; for the special case $\cos\theta = 1$, the eigenvalues are placed at $-1/\varepsilon$. In addition, the transfer function from $o(z, w, \hat{z}, \hat{w})$ to e, which is

$$T(s) = \frac{\varepsilon}{(\varepsilon s)^2 + 2\varepsilon s + 1} \begin{bmatrix} \varepsilon \\ \varepsilon s + 2 \end{bmatrix} \tag{3.35}$$

goes to zero when $\varepsilon \to 0$. Consequently, Eq. 3.29 and Eq. 3.30 define a high gain observer for estimating (z, w) in terms of the measurements of z, θ and q.

Remark 3.4.1: It is a well-known concern regarding the performance of a high-gain observer in the presence of measurement noise. In [22], related analysis work has been conducted on the effect of choosing different ε on minimizing the state estimation error bound. It was shown in [22] that although letting $\varepsilon \to 0$ will reduce the state estimation error in the absence of noise, $\varepsilon \to 0$ will also amplify the noise. Therefore an appropriate ε is needed to achieve the balance between minimizing the state estimation error due to $o(z, w, \hat{z}, \hat{w})$ and minimizing the error bound due to the measurement noise.

3.5 Simulation Results

In this section, we present simulation results for the sliding-mode controller (SMC). First, we will show the results when the high-gain observer is not included in simulations. Then we will present the simulation results for the nonlinear partial output-feedback controller, which combine the sliding-mode controller (SMC) with the high-gain observer.

In order to offer results that are comparable with those presented in [1] and [4], we first show the initial responses, where the initial condition is given by $z = 0$, $\theta = 0$, $w = 3m/sec$, and $q = 0.2rad/sec$. Additional tracking responses are also simulated to further evaluate the controllers' performance. The numerical example used in the following simulations is based on parameter values in Appendix D that are the same as those used in [1].

A similar first-order actuator model as in [18], with transfer function $\frac{300}{s+300}$, is

used for both the cavitator and fin control in the simulations presented in this section. In addition, we assume that the actuators are subject to amplitude limits of $|\delta_c| \le 25\ deg$ and $|\delta_f| \le 25\ deg$, and a rate limit of 100 rad/sec [18], noting that δ_f over a high angle may compromise control effectiveness.

Note that small-angle approximation is used to derive the equations of motion. Eq. 2.29 is valid only when the deflection angles of the cavitator and fins are not too large. It is well known that actuator saturation could have a detrimental effect on control performance, and it may even cause instability, especially for multiple-input multiple-output systems [23]. In the literature, there are many compensation designs to handle control input saturation [23 - 27]. From Eq. 2.29, we can see that δ_f and δ_c play very similar roles in controlling w and q. Thus, if one actuator, either δ_f or δ_c, becomes saturated due to physical limitation, while the other one still has plenty of room before becoming saturated, it is possible to reallocate the control between δ_f and δ_c such that the same control performance can be achieved without exceeding the physical limitation of either δ_f or δ_c. In Appendix C, we describe in details a control-reallocation-based saturation compensation, which is applied in simulations in this dissertation when needed. We have observed that without this saturation compensation, closed-loop systems may become unstable if control inputs are forced to stay within their physical limitations. On the other hand, we can imagine that if the required control actuation is so large that both δ_f and δ_c will get saturated even after control reallocation, then additional saturation

compensation techniques, e.g., anti-windup based saturation compensation, maybe needed. However, this is not the case for the simulations in this dissertation.

In the rest of this section, we let saturation compensation (SC) denote the simulations with the above-referenced actuator model and actuation limits (but augmented by the saturation compensation once the amplitude limit is touched). We also let unlimited control (UC) represent the simulations with actuators of no limitation on either amplitude or rate.

For the sliding-mode controller (SMC), as shown in Tab. 3-1, the feedback gain matrix K is designed using an LQ regulator with $Q = I_{2\times 2}$, $R = 5I_{2\times 2}$; the design parameter k in approximating the discontinuous sign function is set to be 100; $\beta(\xi,\eta)$ in Eq. 3.18 is set to be a constant 50. According to Eq. 3.18, as $\beta(\xi,\eta)$ becomes larger, the closed loop system becomes capable of achieving better robustness, although the controller becomes more conservative. We consider uncertainties in system parameters that include variations in the parameters $\frac{C_x}{m}$ and n. Later in this chapter, we also evaluate the performance of the sliding-mode controller (SMC) using the Time-Delay Benchmark Model even though the controller is not designed to deal with the memory effect of the cavity-vehicle interaction.

Table 3-1: Design parameters for the sliding-mode controller (SMC)

Parameter	Value
K	$\begin{bmatrix} 0.0487 & -0.4446 \\ -0.4446 & 8.1661 \end{bmatrix}$
$\beta(\xi,\eta)$	50
k	100

3.5.1 Simulation Results without the High-gain Observer

A. Nominal performance

Fig. 3-1 plots the initial-response time histories of the state, control, and planing force for the nominal closed-loop system, to which the sliding-mode controller (SMC) with unlimited control (UC) and the saturation compensation (SC) is applied respectively. This initial response is conducted using the Benchmark Model without including the memory effect of cavity-vehicle interaction. States have more obvious oscillation in the SC case than in the UC case, since both the amplitude and rate limits of δ_f are touched in the former, and thus the amplitude of δ_c is adjusted by the saturation compensation to coordinate the two controls and so maintain system stability. We have learned from our simulations that if actuation amplitude limits are imposed but no saturation compensation is implemented, the closed-loop system will become unstable.

Fig. 3-2 plots the initial-response time histories of state, control, and planing force for the nominal closed-loop system, where the sliding-mode controller (SMC) with saturation compensation (SC) is applied. In this figure, we show both simulations with

and without the memory effect of the cavity-vehicle interaction. The planing force model without memory effect is described in Eq. 2.17, Eq. 2.24 and Eq. 2.25; the model with the memory effect is given in Eq. 2.17, Eq. 2.34 and Eq. 2.35, where the delay time $\tau = L/V$ caused by the memory effect is calculated as $\tau = 0.024$ in terms of the vehicle configuration parameters in Appendix D. Fig. 3-2 shows that the sliding-mode controller (SMC) can stabilize the nominal system even in the presence of the memory effect. It is worth pointing out that in Fig. 3-2, the rate limit for δ_f is touched in the simulation, but by imposing a hard constraint of $100\, rad/sec$ on the rate limit, the system is still stabilized without degrading performance very much. Also, if actuation amplitude limits are imposed without saturation compensation, the closed-loop system will become unstable.

The tracking performance of the sliding-mode controller (SMC) for the nominal system is shown in Fig. 3-3 and Fig. 3-4. Here, we consider two tracking reference signals: a unit-step input for the depth *z* is used as the reference signal in Fig. 3-3, and the *w*-tracking response is shown in Fig. 3-4, where the reference signal is

$$w_r = 2\sin(2\pi t),\ z_r = 0,\ \theta_r = \frac{w}{V}, \text{ and } q_r = \dot{\theta}_r \qquad 3.36$$

According to the Time-Delay Benchmark Model, the small magnitude of the vertical velocity *w* in the simulation shown in Fig. 3-3 would not induce any planing force. For the *w*-tracking response in Fig. 3-4, though, planing force does occur;

therefore, the memory effect in the planing force model is included in the simulation. Fig. 3-3 shows that the z-step response has a settling time of less than one second. Fig. 3-4 also shows very good tracking performance, though the rate limit of the fin surface deflection δ_f has been reached.

B. Robustness Evaluation

A close observation of the system equations (i.e. Eq. 2.32) shows that if the forward speed V and the vehicle length L are assumed to be a known constant, the possible uncertainties in the system matrices A_I and B_I could be considered to come from $\frac{Cn}{m}$ and $\frac{C}{m}$. By Eq. 2.30, we see that if the vehicle and cavitator configuration parameters R and R_n are fixed, the ratio of the cavitator's radius and the cylindrical section radius of the vehicle remain constant. Then, the possible parametric uncertainty in A_I and B_I is basically associated with $\frac{C_x n}{m}$ and $\frac{C_x}{m}$. Hence, we consider $\frac{C_x}{m}$ and n to be the uncertain parameters used in robust control that essentially cover variations in control-effective coefficients and variation in the density ratio of the vehicle and fluid/water.

To illustrate the robustness of the sliding-mode controller (SMC), Figs. 3-5 and 3-6 plot the stochastic envelopes of the state, control, and planing force histories based on 100 Monte Carlo simulations of the tracking responses (*z*-step response and *w*-tracking response). The memory effect is included in the planing force model used in the simulations. The uncertainties used in the Monte Carlo simulations include $\pm 5\%$

variations in the parameters $\frac{C_x}{m}$ and n. The random samples are generated using normal distributions, which have zero mean and 0.05 std, and are then truncated within $\pm 5\%$ variation of the nominal values. The stochastic envelopes consist of maximum, mean, and minimum values at each time instance. Figs. 3-5 and 3-6 show that the sliding-mode controller (SMC) is robust to system parameter uncertainties and the planing force memory effect, although the latter is not included in the control design.

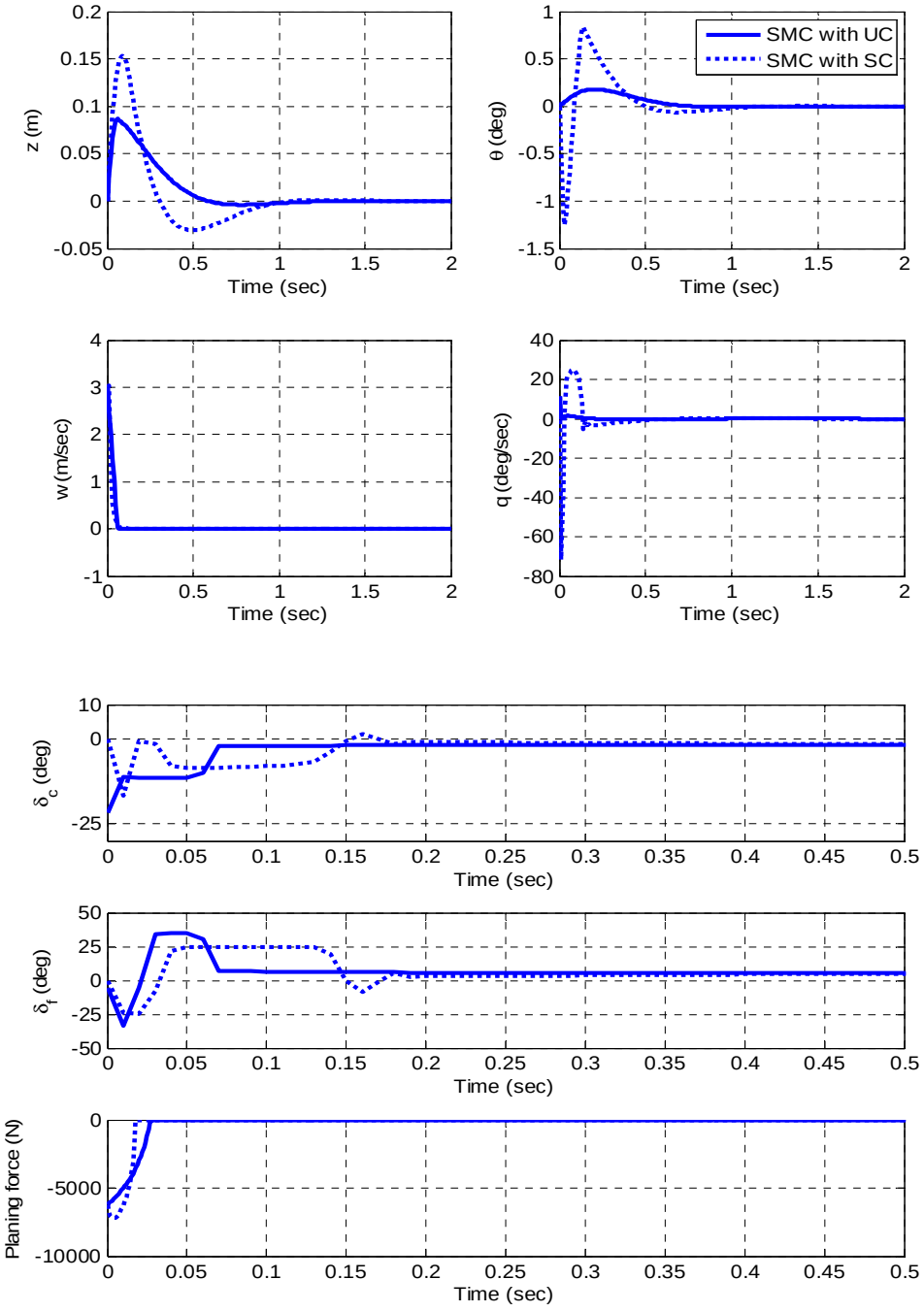

Figure 3-1: Initial responses for nominal systems implemented with the sliding-mode controller (SMC) with UC and SC, without consideration of cavity memory effect.

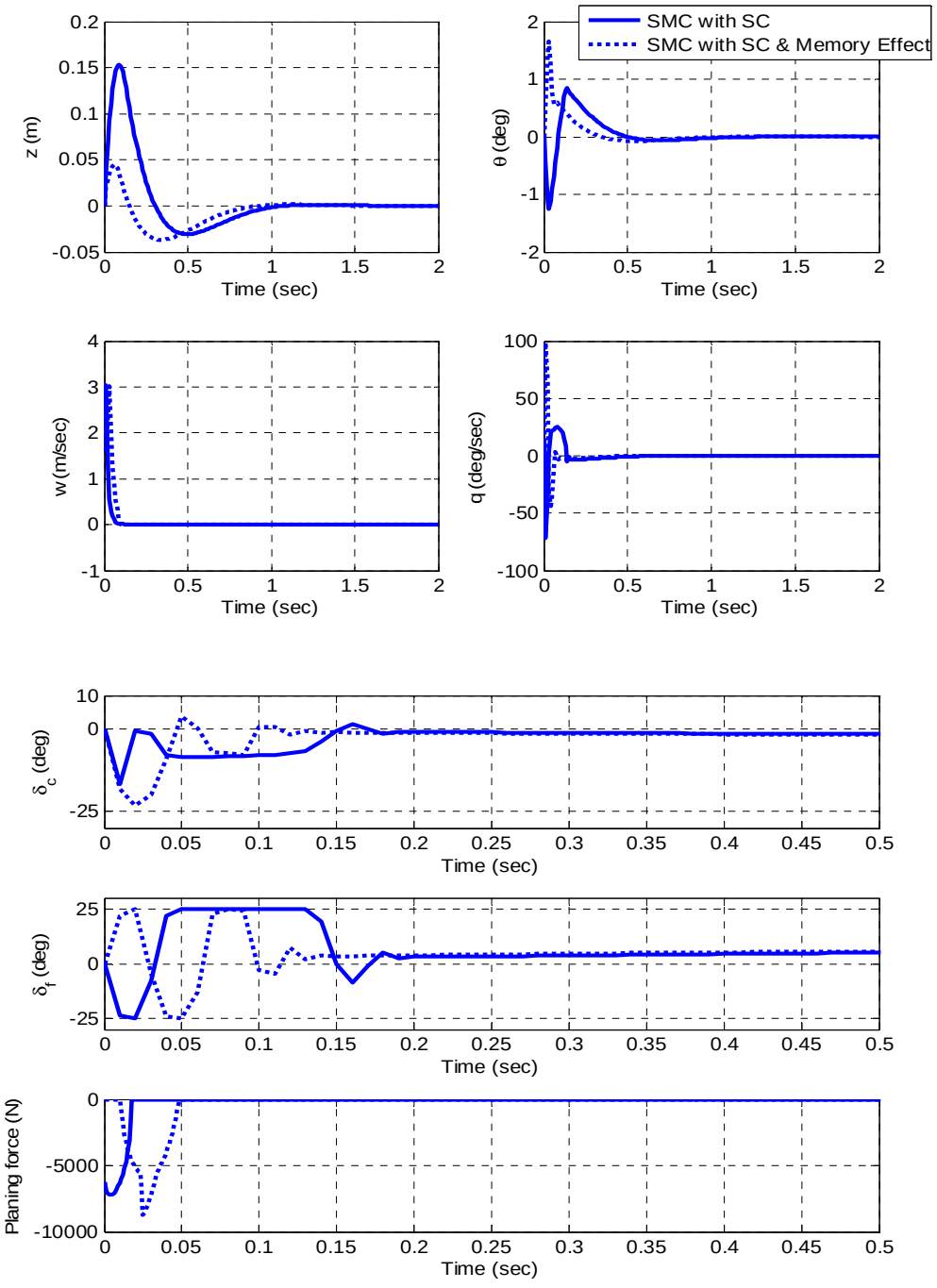

Figure 3-2: Initial responses for nominal systems implemented with the sliding-mode controller (SMC) with SC, with and without consideration of cavity memory effect.

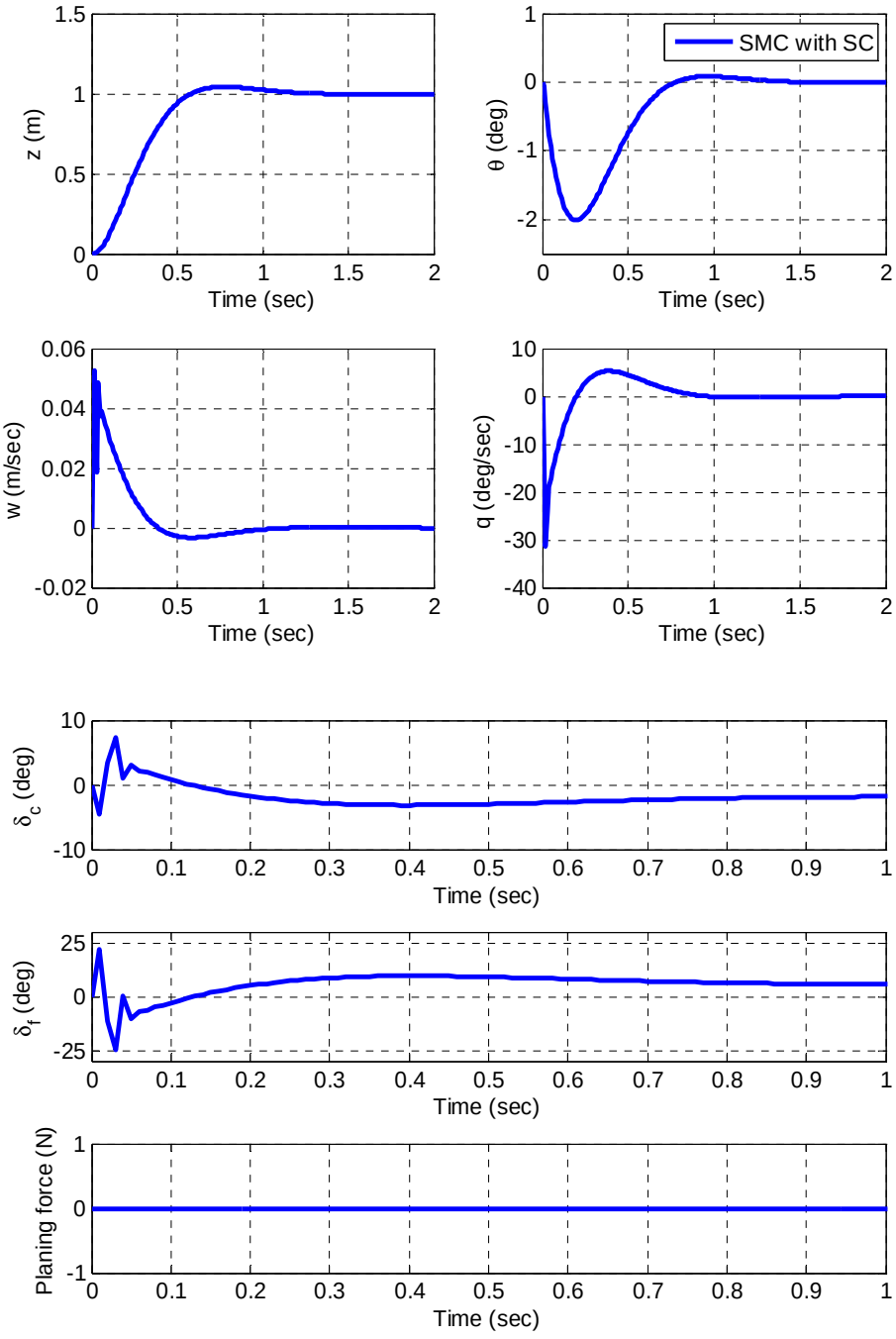

Figure 3-3: z-step response for the nominal system, implemented with the sliding-mode controller (SMC) with SC, with consideration of cavity memory effect. The planing force remains zero.

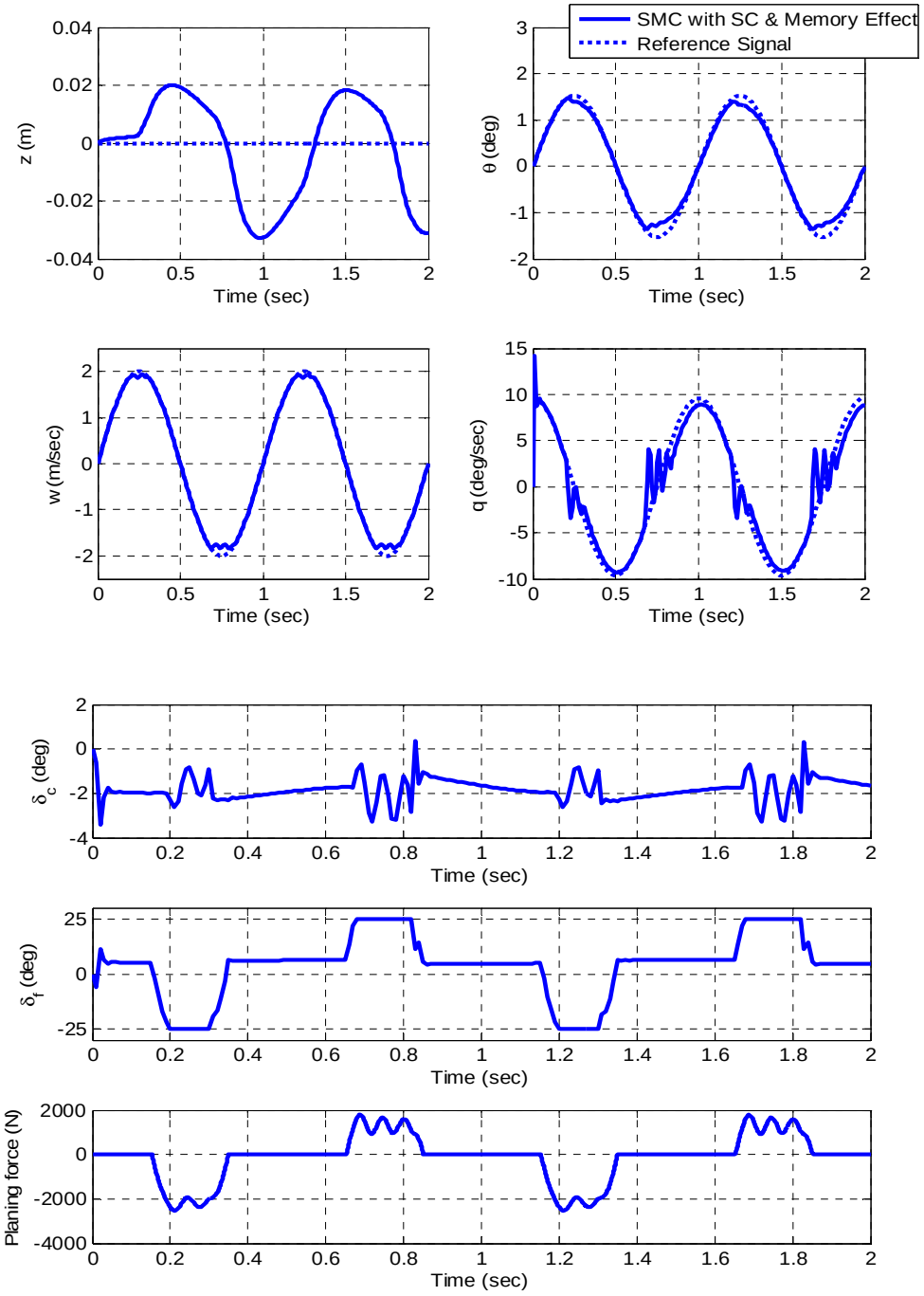

Figure 3-4: w-tracking response for the nominal system, implemented with the sliding-mode controller (SMC) with SC, with consideration of cavity memory effect.

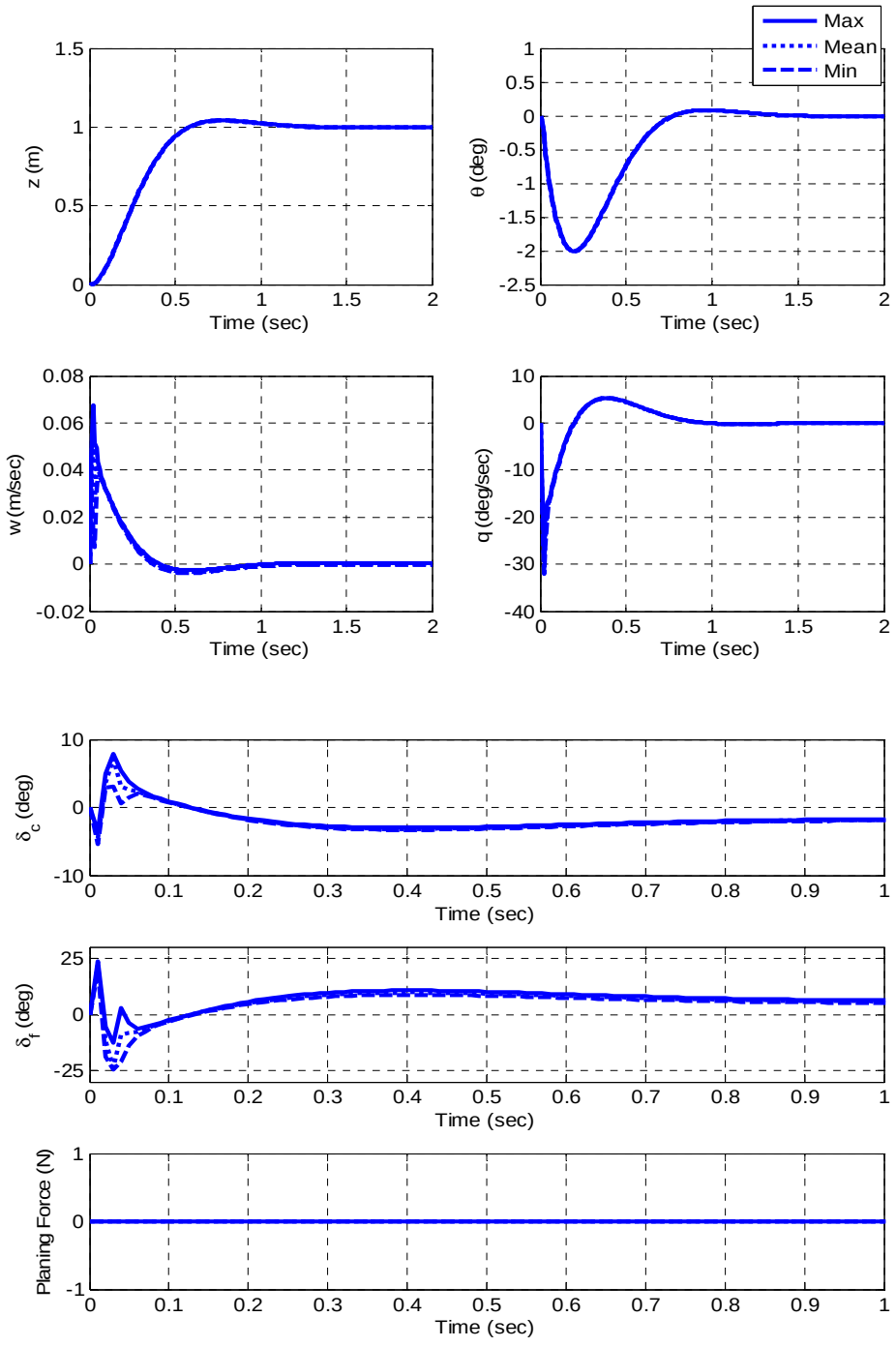

Figure 3-5: Stochastic envelopes of the z-step tracking responses for the uncertain system, implemented with the sliding-mode controller (SMC) with SC.

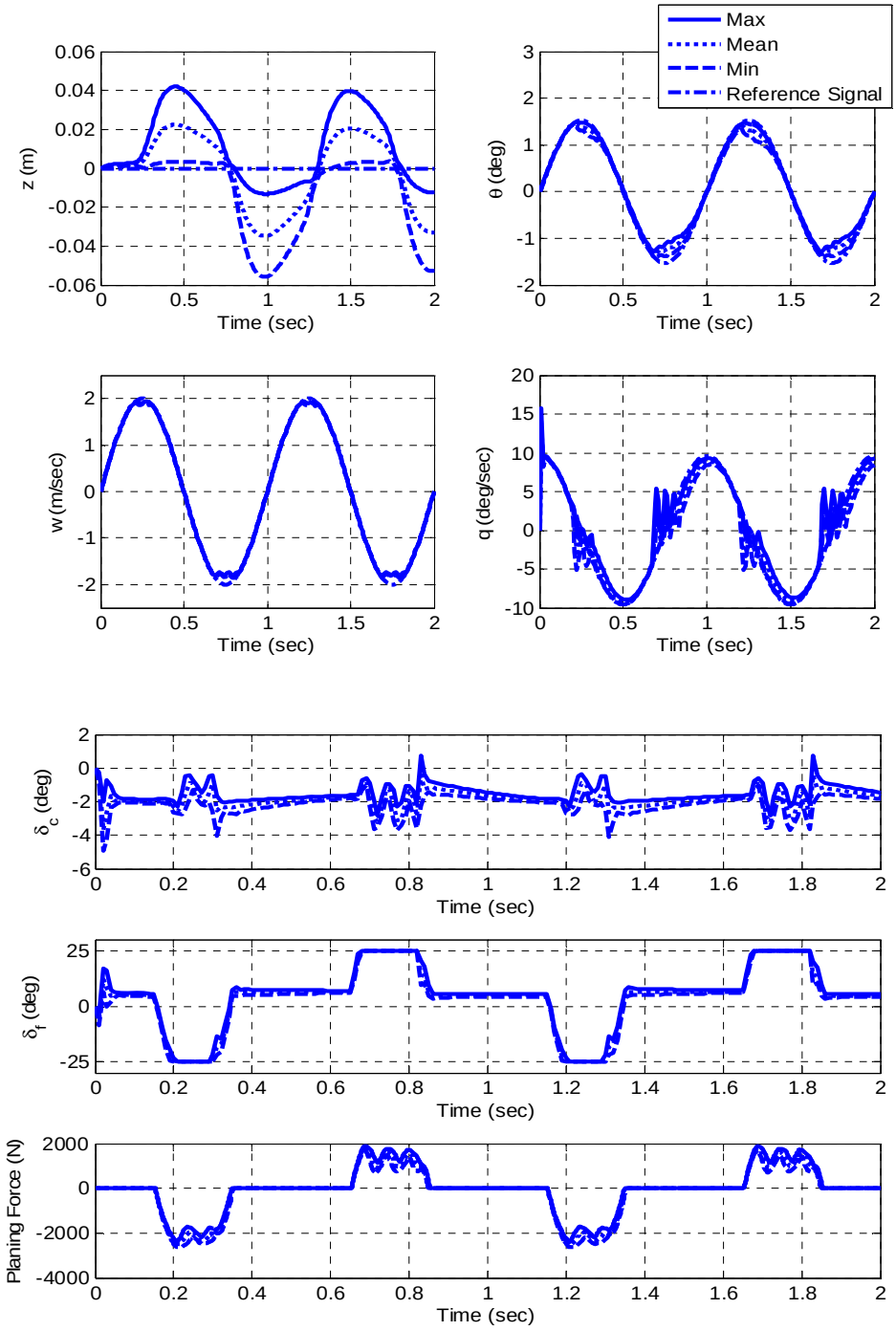

Figure 3-6: Stochastic envelopes of the w-tracking responses for the uncertain system, implemented with the sliding-mode controller (SMC) with SC.

3.5.2 Simulation Results with the High-gain Observer

In this section, we repeat all the simulations shown in the last section for the output feedback controllers. The only difference is that here we include the designed high-gain observer in our consideration when an observer is necessary. The high-gain observer parameter is set as ε = 0.00015. For all initial responses, the initial conditions of the high-gain observer are specified as $\hat{z} = 0, \hat{w} = 0$; i.e., the estimated initial $\hat{w}$ is away from its true value.

The results of the simulations shown in Figs. 3-7 - 3-12 correspond with those shown in Figs. 3-1 - 3-6 respectively. It is clear that the closed-loop systems with the high-gain observer can achieve almost the same performance as the closed-loop systems without the observer, in both the nominal performance and the robustness testing simulations.

To further explore the performance of the observer, Fig. 3-13 shows the time histories of the estimation errors e_z and e_w (as defined in Eq. 3.32) when the observer is implemented with the sliding-mode controller (SMC) in initial responses for which the high-gain observer parameter is set as ε = 0.00015. Recall that the initial conditions for the high-gain observer are specified as $\hat{z} = 0, \hat{w} = 0$; i.e., the estimated initial $\hat{w}$ is away from its true value $w = 3m/sec$. We can see that the state estimation errors converge to zero quickly despite the uncertain nonlinear aspect $o(z, w, \hat{z}, \hat{w})$ of Eq. 3.33. This is because the transfer function from $o(z, w, \hat{z}, \hat{w})$ to the estimation errors is almost zero due to the high gain of the observer.

Here, we also use simulations to show how the high-gain observer behaves under sensor measurement noise. In the presence of the sensor measurement noise of *z*, Fig. 3-14 plots the initial responses corresponding to the sliding-mode controller (SMC) combined with a high-gain observer. The sensor measurement noise used in the simulations in Fig. 3-14 is white noise with a power of 10^{-8} and a sample time of 0.001 sec. Following the discussions in [28], we reset the high-gain observer design parameter $\varepsilon = 0.00001$ for the sliding-mode controller. Note that the ε value is fine-tuned for the sliding-mode controller (SMC) in order to balance the minimization of the state estimation errors against the amplification of the sensor noise. It is observed that the controller is still able to stabilize the system, even though the sensor noise causes oscillations in the control inputs δ_c and δ_f. It is also noted that the rate limit for δ_c is reached, as shown in Fig. 3-14.

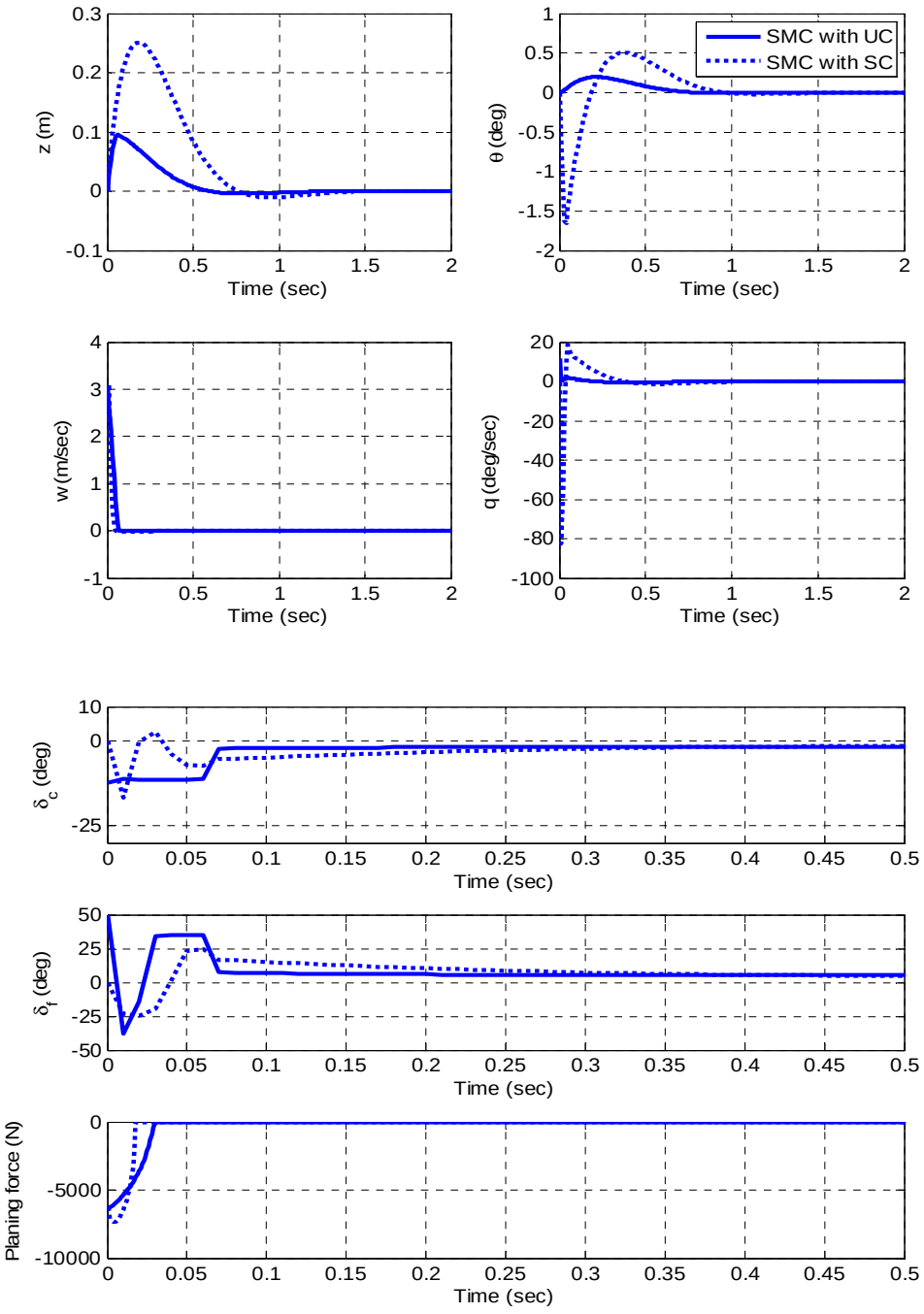

Figure 3-7: Initial responses for nominal systems implemented with the sliding-mode controller (SMC) with UC and SC, without consideration of cavity memory effect. The high-gain observer is also included in the simulations.

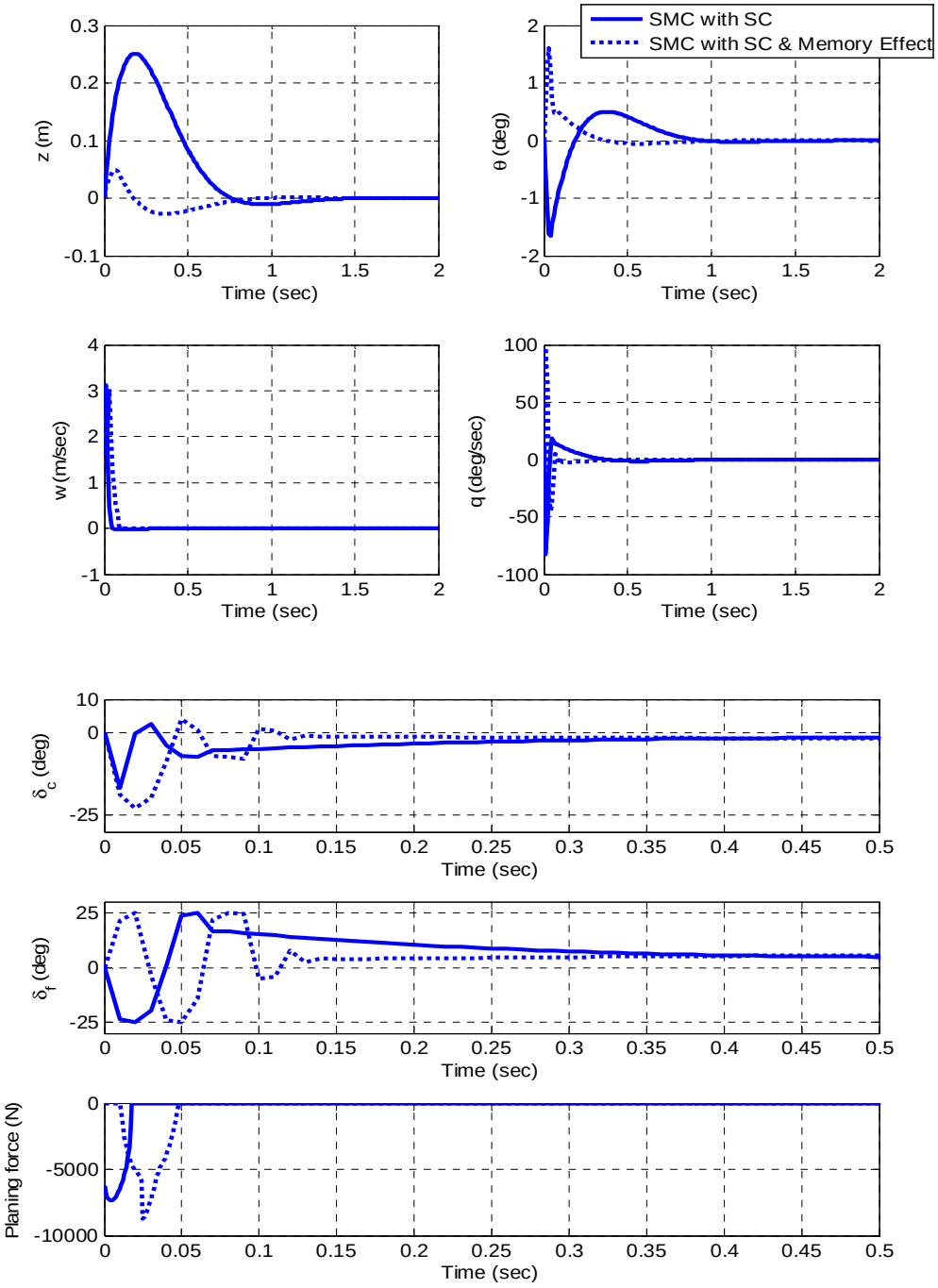

Figure 3-8: Initial responses for nominal systems implemented with the sliding-mode controller (SMC) with SC, with and without consideration of cavity memory effect. The high-gain observer is also included in the simulations.

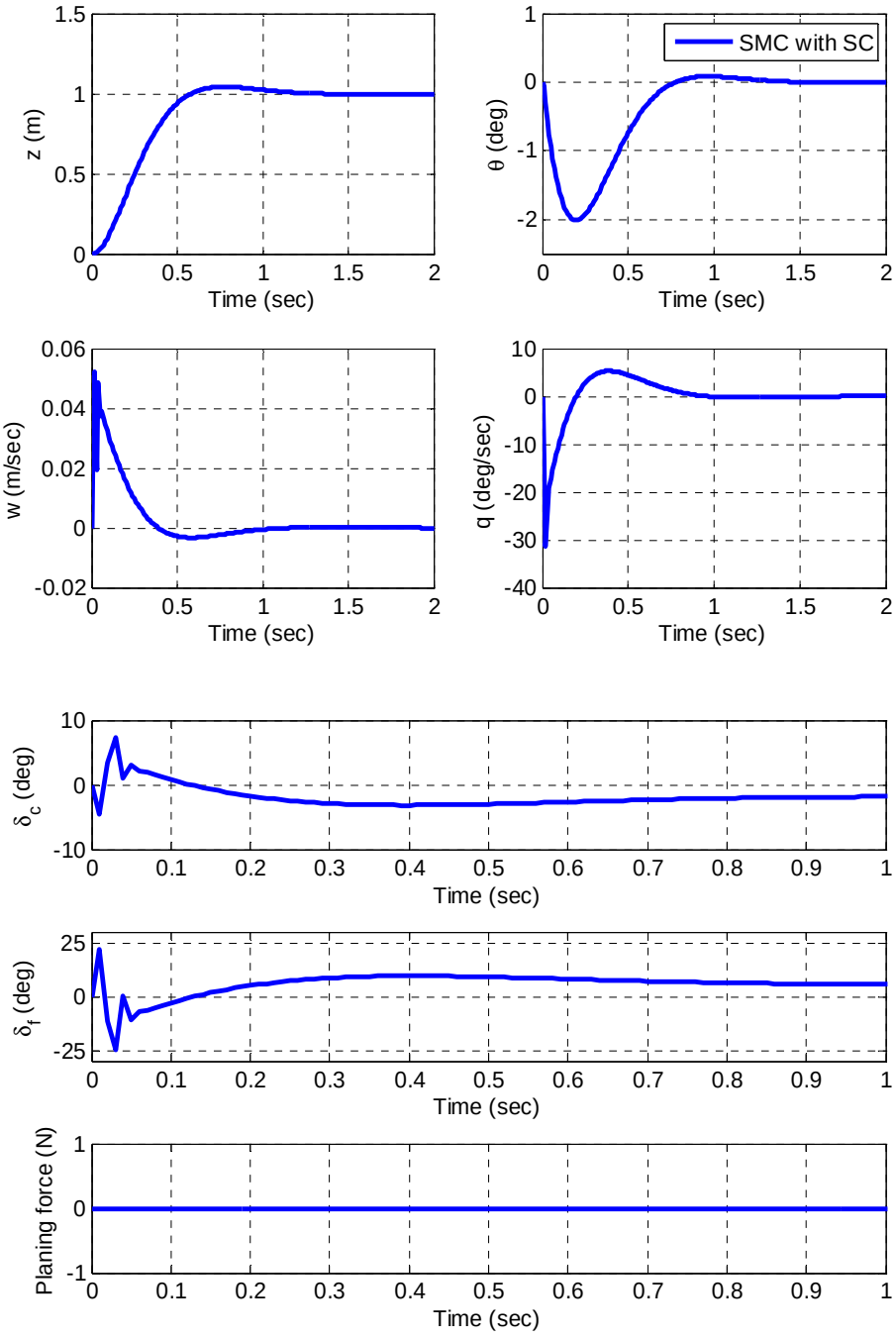

Figure 3-9: z-step response for the nominal system, implemented with the sliding-mode controller (SMC) with SC, with consideration of cavity memory effect. The high-gain observer is also included in the simulations. The planing force remains zero.

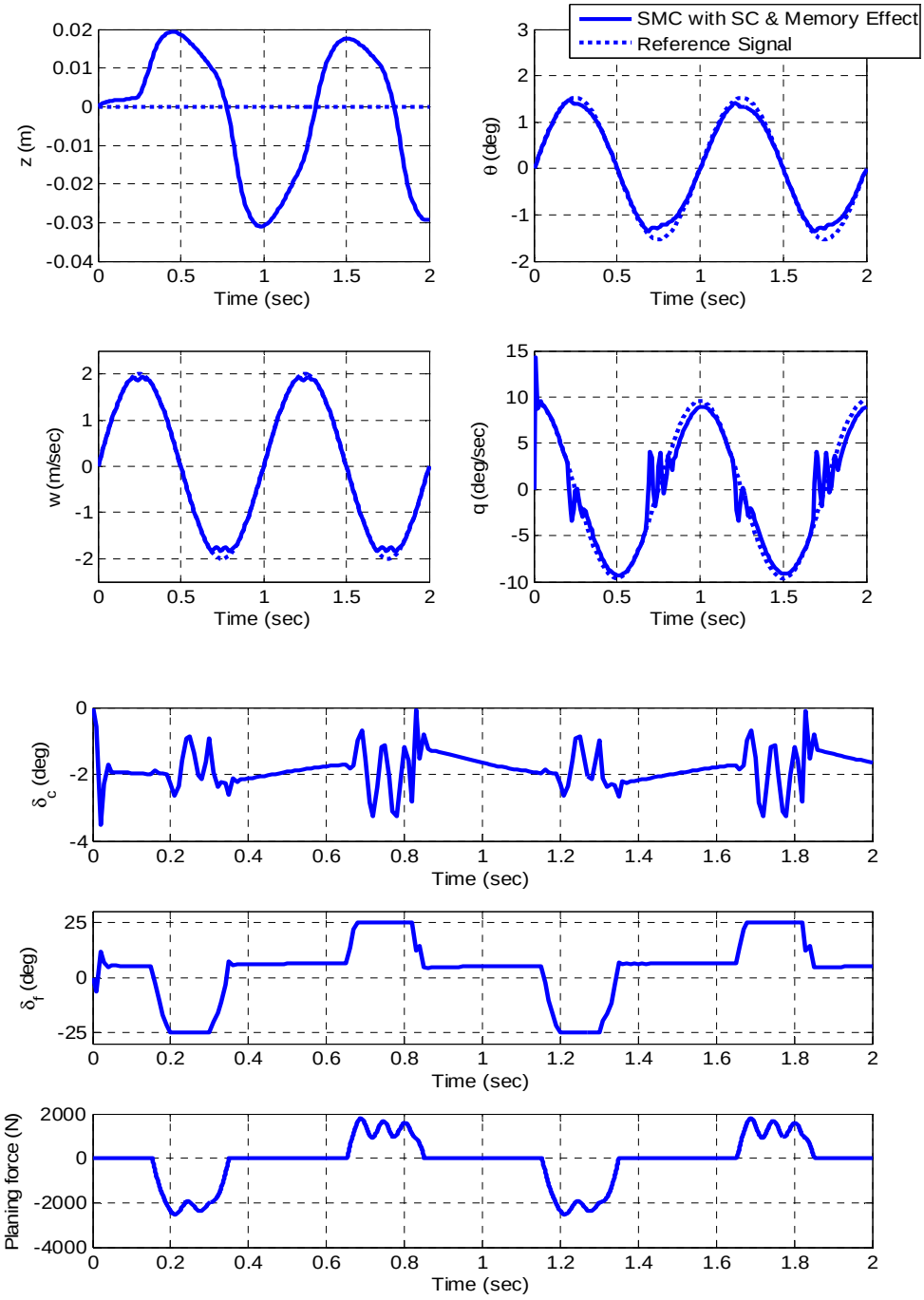

Figure 3-10: *w* -tracking response for the nominal system, implemented with the sliding-mode controller (SMC) with SC, with consideration of cavity memory effect. The high-gain observer is also included in the simulations.

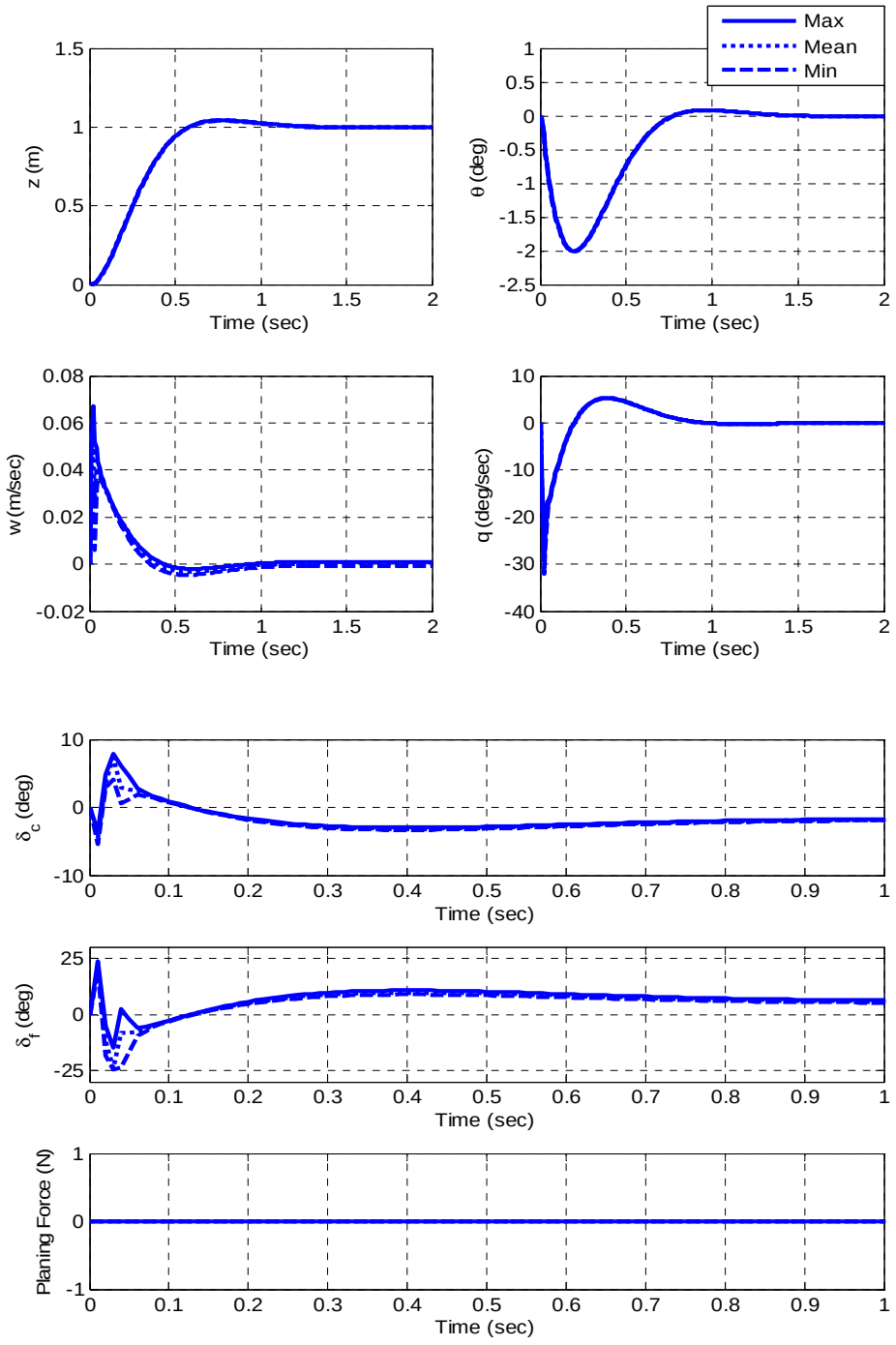

Figure 3-11: Stochastic envelopes of the z-step tracking responses for the uncertain system, implemented with the sliding-mode controller (SMC) with SC. The high-gain observer is also included in the simulations.

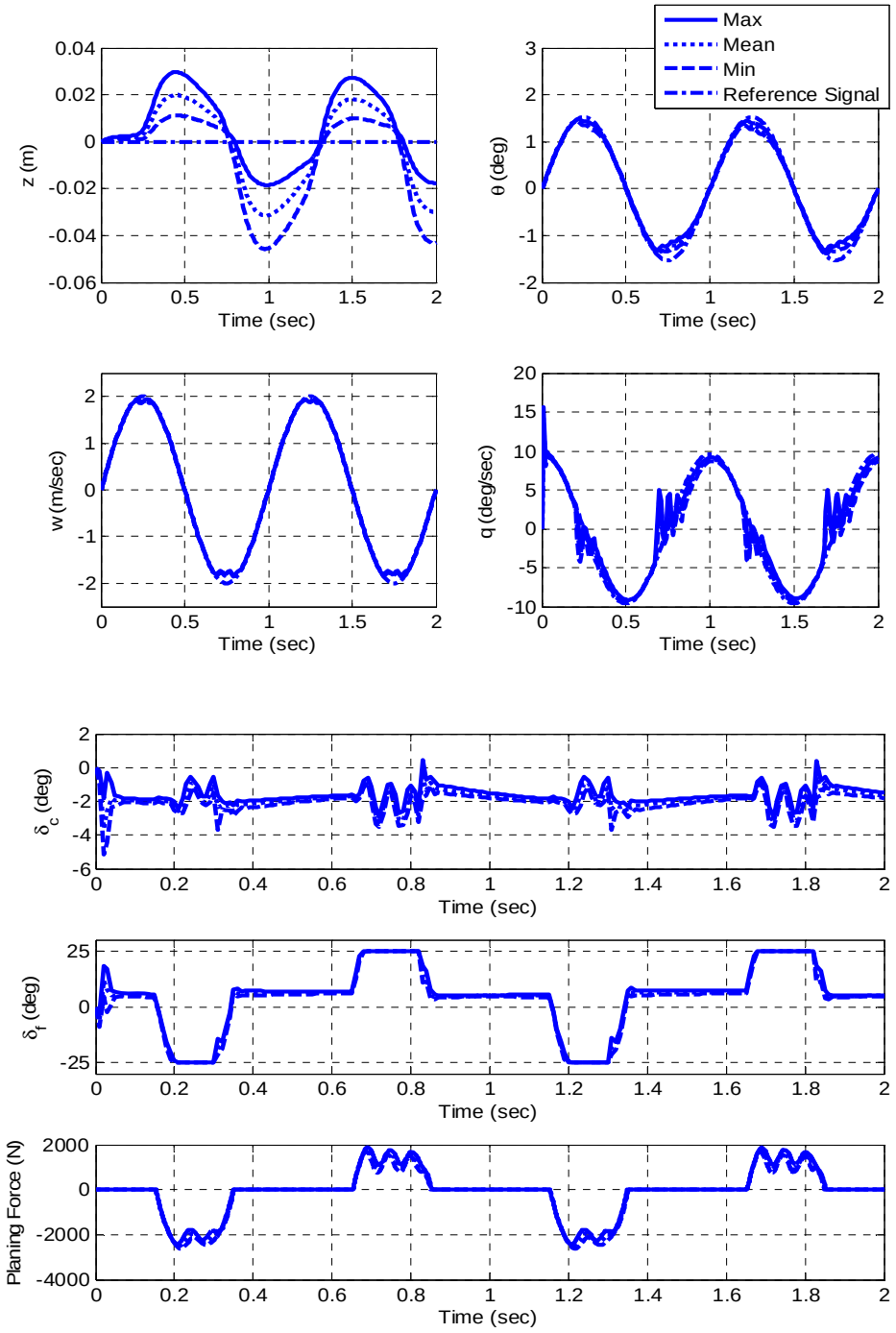

Figure 3-12: Stochastic envelopes of the w-tracking responses for the uncertain system, implemented with the sliding-mode controller (SMC) with SC. The high-gain observer is also included in the simulations.

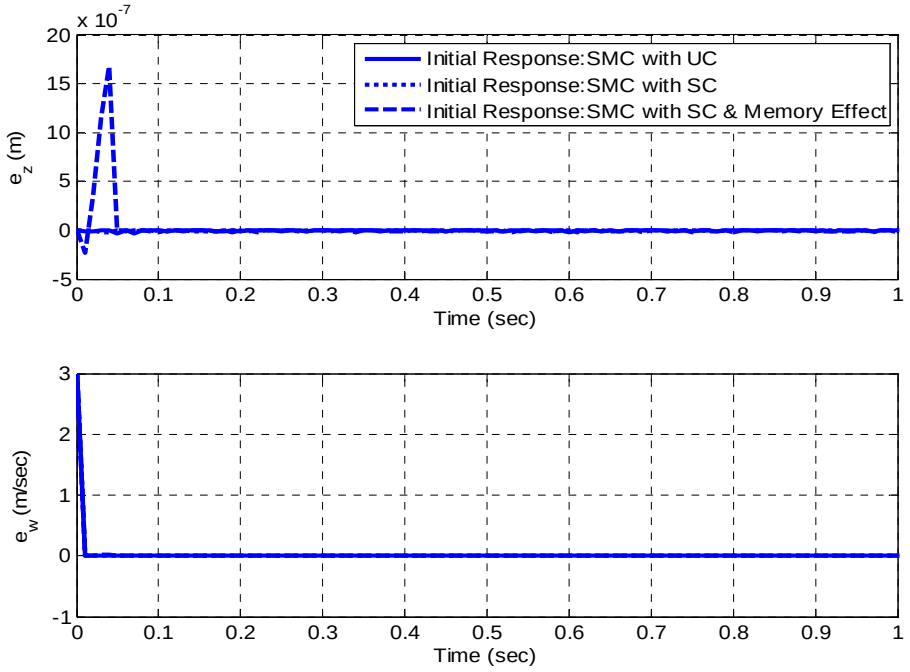

Figure 3-13: Performance of the high-gain observer in closed-loop systems implemented with the sliding-mode controller (SMC). No measurement noise is considered.

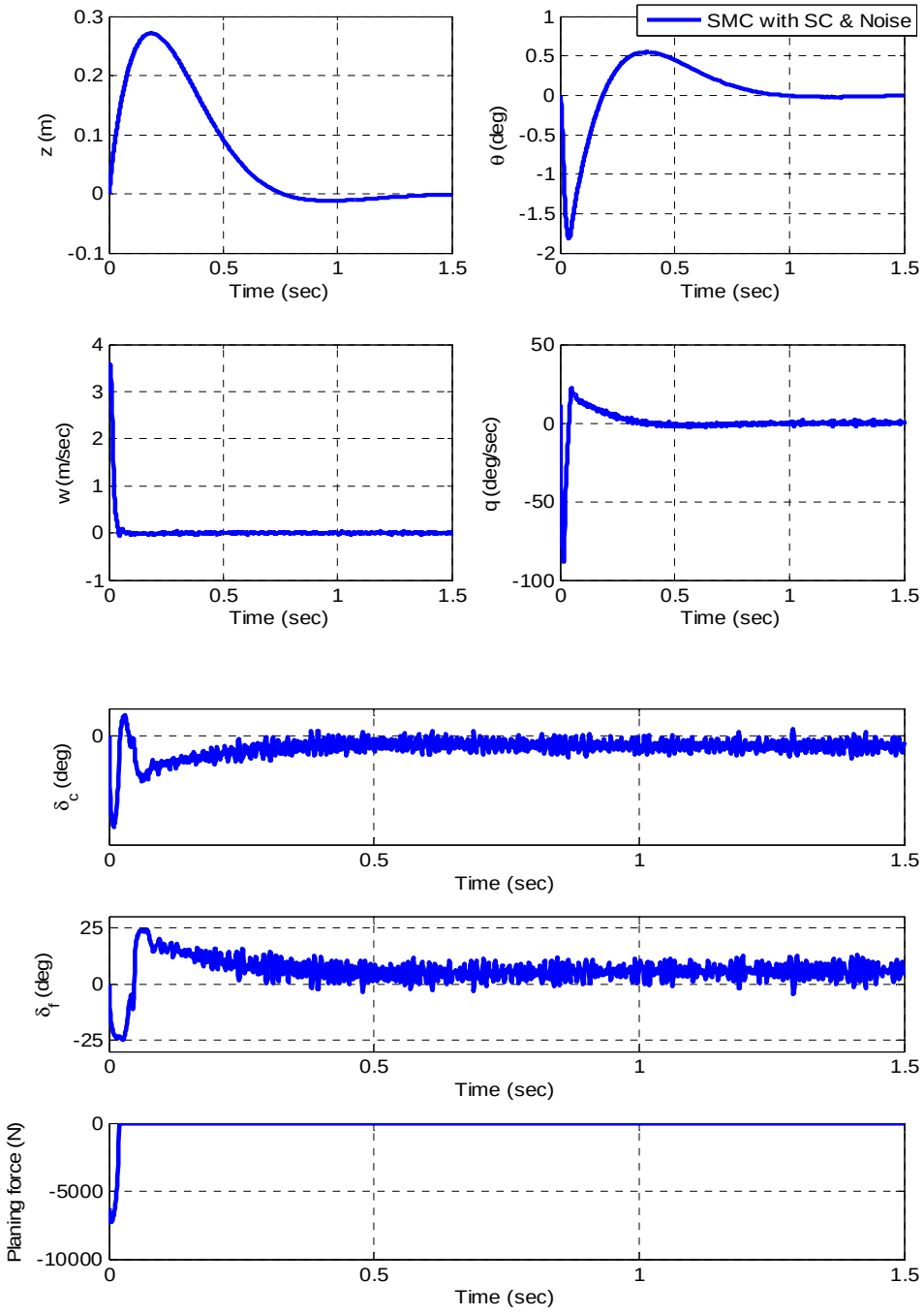

Figure 3-14: Sensitivity of initial response to measurement noise in z, under the sliding-mode controller (SMC) with SC and the high-gain observer.

Chapter 4

Quasi-LPV Control for the Benchmark Model of Supercavitating Vehicles

4.1 Introduction

The Linear-Parameter-Varying (LPV) method can be applied to a nonlinear system by reformulating that system into a Quasi-Linear-Parameter-Varying (Quasi-LPV) representation, $\dot{x} = A(\kappa(x))x + B(\kappa(x))u$, in which κ is a parameter depending on the state. Hence, the nonlinear dynamics become the linear parameterization of dynamics through the scheduling parameter κ, such that a Quasi-LPV controller can be designed. Note that a Quasi-LPV form can be formulated in many possible ways. For example, for any $l(\kappa(x))$ satisfying $l(\kappa(x))x = 0$, the Quasi-LPV system $\dot{x} = A(\kappa(x))x + B(\kappa(x))u$ is equivalent to $\dot{x} = (A(\kappa(x)) + l(\kappa(x)))x + B(\kappa(x))u$. The definition of $A(\kappa(x))$ would affect the conservativeness of the control analysis and design.

The Quasi-LPV control has been shown to be a powerful nonlinear design tool. In [29], a Quasi-LPV H_∞ controller is designed for an aircraft model in which a single quadratic Lyapunov function is used and the Quasi-LPV control allows arbitrarily fast parameter variations. An induced L_2-norm control for a Quasi-LPV system is given in [30] and applied to different applications [31], where a parameter-dependent Lyapunov function is utilized for a class of LPV systems that have bounded parameter variation rates.

First, we will introduce the definitions of *Polytopic LPV systems* and *Quadratic* H_∞ *performance* as originally stated in [29].

Definition 4.1.1 [29] (*Polytopic LPV systems*.) An LPV system

$$\begin{aligned} \dot{x} &= A(\kappa)x + B(\kappa)u \\ y &= C(\kappa)x + D(\kappa)u \end{aligned} \tag{4.1}$$

is called polytopic when it can be represented by state-space matrices $A(\kappa)$, $B(\kappa)$, $C(\kappa)$ and $D(\kappa)$, where the dependence of $A(.)$, $B(.)$, $C(.)$ and $D(.)$ on κ is affine, and the parameter vector κ ranges over a fixed polytope as shown below,

$$\begin{aligned} &\begin{pmatrix} A(\kappa) & B(\kappa) \\ C(\kappa) & D(\kappa) \end{pmatrix} = \left\{ \sum_{i=1}^{r} \lambda_i \begin{pmatrix} A(\kappa_i) & B(\kappa_i) \\ C(\kappa_i) & D(\kappa_i) \end{pmatrix} : \lambda_i \geq 0, \sum_{i=1}^{r} \lambda_i = 1 \right\} \\ &\kappa \in \Omega = \left\{ \sum_{i=1}^{r} \lambda_i \kappa_i : \lambda_i \geq 0, \sum_{i=1}^{r} \lambda_i = 1 \right\} \end{aligned} \tag{4.2}$$

Definition 4.1.2 [29] (*Quadratic* H_∞ *performance.*) The LPV system in Eq. 4.1 has quadratic H_∞ performance γ if the L_2 gain of the input/output map is bounded by γ. That is, $\|y\|_2 < \gamma \|u\|_2$ along all possible parameter trajectories κ. The LPV system has quadratic H_∞ performance γ if and only if there exists a single matrix $X > 0$ such that

$$\Re_{[A,B,C,D]}(X,\gamma) := \begin{pmatrix} A(\kappa)^T X + XA(\kappa) & XB(\kappa) & C(\kappa)^T \\ B(\kappa)^T X & -\gamma I & D(\kappa)^T \\ C(\kappa) & D(\kappa) & -\gamma I \end{pmatrix} < 0 \qquad 4.3$$

for all admissible values of the parameter vector κ. □

The definition for the Quadratic H_∞ performance is a straightforward extension of the bounded real lemma for linear-time invariant systems. The Lyapunov function $V(x) = x^T Xx$ establishes global asymptotic stability, and the L_2 gain of the input/output map is bounded by γ. For a polytopic LPV system, using convexity, it is easily shown that Eq. 4.3 is equivalent to $\Re_{[A,B,C,D]}(X,\gamma) < 0$, which holds at the vertices $(A(\kappa_i), B(\kappa_i), C(\kappa_i), D(\kappa_i))$ for $i = 1,...,r$. While for a LPV system which is not polytopic, the parameter-dependent LMI in Eq. 4.3 is often solved by gridding the space of scheduling parameters. However, when the dimension of the scheduling parameters increases, the computational complexity will increase.

For a polytopic LPV system, an output feedback LPV controller can then be designed to achieve the Quadratic H_∞ performance. The state-space matrices of the controller are convex combination of vertex controller matrices; i.e., the LPV controller has the following state matrices $(A_c(\kappa), B_c(\kappa), C_c(\kappa), D_c(\kappa))$:

$$\begin{pmatrix} A_c(\kappa) & B_c(\kappa) \\ C_c(\kappa) & D_c(\kappa) \end{pmatrix} = \sum_{i=1}^{r} \lambda_i \begin{pmatrix} A_{ci} & B_{ci} \\ C_{ci} & D_{ci} \end{pmatrix} \qquad 4.4$$

where the vertex controller $(A_{ci}, B_{ci}, C_{ci}, D_{ci})$ is an LTI H_∞ controller for the LPV system at the *i*th vertex of the parameter polytope, and can be calculated after computing a common Lyapunov function. The Lyapunov function is used for H_∞ control design at all vertices and can be calculated in terms of the solutions to a set of LMIs [29]. Though the vertex controllers can be computed offline, the LPV controller matrices $(A_{ci}, B_{ci}, C_{ci}, D_{ci})$ must be updated in real time based on the measurement κ.

Quadratic H_∞ performance is a strong notion of H_∞ performance in the sense that it holds for arbitrarily fast variation along the parameter trajectories. In [30] and [48], based on parameter-dependent Lyapunov functions, the Quadratic H_∞ performance notion is generalized to an induced L_2 norm performance measure for LPV systems with bounded parameter variation rate. A sufficient condition to test if the induced L_2 norm of an LPV system is less than some γ>0 is also formulated. By incorporating the known bounds on the rate of parameter variation into analysis and design, the parameter-dependent Lyapunov functions could reduce the conservativeness in control analysis and design. An example which can not be stabilized based on parameter-independent Lyapunov functions but otherwise is possible by using parameter-dependent Lyapunov functions is presented in [48]. However, a parameter-dependent Lyapunov function leads to local stability rather than global stability in the sense that it can guarantee stability only if the rate of parameter variation is within certain bounds. If the bounds on the rate of parameter variation are unknown, the parameter-dependent Lyapunov functions are not applicable.

4.2 Formulating the Benchmark Model into a Quasi-LPV System

In this chapter, we first reformulate the Benchmark model into a Quasi-LPV system, and then design a LPV H_∞ controller. Essentially we model the nonlinear planing force into a Quasi-LPV form by including the vertical speed w in the scheduling variable. Note that in the dive-plane model of the Benchmark Model in Eq. 2.31, the planing force and moment are the only nonlinear terms, and it is assumed that the planing force depends entirely on the vertical velocity *w*. We recast the dive-plane dynamics as a Quasi-LPV system in which a function of the vertical velocity w is specified as the time-varying scheduling parameter. Note that we will adopt the LPV control from [29], which is applicable to Quasi-LPV systems with arbitrarily fast parameter variations rather than the LPV control from [30, 48], which uses parameter variation rates. We do this because we do not have access to the variation rate of the vertical velocity *w*. However, if the variation rate *w* is available, the Quasi-LPV control from [30, 48] can be used to reduce the conservativeness of the control.

Eq. 2.17 shows that the planing force depends entirely on the vertical speed *w* once the model configuration has been determined. A normalized planing force $F_{plane}^{\Lambda} = \dfrac{F_{plane}^{z}}{\pi\rho m R^2 L}$ is plotted in Fig. 4-1, where system parameters from Appendix D are used. We rewrite F_{plane}^{Λ} as, $F_{plane}^{\Lambda} = \kappa(w)\cdot w$, $w \in (-\infty, \infty)$, $\kappa(w): R^1 \to R^1$. As shown in the second subfigure of Fig. 4-1, $\kappa(w)$ is bounded for all vertical velocity w; i.e., $\kappa(w) \in [\underline{\kappa}, \overline{\kappa}]$ for certain bounds $\underline{\kappa}$ and $\overline{\kappa}$. With the system parameters from Appendix D, Fig. 4-1 shows that $\kappa(w) \in (-25, 0]$.

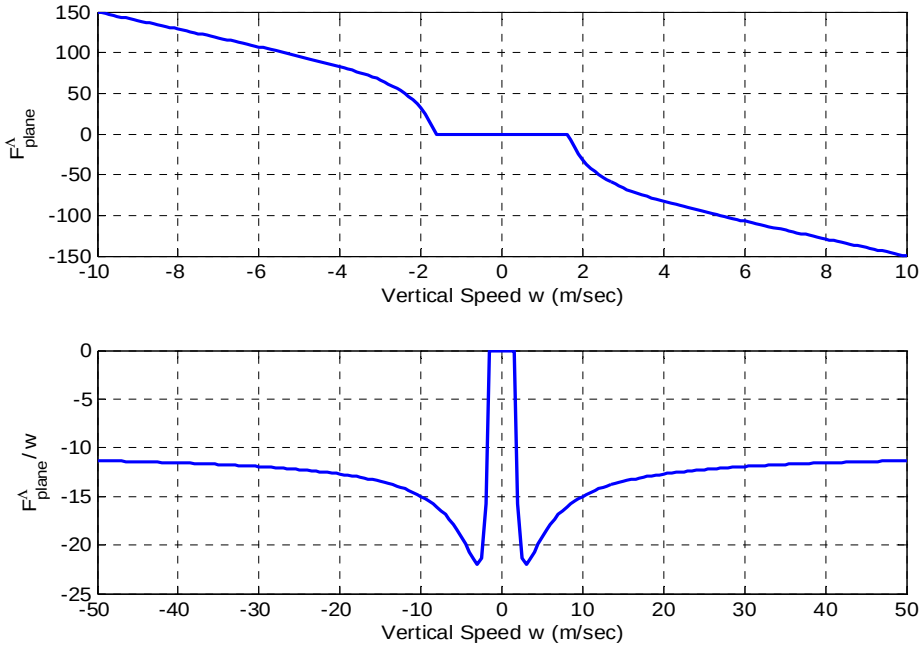

Figure 4-1: Normalized planing force F_{plane}^{Λ} (m/sec^2) and F_{plane}^{Λ} / w.

By $F_{plane}^{\Lambda} = \kappa(w) \cdot w$, Eq. 2.31 can be rewritten in the following form:

$$\dot{z} = w - V\theta$$
$$\dot{\theta} = q$$
$$M_I \begin{bmatrix} \dot{w} \\ \dot{q} \end{bmatrix} = A_I \begin{bmatrix} w \\ q \end{bmatrix} + B_I \begin{bmatrix} \delta_f \\ \delta_c \end{bmatrix} + F_{grav}^{\Lambda} + \begin{bmatrix} \kappa(w) \\ \kappa(w) \cdot L \end{bmatrix} w \qquad 4.5$$
$$= (A_I + \begin{bmatrix} \kappa(w) & 0 \\ \kappa(w) \cdot L & 0 \end{bmatrix}) \begin{bmatrix} w \\ q \end{bmatrix} + B_I \begin{bmatrix} \delta_f \\ \delta_c \end{bmatrix} + F_{grav}^{\Lambda}$$

where M_I, A_I, B_I and F_{grav}^{Λ} are defined in Eq. 2.30 and Eq. 2.32. Define $H(\kappa(w)) = M_I^{-1}(A_I + \begin{bmatrix} \kappa(w) & 0 \\ \kappa(w)\cdot L & 0 \end{bmatrix})$, $E = M_I^{-1}B_I$, $\begin{bmatrix} \delta_{f0} \\ \delta_{c0} \end{bmatrix} = -B_I^{-1}\cdot F_{grav}^{\Lambda}$, and then Eq. 4.5 can be further written as,

$$\begin{aligned} \begin{bmatrix} \dot{z} \\ \dot{\theta} \\ \dot{w} \\ \dot{q} \end{bmatrix} &= \begin{bmatrix} 0 & -V & 1 & 0 \\ 0 & 0 & 0 & 1 \\ 0 & 0 & H_{11}(\kappa(w)) & H_{12}(\kappa(w)) \\ 0 & 0 & H_{21}(\kappa(w)) & H_{22}(\kappa(w)) \end{bmatrix} \begin{bmatrix} z \\ \theta \\ w \\ q \end{bmatrix} + \begin{bmatrix} 0 & 0 \\ 0 & 0 \\ E_{11} & E_{12} \\ E_{21} & E_{22} \end{bmatrix} \begin{bmatrix} v_f \\ v_c \end{bmatrix} \\ &\equiv A(\kappa(w)) \begin{bmatrix} z \\ \theta \\ w \\ q \end{bmatrix} + G \begin{bmatrix} v_f \\ v_c \end{bmatrix} \end{aligned} \qquad 4.6$$

where $\begin{bmatrix} v_f \\ v_c \end{bmatrix} = \begin{bmatrix} \delta_f \\ \delta_c \end{bmatrix} - \begin{bmatrix} \delta_{f0} \\ \delta_{c0} \end{bmatrix}$, and H_{ij} and E_{ij} ($i, j = 1,2$) are elements of H and E, respectively.

The system in Eq. 4.6 is a Quasi-LPV system, as the dynamic matrix $A(\kappa(w))$ is a function of the state w. Note that by specifying $\kappa(w)$ as the scheduling parameter, we make elements of $A(\kappa(w))$ linearly dependent on the parameter $\kappa(w)$.

4.3 Constant-Gain State Feedback Controller

We first design a constant-gain state feedback controller for the Quasi-LPV model. Define the control input $\begin{bmatrix} v_f \\ v_c \end{bmatrix} = K\begin{bmatrix} z & \theta & w & q \end{bmatrix}^T$, $K \in R^{2\times 4}$, then the closed-loop system becomes,

$$\begin{bmatrix} \dot{z} & \dot{\theta} & \dot{w} & \dot{q} \end{bmatrix}^T = (A(\kappa(w)) + GK)\begin{bmatrix} z & \theta & w & q \end{bmatrix}^T \tag{4.7}$$

If there exists a constant positive definite matrix P that satisfies,

$$(A(\kappa(w)) + GK)^T P + P(A(\kappa(w)) + GK) < 0, \qquad \forall \kappa(w) \in [\underline{\kappa}, \overline{\kappa}] \tag{4.8}$$

then the closed-loop system is stable. Since $\kappa(w) \in [\underline{\kappa}, \overline{\kappa}]$ and $A(\kappa(w)) + BK$ is an affine function of $\kappa(w)$, it suffices to find a $P > 0$ that satisfies the following [32],

$$\begin{aligned} (A(\underline{\kappa}) + GK)^T P + P(A(\underline{\kappa}) + GK) < 0 \\ (A(\overline{\kappa}) + GK)^T P + P(A(\overline{\kappa}) + GK) < 0 \end{aligned} \tag{4.9}$$

Pre-multiply and post-multiply Eq. 4.9 by $Q = P^{-1}$, and define $J = KQ$, we have

$$\begin{aligned} QA^T(\underline{\kappa}) + A(\underline{\kappa})Q + J^T G^T + GJ < 0 \\ QA^T(\overline{\kappa}) + A(\overline{\kappa})Q + J^T G^T + GJ < 0 \end{aligned} \qquad 4.10$$

which are LMIs in terms of Q and J. Using the system parameters from Appendix D and *Matlab* LMI toolbox, one feasible solution is given as,

$$P = \begin{bmatrix} 357.2128 & -444.6011 & -2.6876 & -1.7733 \\ -444.6011 & 553.3682 & 3.3446 & 2.2071 \\ -2.6876 & 3.3446 & 0.1077 & 0.0133 \\ -1.7733 & 2.2071 & 0.0133 & 0.0088 \end{bmatrix} \qquad 4.11$$

$$K = \begin{bmatrix} -66.585 & 274.4042 & 0.5255 & 4.2448 \\ 7.2456 & -50.8998 & -0.4431 & -0.9768 \end{bmatrix}$$

and the controller is

$$\begin{bmatrix} \delta_f \\ \delta_c \end{bmatrix} = -B_I^{-1} F_{grav}^{\wedge} + K \begin{bmatrix} z & \theta & w & q \end{bmatrix}^T \qquad 4.12$$

4.4 Quasi-LPV H_∞ Controller

Considering the dive-plane dynamics in Eq. 4.6, $A(\kappa(w))$ is affine dependent on the scheduling parameter $\kappa(w)$, and thus we apply the algorithm from [29] to design the Quasi-LPV H_∞ controllers for Eq. 4.6. Since the algorithm from [29] has been coded in the *MATLAB* toolbox and thus in this chapter, we use the *MATLAB* toolbox directly and

omit the algorithm details here. The only design parameters for the delay-independent Quasi-LPV H_∞ controller design required by the *MATLAB* toolbox are the weighting functions.

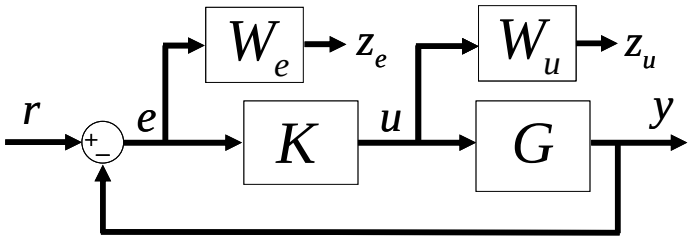

Figure 4-2: Control structure in the Quasi-LPV H_∞ controller design.

Fig. 4-2 shows the block diagram of the Quasi-LPV H_∞ controller, where the block *G* represents the plant of the supercavitating vehicle, the block *K* represents the Quasi-LPV H_∞ controller, and *r* denotes the reference signal. The performance-tracking weighting function W_e and the control-input weighting function W_u are designed as follows:

$$W_e = diag\{W_1, W_1, W_2, W_2\},\ W_u = W_3 I_{2\times 2} \qquad 4.13$$

where $I_{2\times 2}$ denotes the 2×2 identity matrix. W_1, W_2 and W_3 are listed in Tab. 4-1.

Table 4-1: Weighting functions for the Quasi-LPV H_∞ controller (QLPVHC)

Weighting Function	Value
W_1	$\frac{1500}{s+2}$
W_2	150
W_3	$\frac{200s}{s+250}$

The tracking-performance weights $W_1 = \frac{1500}{s+2}$ and $W_2 = 150$ are designed to emphasize low-frequency tracking and minimize steady-state error. The actuator weight $W_3 = \frac{200s}{s+250}$ is designed to penalize high-frequency noise under the consideration of the actuator bandwidth. Note that for the simulations conducted in [18], same first-order actuator models were used for both the cavitator and fin control. In this chapter, we apply a similar actuator model of transfer function $\frac{300}{s+300}$ in our simulations later in the chapter. Hence the weights for the cavitator and fin control inputs are chosen to be the same. However, if actuator models with different bandwidth are considered for the cavitator and fin control, different control weights should be designed for the cavitator and fin.

4.5 Simulation Results

In this section, we present simulation results for the Quasi-LPV H_∞ controller (QLPVHC). First, we will present the results of the simulations that do not include the

high-gain observer. Note that the Quasi-LPV H_∞ controller (QLPVHC) is an output feedback controller as mentioned before [29-31, 48]. However, the high-gain observer is needed to provide the w value for updating the LPV controller, which is scheduled by a function of w. Then, we will present the simulation results for the controller combineing the Quasi-LPV H_∞ controller (QLPVHC) with the high-gain observer.

In order to achieve results that can be compared with the results from [1] and [4], initial responses are simulated under the initial conditions of $z = 0, \theta = 0, w = 3m/sec$, and $q = 0.2rad/sec$. Additional tracking responses are also simulated to further evaluate the controllers' performance. The numerical example used in the following simulations is based on the parameter values in Appendix D from [1].

The first-order actuator model of the transfer function $\frac{300}{s+300}$ is used for both the cavitator and the fin control in the simulations presented in this section. In addition, we assume that the actuators are subject to amplitude limits of $|\delta_c| \le 25 \ \ deg$ and $|\delta_f| \le 25 \ \ deg$, and a rate limit of 100 rad/sec [18]. We note that δ_f over a high angle may compromise control effectiveness. In the rest of this section, we let saturation compensation (SC) denote the simulations with the above-mentioned actuator model and actuation limits (but augmented by the saturation compensation once the amplitude limit has been touched). We let unlimited control (UC) represent the simulations with ideal actuators.

As in Chapter 3, we evaluate the robustness of the Quasi-LPV H_∞ controller

(QLPVHC) to uncertainties such as variations in the parameters $\frac{C_x}{m}$ and n. The same variation range as in Chapter 3 is used. We also use the Time-Delay Benchmark Model to evaluate the system performance, although the memory effect of the cavity-vehicle interaction is not included in the Benchmark Model used for the control design.

4.5.1 Simulation Results without the High-gain Observer

A. Nominal performance

Fig. 4-3 plots the initial-response time histories of the state, control, and planing force for the nominal closed-loop systems in which the Quasi-LPV H_∞ controller (QLPVHC) with either the unlimited control (UC) or the saturation compensation (SC) is applied. In this initial response, the Benchmark Model without the cavity memory effect is used. The state in the SC case oscillates more obviously than does the state in the UC case. This is because in the former both the amplitude and rate limits of δ_f and δ_c are touched, and thus the saturation compensation coordinates the two controls to maintain the system's stability. We have learned from our simulations that if actuation amplitude limits are imposed but no saturation compensation is implemented, the closed-loop system will become unstable.

Fig. 4-4 plots the initial-response time histories of the state, control, and planing force for the nominal closed-loop systems in which the Quasi-LPV H_∞ controller (QLPVHC) controller with saturation compensation (SC) is applied. In this figure, we show both simulations with and without memory effect due to the cavity-vehicle

interaction. The planing force model without memory effect is described in Eqs. 2.17, 2.24, and 2.25. The model with the memory effect is given in Eqs. 2.17, 2.34, and 2.35 in which the delay time $\tau = L/V$ caused by the memory effect is calculated as $\tau = 0.024$ in terms of the vehicle configuration parameters in Appendix D. Fig. 4-4 shows that the Quasi-LPV H_∞ controller (QLPVHC) can stabilize the nominal system in the presence of the memory effect, though with worse transient performance. It is worth pointing out that in Fig. 4-4, the rate limits for both δ_f and δ_c are touched in the simulation. However, by imposing a hard constraint of 100 rad/sec on the rate limit, the system is still stabilized. In addition, if actuation amplitude limits are imposed but no saturation compensation is implemented, the closed-loop system will become unstable.

The tracking performance of the Quasi-LPV H_∞ controller (QLPVHC) for the nominal system is shown in Figs. 4-5 and 4-6. Here, we consider two tracking reference signals: a unit-step input for depth *z* is used as the reference signal in Fig. 4-5, and the *w*-tracking response is shown in Fig. 4-6, where the reference signal is

$$w_r = 2\sin(2\pi t),\ z_r = 0,\ \theta_r = \frac{w}{V},\ \text{and}\ q_r = \dot{\theta}_r \qquad 4.14$$

According to the Time-Delay Benchmark Model, the small magnitude of the vertical velocity *w* in the simulation shown in Fig. 4-5 would not induce any planing force; while for the *w*-tracking response in Fig. 4-6, planing force occurs and the memory effect in the planing force model has been included in the simulation. Fig. 4-5

shows that the z-step response has settling time less than one sec. Fig. 4-6 shows that in the presence of cavity memory effect, though the LPV H_∞ controller designed with the Benchmark Model can track the reference w_r, the reference trajectory θ_r is not well followed.

B. Robustness Evaluation

To evaluate the robustness of the Quasi-LPV H_∞ controller (QLPVHC), Figs. 4-7 and 4-8 plot the stochastic envelopes of the state, control and planing force histories based on 100 Monte Carlo simulations of the tracking responses (*z*-step response and *w*-tracking response). The planing force is not induced in *z*-step response simulations. Memory effect is considered in *w*-tracking response simulations. The uncertainties used in the Monte Carlo simulations include $\pm 5\%$ variations in the parameters $\frac{C_x}{m}$ and *n*. The random samples are generated using normal distributions, which have zero mean and 0.05 std, and are then truncated within $\pm 5\%$ variation of the nominal values. The stochastic envelopes consist of maximum, mean and minimum values at each time instance. In *z*-step response and *w*-tracking response simulations, Figs. 4-7 and 4-8 show that the Quasi-LPV H_∞ controller (QLPVHC) is robust to system parameter uncertainties, as well as the planing force memory effect, which is not included in the control design. However, we learn that it is very difficult to further let the closed-loop system track pitch angle reference signals satisfactorily by designing suitable weighting functions. In Chapter 5, it will be shown that the Quasi-LPV H_∞ controller (QLPVHC) is not able to

perform pitch angle tracking satisfactorily if the Time-Delay Benchmark Model is used. These observations motivate us to exploit time-delay LPV control techniques to address memory effect explicitly in Chapter 5.

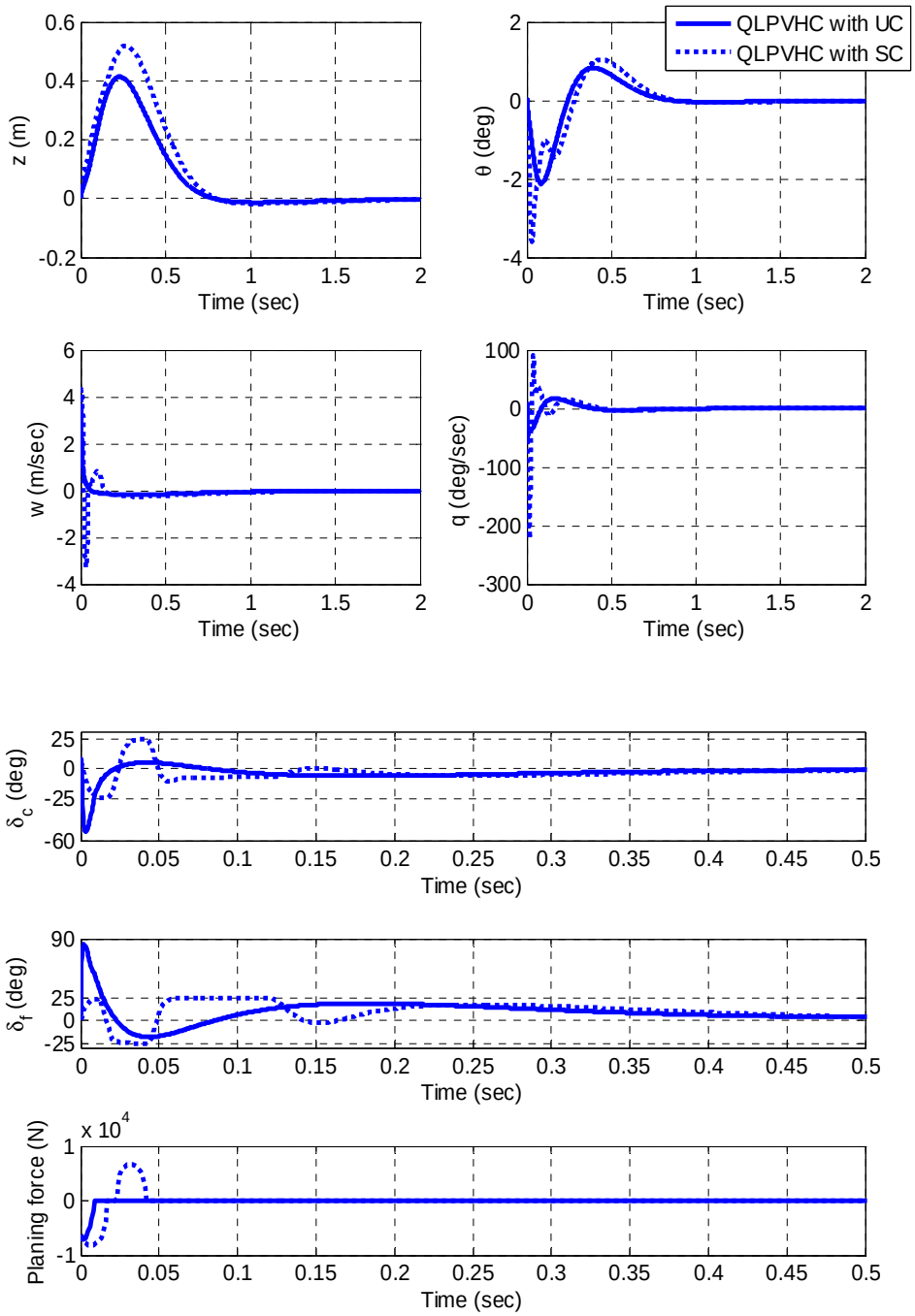

Figure 4-3: Initial responses for nominal systems implemented with the Quasi-LPV H_∞ controller (QLPVHC) with UC and SC, without consideration of cavity memory effect.

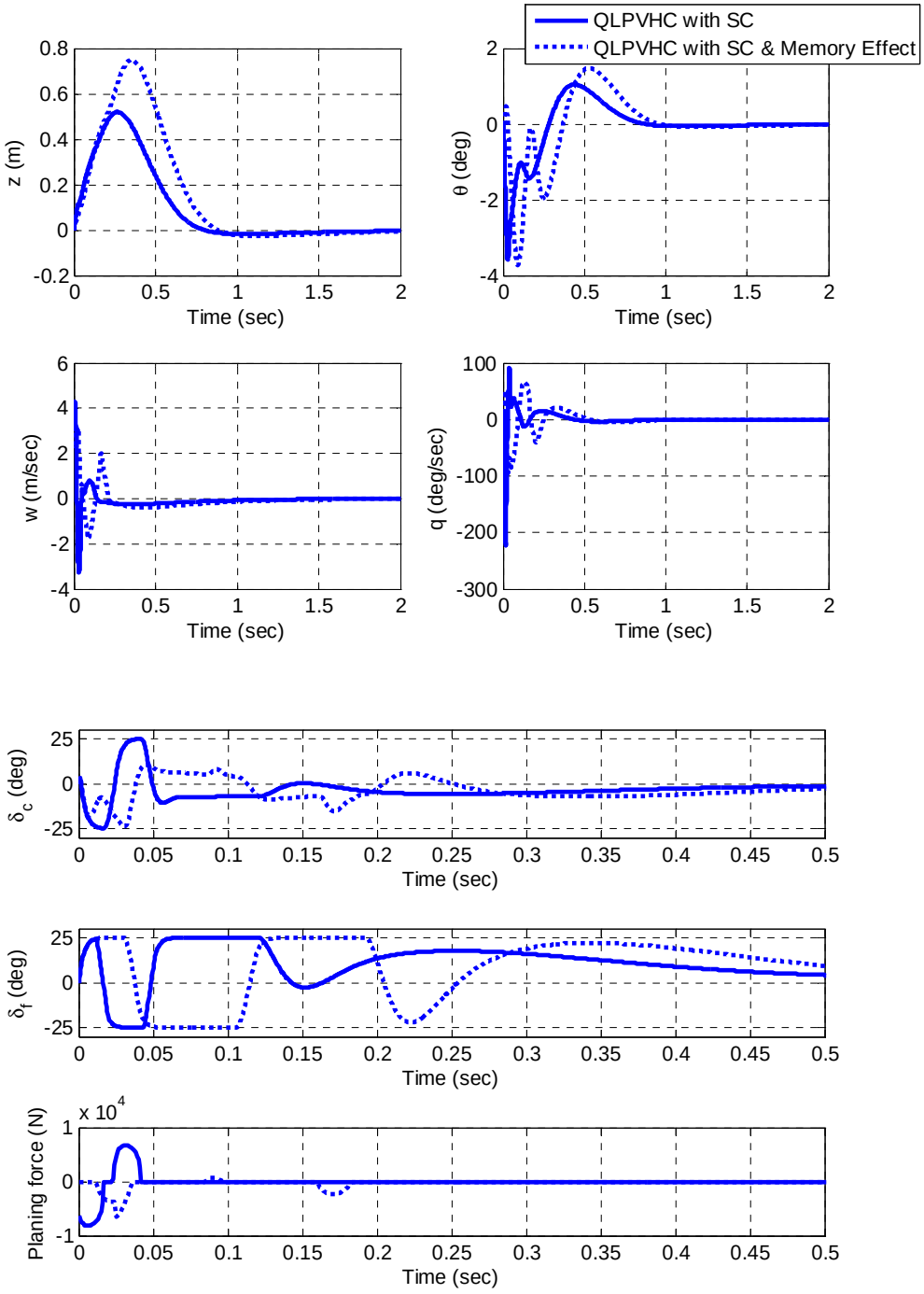

Figure 4-4: Initial responses for nominal systems implemented with the Quasi-LPV H_∞ controller (QLPVHC) with SC, with and without consideration of cavity memory effect.

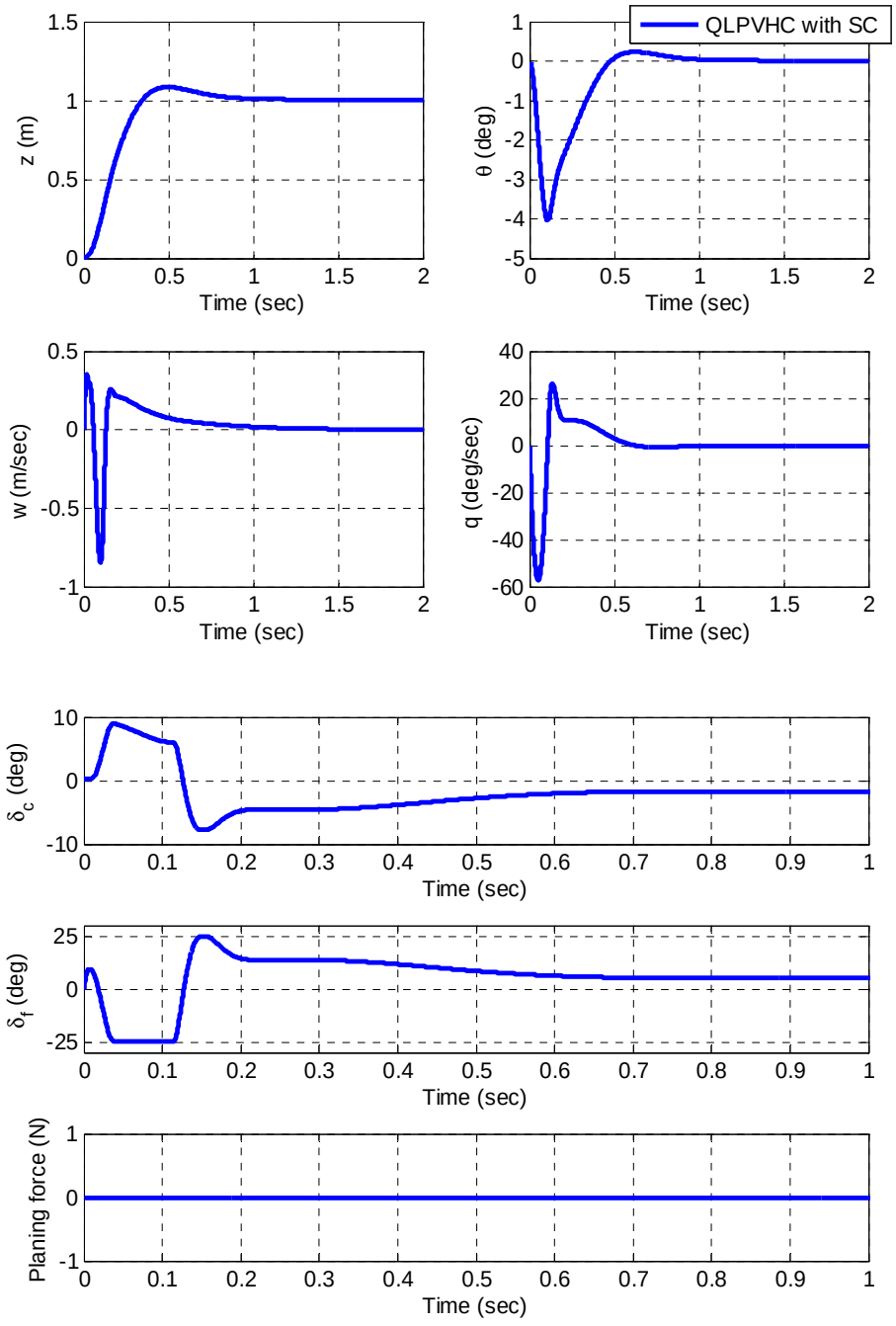

Figure 4-5: z-step response for the nominal system, implemented with the Quasi-LPV H_∞ controller (QLPVHC) with SC. Note no planing force is induced based on either the Benchmark Model or the Time-Delay Benchmark Model.

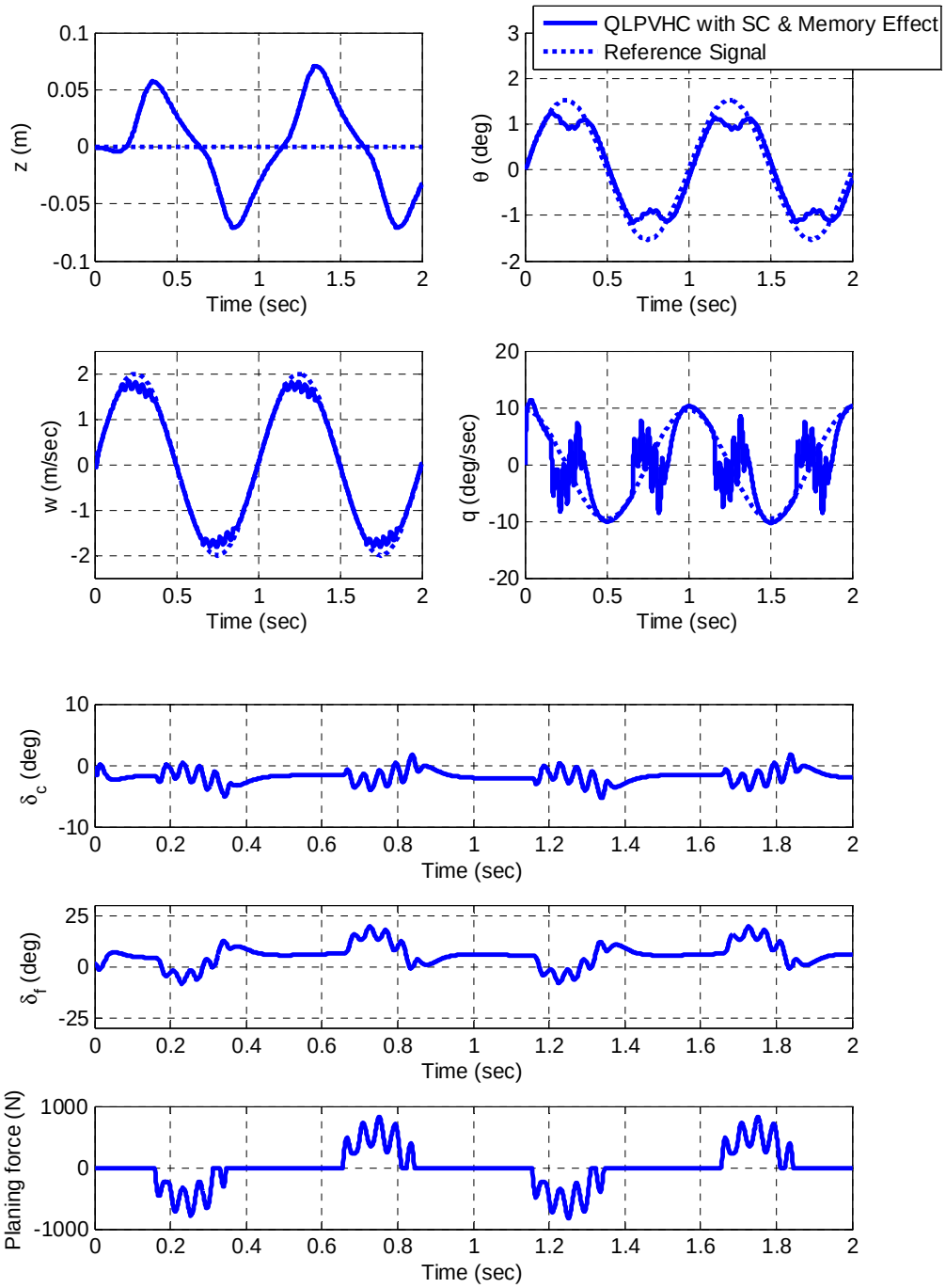

Figure 4-6: w-tracking response for the nominal system, implemented with the Quasi-LPV H_∞ controller (QLPVHC) with SC, with consideration of cavity memory effect.

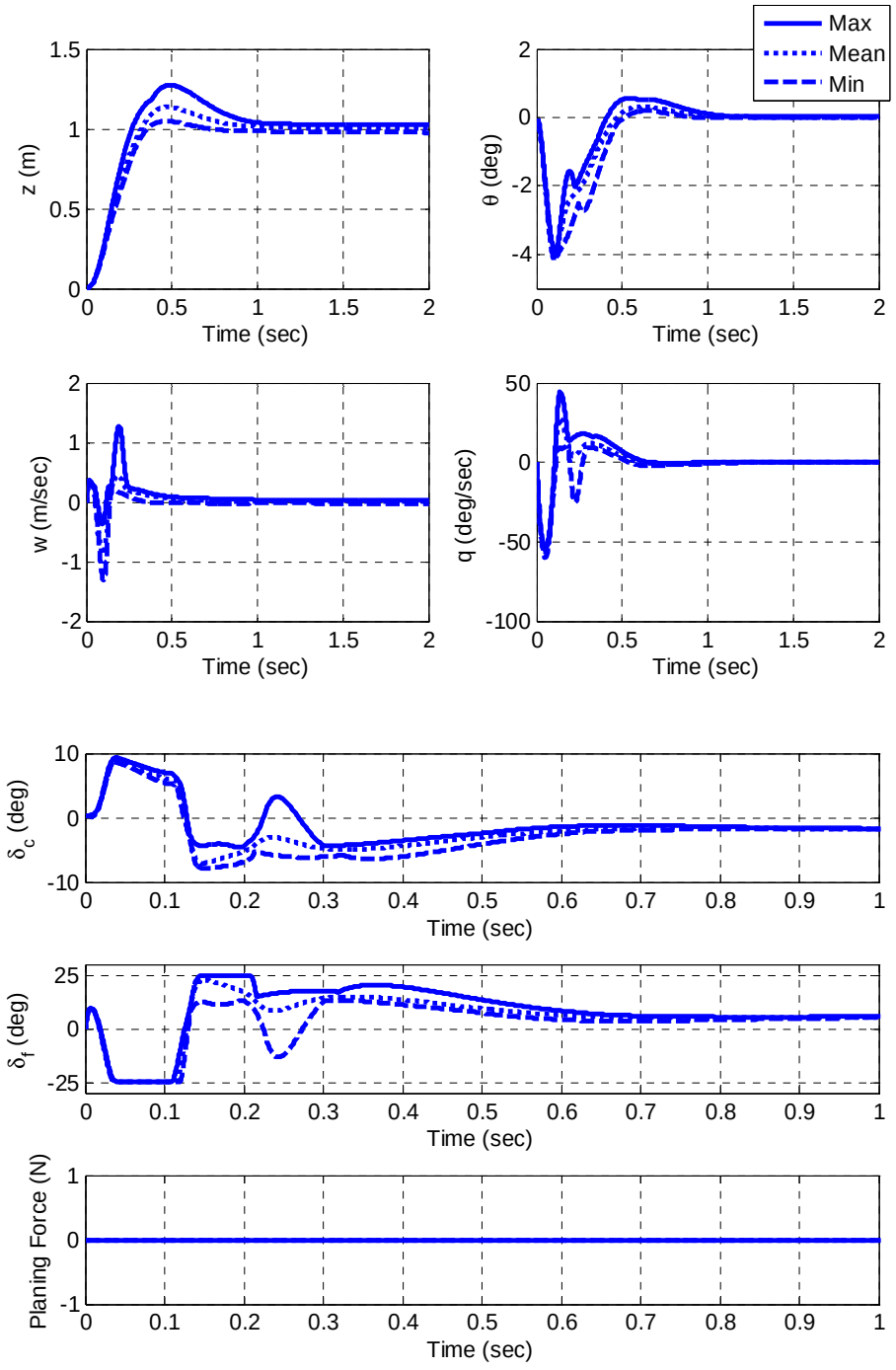

Figure 4-7: Stochastic envelopes of the z-step tracking responses for the uncertain system, implemented with the Quasi-LPV H_∞ controller (QLPVHC) with SC. Note no planing force is induced based on either the Benchmark Model or the Time-Delay Benchmark Model.

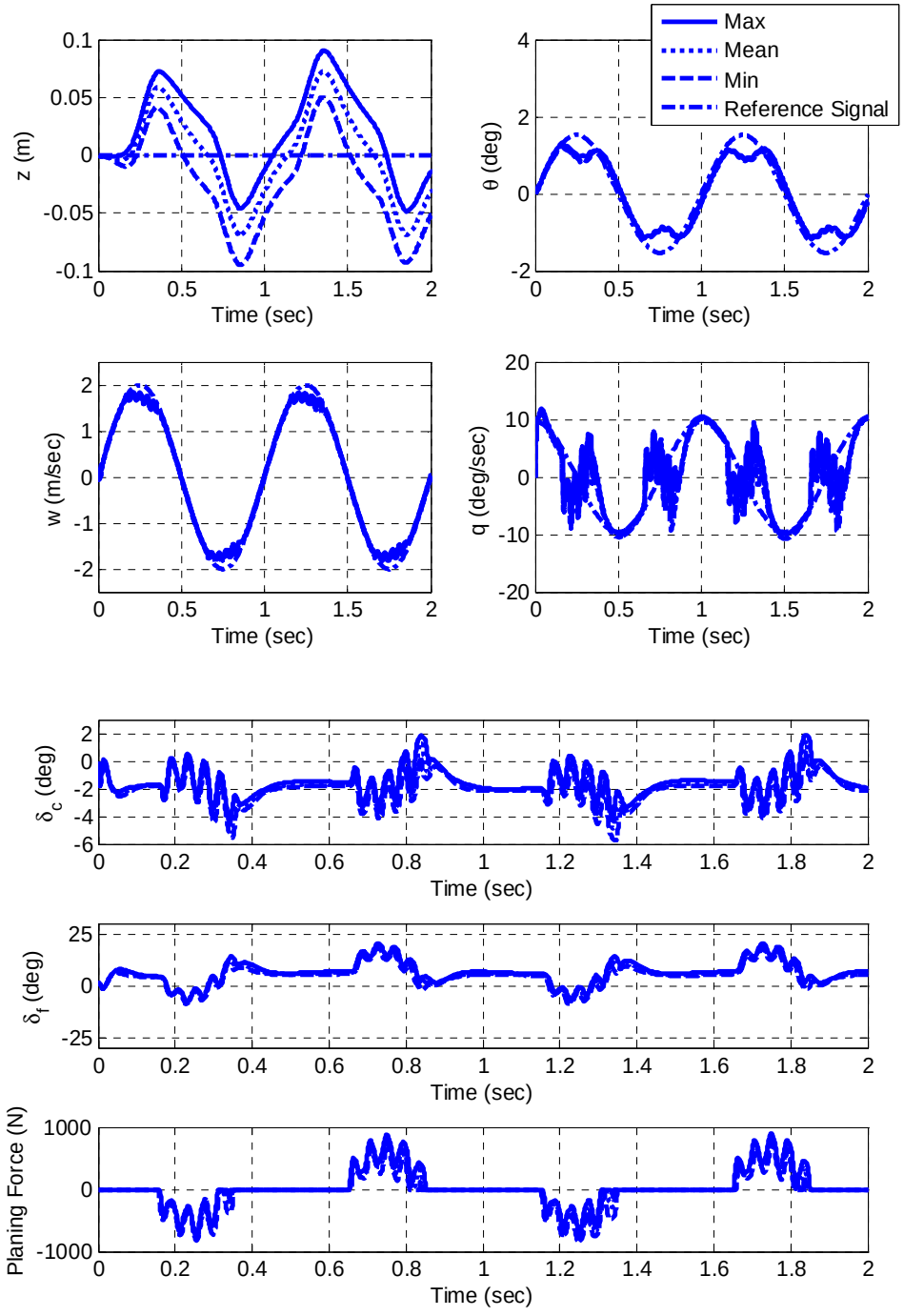

Figure 4-8: Stochastic envelopes of the w-tracking responses for the uncertain system, implemented with the Quasi-LPV H_∞ controller (QLPVHC) with SC, with consideration of cavity memory effect.

4.5.2 Simulation Results with the High-gain Observer

In this section, we repeat all the simulations shown in the last section for the output feedback controllers. The only difference is that here we include the designed high-gain observer by assuming that the vertical velocity w is not available via direct measurement. The high-gain observer parameter is set as ε = 0.00015. For all initial responses, the initial conditions of the high-gain observer are specified as $\hat{z} = 0, \hat{w} = 0$, i.e., the estimated initial $\hat{w}$ is away from its true value.

The simulation results shown in Figs. 4-9 - 4-14 correspond with those shown in Figs. 4-3 - 4-8, respectively. It is clear that the closed-loop systems with the high-gain observer can achieve almost the same performance as the output feedback closed-loop systems without the observer, in both nominal performance and the robustness-testing simulations.

To further explore the performance of the observer, Fig. 4-15 shows the time histories of the estimation errors e_z and e_w (as defined in Eq. 3.32). Specifically, the figure shows the errors when the observer is implemented with the Quasi-LPV H_∞ controller (QLPVHC) in the initial responses in which the high-gain observer parameter is set as ε = 0.00015. Recall that the initial conditions of the high-gain observer are specified as $\hat{z} = 0, \hat{w} = 0$; i.e., the estimated initial $\hat{w}$ is away from its true value of $w = 3m/sec$. We can see that the state estimation errors converge to zero quickly despite the uncertain nonlinear part $o(z, w, \hat{z}, \hat{w})$ of Eq. 3.33. This is because the transfer

function from $o(z, w, \hat{z}, \hat{w})$ to the estimation errors is almost zero due to the high gain of the observer.

Here, we also use simulations to show how the high-gain observer behaves under sensor noise conditions. In the presence of the sensor measurement noise of *z*, Fig. 4-16 plots the initial responses corresponding to the Quasi-LPV H_∞ controller (QLPVHC) combined with a high-gain observer. The sensor measurement noise used in the simulations in Fig. 4-16 is white noise with a power of 10^{-8} and a sample time of 0.001 sec. Following the discussions in [28], we reset the high-gain observer design parameter $\varepsilon = 0.002$ for the Quasi-LPV H_∞ controller (QLPVHC). Note that the ε value is fine-tuned for the Quasi-LPV H_∞ controller (QLPVHC) to balance the minimization of state estimation errors against amplification of sensor noise. It is observed that the controller is still able to stabilize the system, even though there are oscillations in control inputs δ_c and δ_f. It is also noted that the rate limit for both δ_f and δ_c is reached, as shown in Fig. 4-16.

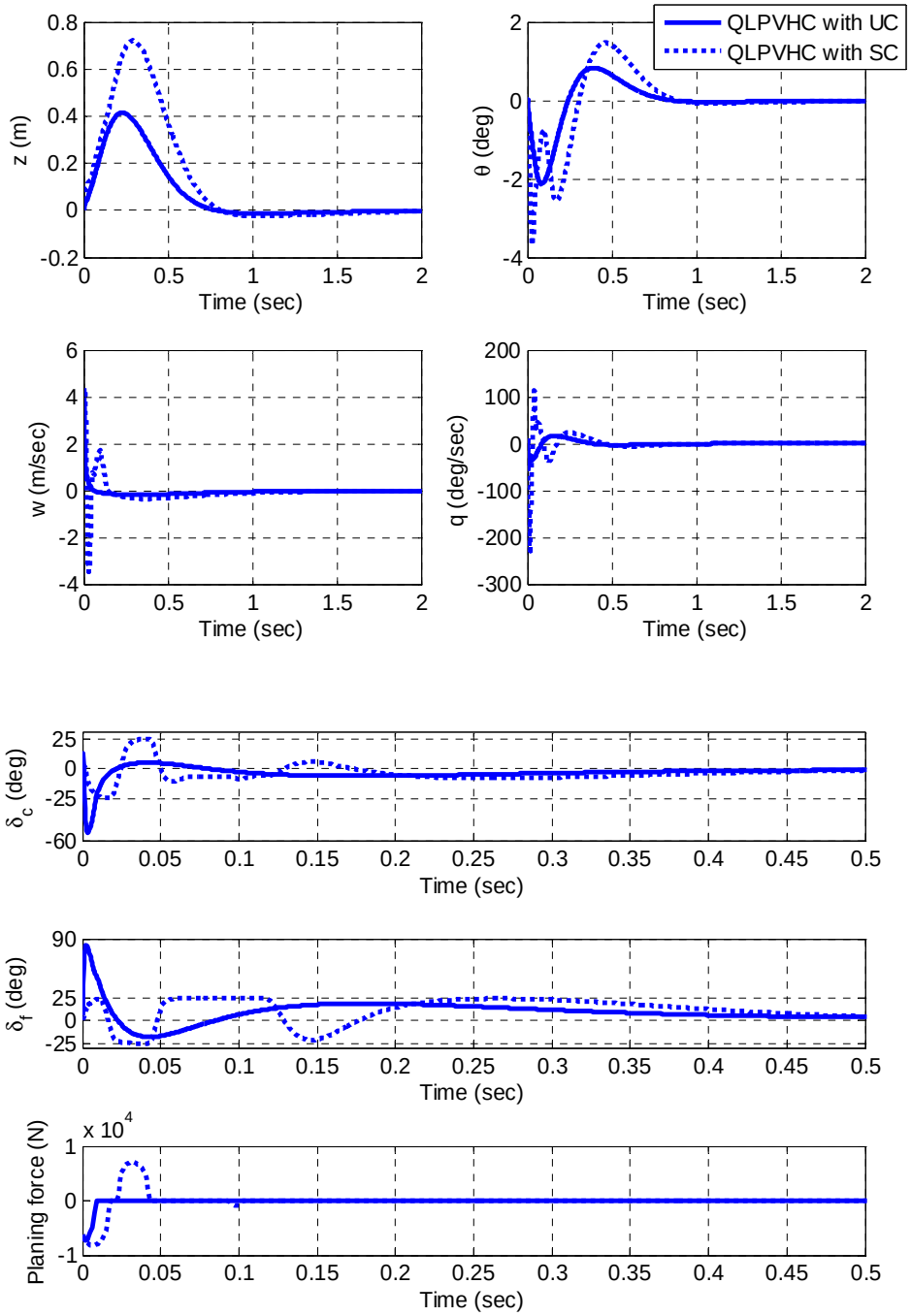

Figure 4-9: Initial responses for nominal systems implemented with the Quasi-LPV H_∞ controller (QLPVHC) with UC and SC, without consideration of cavity memory effect. The high-gain observer is also included in the simulations.

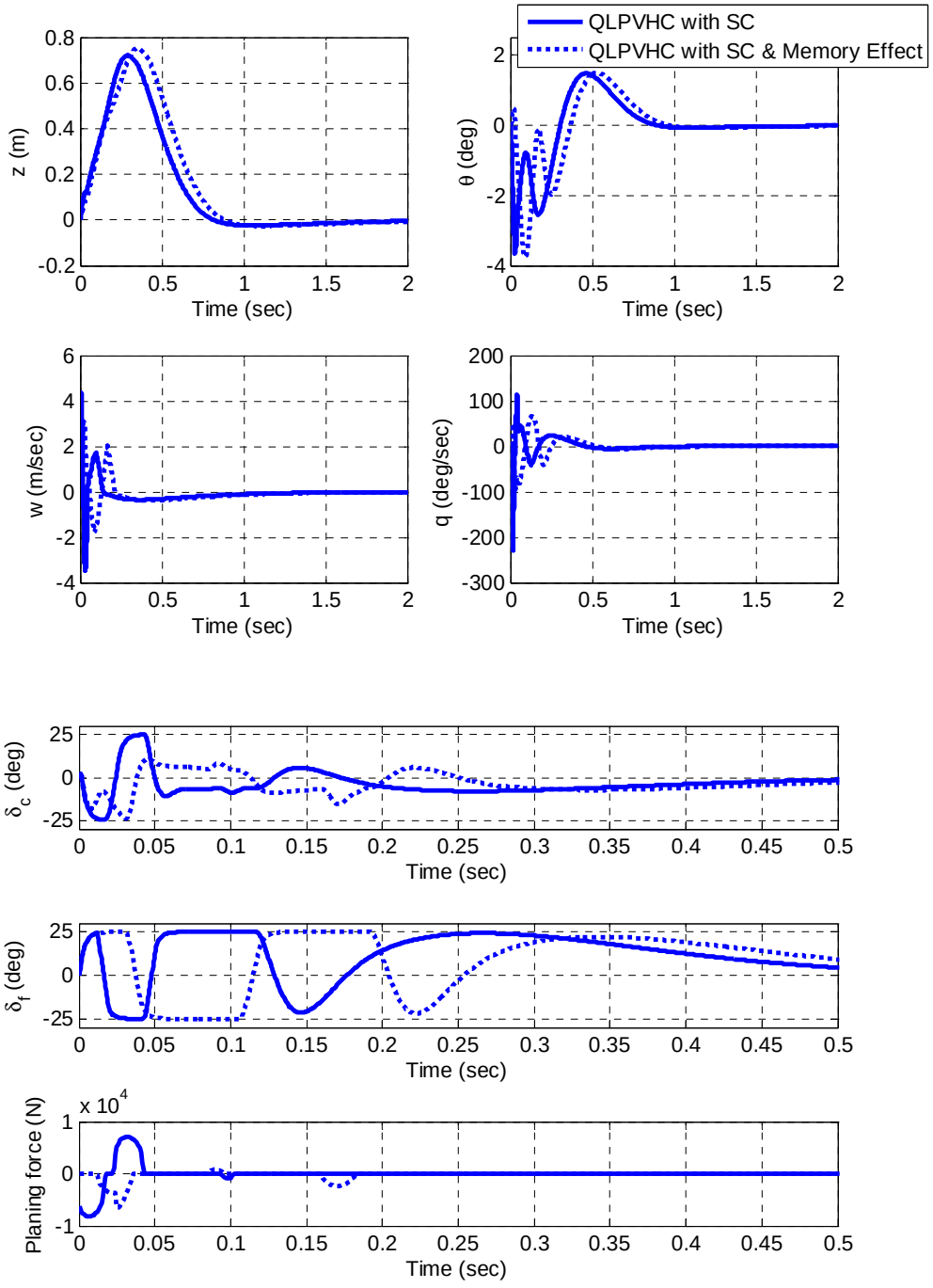

Figure 4-10: Initial responses for nominal systems implemented with the Quasi-LPV H_∞ controller (QLPVHC) with SC, with and without consideration of cavity memory effect. The high-gain observer is also included in the simulations.

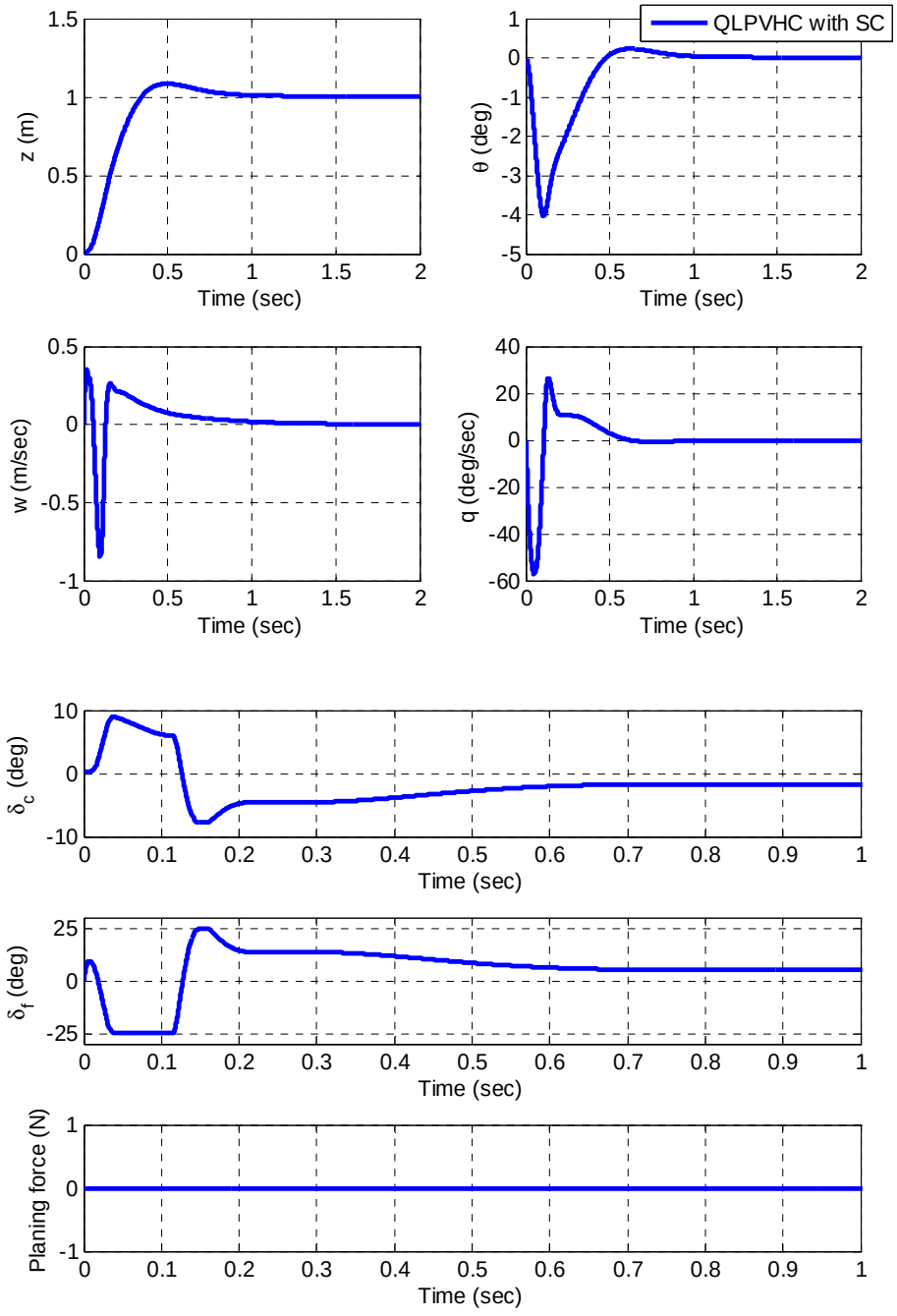

Figure 4-11: z-step response for the nominal system, implemented with the Quasi-LPV H_∞ controller (QLPVHC) with SC, with consideration of cavity memory effect. The high-gain observer is also included in the simulations. Note no planing force is induced based on either the Benchmark Model or the Time-Delay Benchmark Model.

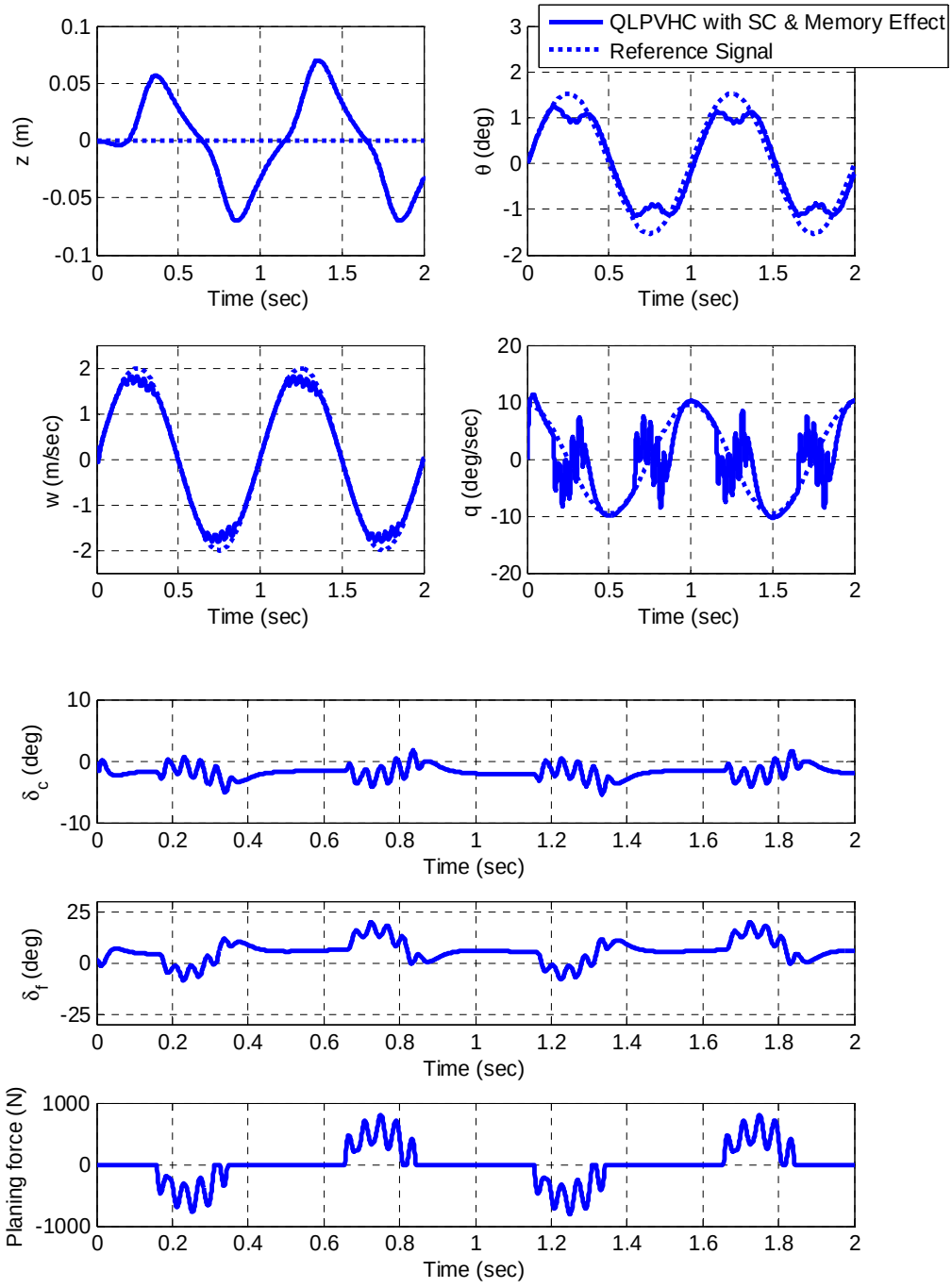

Figure 4-12: w-tracking response for the nominal system, implemented with the Quasi-LPV H_∞ controller (QLPVHC) with SC, with consideration of cavity memory effect. The high-gain observer is also included in the simulations.

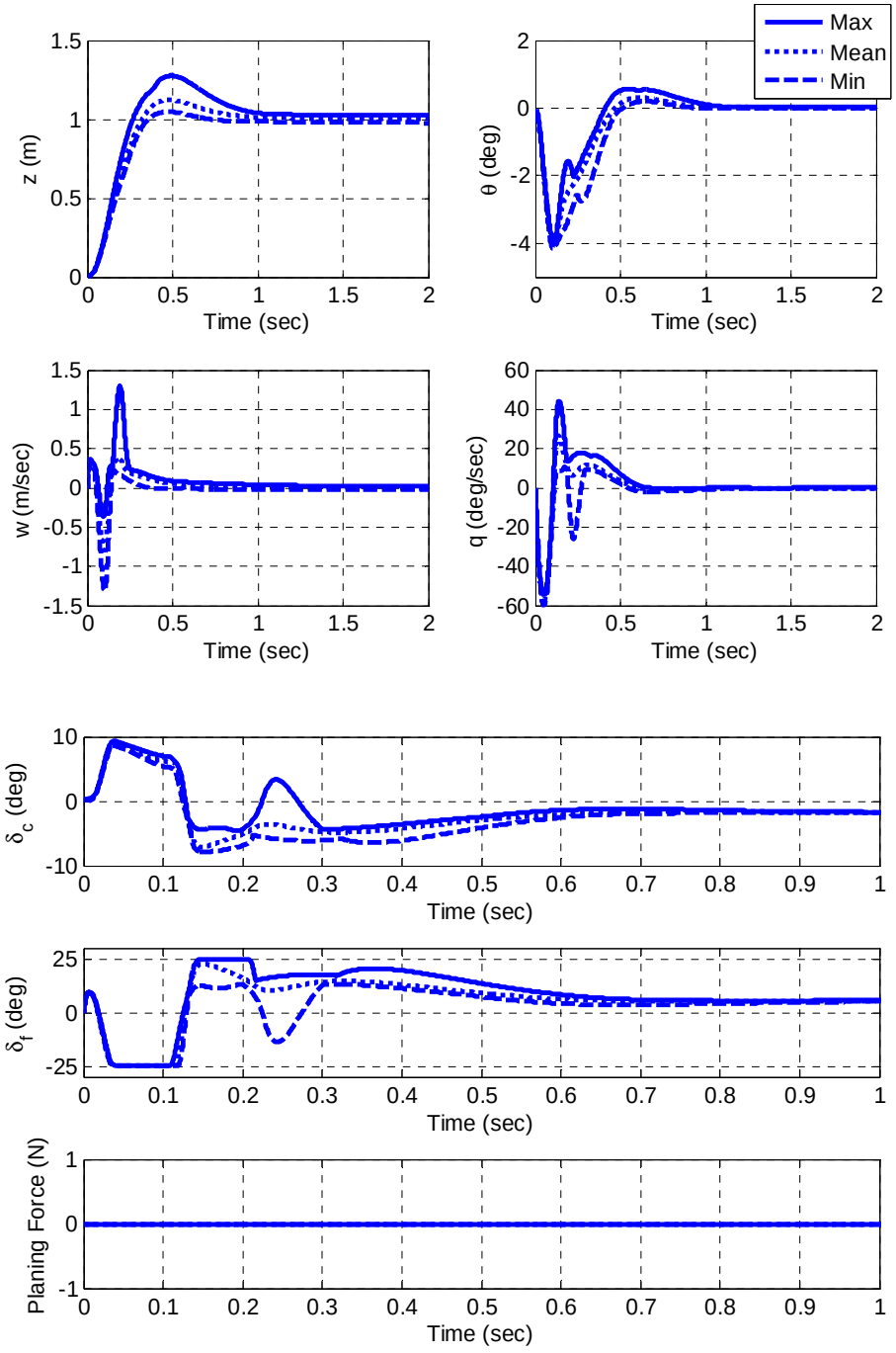

Figure 4-13: Stochastic envelopes of the z-step tracking responses for the uncertain system, implemented with the Quasi-LPV H_∞ controller (QLPVHC) with SC. The high-gain observer is also included in the simulations. Note no planing force is induced based on either the Benchmark Model or the Time-Delay Benchmark Model.

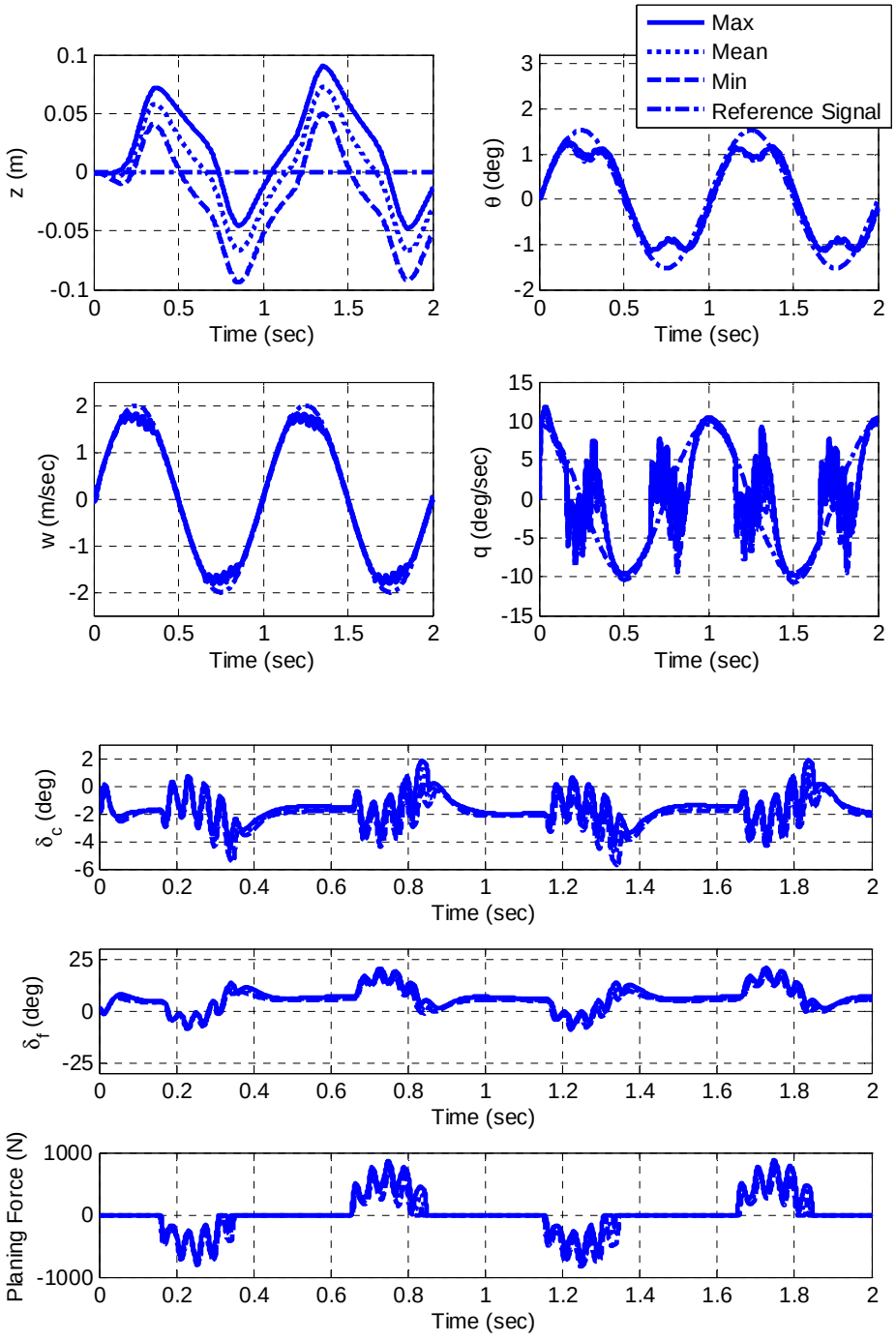

Figure 4-14: Stochastic envelopes of the w-tracking responses for the uncertain system, implemented with the Quasi-LPV H_∞ controller (QLPVHC) with SC, with consideration of cavity memory effect. The high-gain observer is also included in the simulations.

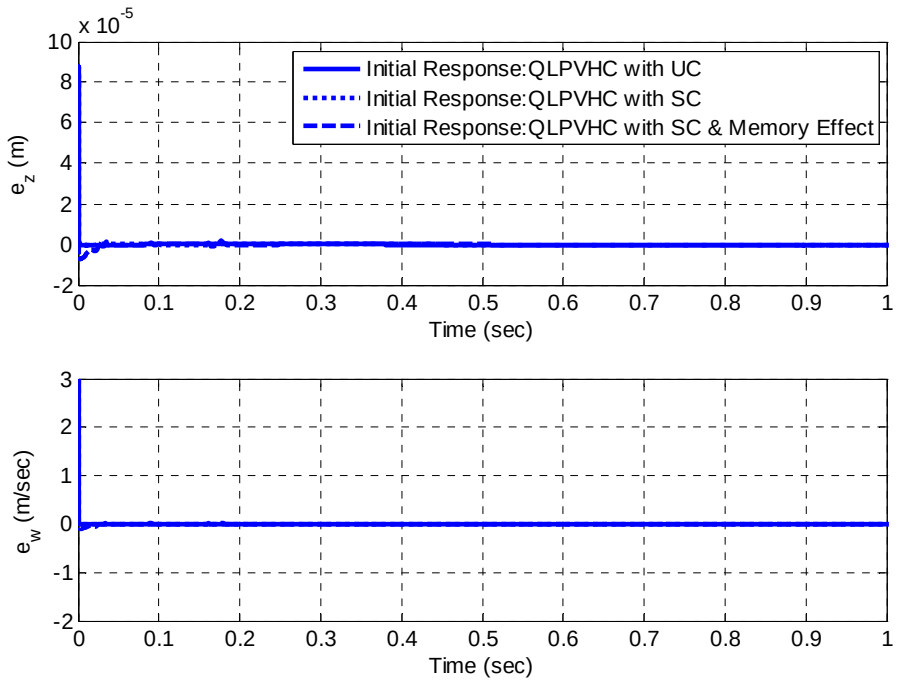

Figure 4-15: Performance of the high-gain observer in closed-loop systems implemented with the Quasi-LPV H_∞ controller (QLPVHC). No measurement noise is considered.

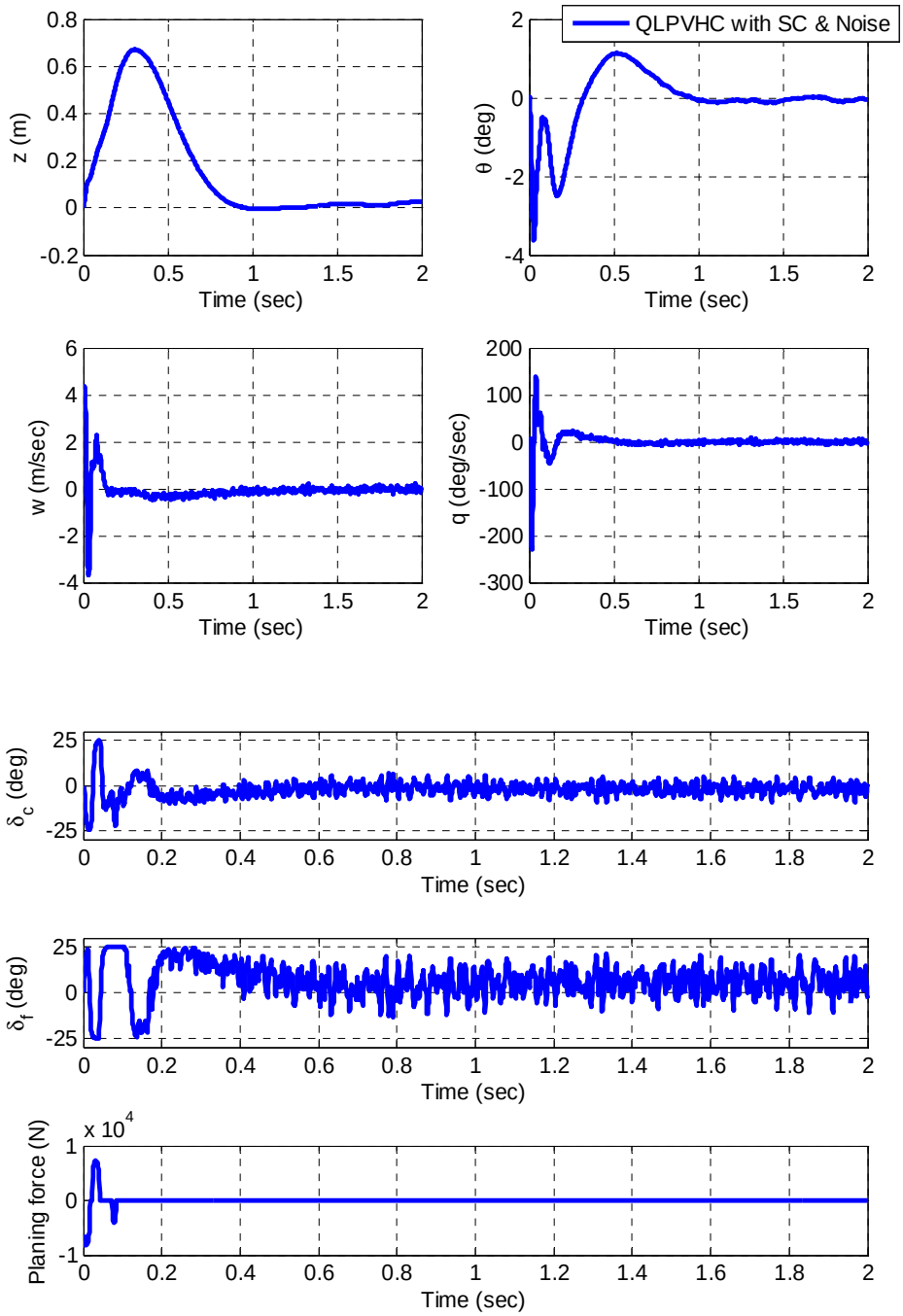

Figure 4-16: Sensitivity of initial response to measurement noise in z, under the Quasi-LPV H_∞ controller (QLPVHC) with SC and the high-gain observer.

4.6 Compared with the Sliding-Mode Controller

Note that the sliding-mode controller (SMC) designed in Chapter 3 and the Quasi-LPV H_∞ controller (QLPVHC) are designed to meet different objectives: the former emphasizes robustness with respect to the uncertainties of the system parameters, the hydrodynamic coefficients, and the planing force, whereas the latter optimizes the H_∞ norm of the performance. Based on our simulations, we consider that the Quasi-LPV H_∞ controller (QLPVHC) handles the nonlinear planing force less conservatively than the sliding-mode controller (SMC). In addition, if the variation rate of the vertical velocity *w* is known, we can further reduce the design conservativeness. The sliding-mode controller (SMC) can handle the uncertainties explicitly once the bounds of the uncertainties have been estimated; further, the sliding-mode controller (SMC) can deal with large uncertainties by using the switching control signal. However, obtaining a very tight bound β on the uncertain nonlinear term can be difficult, and thus could lead to a conservative design. Generally speaking, it is a bit unfair to compare two controllers only in terms of several sets of simulation results, especially if both controllers involve tuning design parameters. Nevertheless, we still include the evaluation of both controller designs using the same set of simulations, i.e., the sliding-mode controller (SMC) in Figs. 3-5 - 3-6 and the Quasi-LPV H_∞ controller (QLPVHC) in Figs. 4-7 - 4-8 are evaluated against the same set of uncertainty samples in the Monte Carlo simulations. We offer the following observations: compared to the Quasi-LPV H_∞ controller (QLPVHC), the sliding-mode controller (SMC) achieved more precise *w*-tracking (compare Fig. 3-6 with

Fig. 4-8); however, the latter may lead to larger control inputs by explicitly taking into account uncertainties in the control design. It is interesting to see that the Quasi-LPV H_∞ controller (QLPVHC) is able to maintain satisfactory performance in the presence of parameter uncertainties that are not considered in the control design. The Quasi-LPV H_∞ controller (QLPVHC) also shows more oscillations in control surface deflections for reference tracking.

The memory effect has considerable impact on the transient performance of the initial responses for both the sliding-mode controller (SMC) and the Quasi-LPV H_∞ controller (QLPVHC), as shown in Figs. 3-2 and 4-4. This observation motivates us to design controllers directly based on the Time-Delay Benchmark Model, as we will show in Chapter 5.

Chapter 5

Delay-dependent Quasi-LPV Control for the Time-Delay Benchmark Model

5.1 Introduction

Existing control designs either neglect the memory effect of the cavity-vehicle interaction [1, 3, 6-8, 14, 15] or assume that the delay can be directly cancelled [12, 18]. As discussed in [12, 16, 17], neglecting this cavity-vehicle memory effect could substantially degrade the control performance of a supercavitating vehicle. Figs. 3-2 and 4-4 show that the memory effect has degraded the transient performance of the initial responses for both the sliding-mode controller (SMC) and the Quasi-LPV H_∞ controller (QLPVHC). Fig. 4-6 shows that the QLPVHC controller cannot track the pitch angle command well. Note that these two controllers are designed based on the Benchmark Model, which does not take into account the memory effect of the cavity-vehicle interaction. In this chapter, we will treat the supercavitating vehicle with a time-delay planing force model (as described in the Time-Delay Benchmark Model in Chapter 2) as a delay-dependent system. We will apply a Lyapunov-Krasovskii-based control technique instead of directly canceling the delay-dependent terms.

In recent years, various (robust) H_∞ control approaches have been proposed for linear (uncertain) time-delay systems. These can be categorized into two main groups: delay-independent (e.g., [33, 34]) and delay-dependent (e.g., [35-39]). The delay-

independent approaches aim to design a stabilizing control that works for any constant delay irrespective of size. The delay-dependent approaches explicitly take into account the size of the time delay in the control design and usually work out an upper bound for the time delay, so that the closed-loop system remains stable under any delay less than the upper bound. In general, delay-dependent approaches are less conservative than delay-independent ones. Analysis and control designs for time-delay Linear-Parameter-Varying (LPV) systems were also conducted in several papers, e.g., a set of delay-independent and delay-dependent stability conditions are derived in [40], analysis and state-feedback control for LPV systems with state-delay and parameter-varying time delays are given in [41, 42], and variation rate of time-delay is taken into account in deriving the stability conditions in [43]. In this dissertation, based on the Time-Delay Benchmark Model proposed in [18], we reformulate the pitch-plane dynamics of the supercavitating vehicle as a time-delay Quasi-Linear-Parameter-Varying (Quasi-LPV) system to address the delay-dependent nonlinear planing force. Since the variation rates of the scheduling variables in the Quasi-LPV supercavitating vehicle model, as well as the variation rate of the time delay are not available for design, we do not directly apply the time-delay LPV control results from the above-mentioned references [41, 42, 43]. Instead, we extend the delay-dependent (robust) H_∞ control for linear (uncertain) time-delay systems in [37, 44] to polytopic LPV systems and then apply the results to the Quasi-LPV supercavitating vehicle model. The reasons why we are interested in the results from [37, 44] lie that they propose a less conservative Lyapunov-Krasovskii functional and the bounded real lemma derived by the descriptor system approach is considered the most efficient criterion for systems with delays in existing literature.

5.2 A Time-delay Quasi-LPV Model

In this section, we reformulate the nonlinear Time-Delay Benchmark Model given in Section 2.2 into a time-delay Quasi-LPV model. We first define the function $\lambda_1(h') = (\frac{1+h'}{1+2h'})[1-(\frac{R'}{h'+R'})^2]$. By definition, h' (normalized immersion depth) is nonnegative and R' (normalized difference between cavity and body diameter) is constant once the configuration parameters of a supercavitating vehicle (e.g., L, R, R_n and σ) are determined. Also note that $\lambda_1(h')$ is a strict concave function of h'. It achieves the maximum value at $h' = 1.7942$ based on the parameter values in Appendix D. A parametric plot of λ_1 in terms of h' is given in Fig. 5-1.

We further define

$$\lambda_2 = \begin{cases} -\frac{\dot{R}_c}{V} & \textit{bottom contact} \\ 0 & \textit{inside cavity} \\ \frac{\dot{R}_c}{V} & \textit{top contact} \end{cases} \qquad 5.1$$

$$\lambda_3 = z(t) + \theta(t)L - z(t-\tau) \qquad 5.2$$

and define variables $\pi_1 = \frac{V^2}{mL}\lambda_1$, and $\pi_2 = \frac{\lambda_2}{\lambda_3}$.

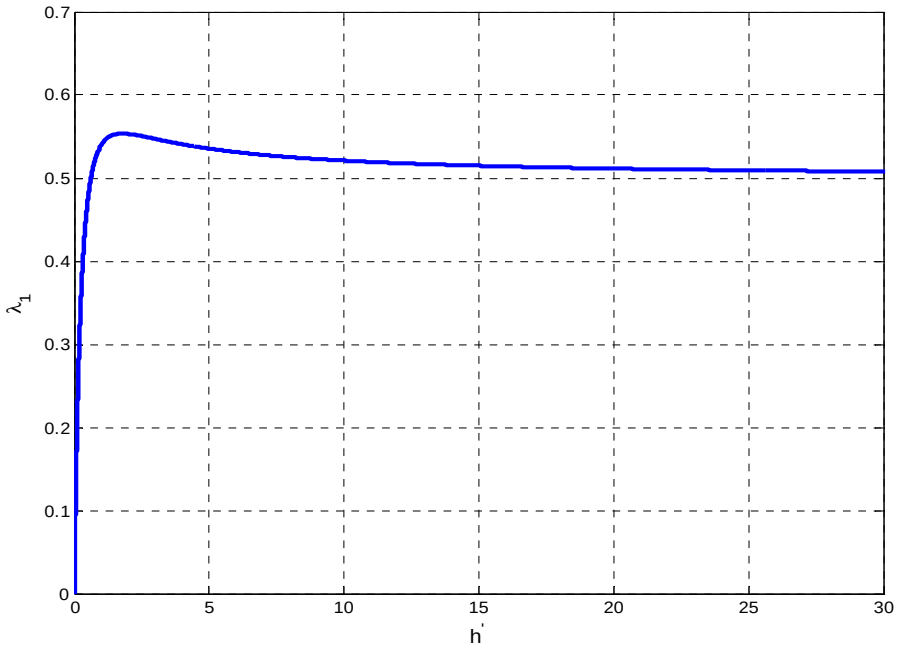

Figure 5-1: Relationship between λ_1 and h'.

If planing occurs, i.e., there is bottom contact or top contact, by the definitions of λ_1, λ_2, λ_3, π_1 and π_2, we can express the $F_{plane}^{\wedge}$ in Eq. 2.31 into the following form,

$$\begin{aligned} F_{plane}^{\wedge} &= -\frac{V^2}{mL}\left(\frac{1+h'}{1+2h'}\right)\left[1-\left(\frac{R'}{h'+R'}\right)^2\right]\alpha_{plane} \\ &= -\pi_1\alpha_{plane} \\ &= -\pi_1\left[\theta(t)-\theta(t-\tau)+\frac{w(t-\tau)}{V}+\lambda_2\right] \\ &= -\pi_1\left\{\theta(t)-\theta(t-\tau)+\frac{w(t-\tau)}{V}+\pi_2\left[z(t)+\theta(t)L-z(t-\tau)\right]\right\} \end{aligned} \qquad 5.3$$

By definition, we note that for a fixed set of vehicle parameters, $\dot{R}_c$ (contraction rate of the cavity at the planing location) is constant and particularly, $\dot{R}_c < 0$ corresponding to the cavitation number σ given in Appendix D. By Eq. 2.36, and Eqs. 5.1 - 5.3, if planing occurs, λ_2 and λ_3 always have the same sign. When they are both positive (corresponding to bottom contact), λ_2 is constant since $\dot{R}_c$ is constant, and λ_3 is lower bounded by $(R_c - R)$. When they are both negative (top contact), λ_2 is constant and $-\lambda_3$ is lower bounded by $(R_c - R)$. Hence, λ_2 / λ_3 is always positive and upper bounded. In summary, if planing occurs, we have

$$0 < \pi_2 \le -\frac{\dot{R}_c}{V(R_c - R)} \tag{5.4}$$

Also note that by the concavity of λ_1 with respect to h', π_1 is positive and upper bounded. Hence, by Eq. 5.3, F^{Λ}_{plane} is a bilinear function of π_1 and π_2, with π_1 and π_2 both positive and upper bounded. We further define $\pi_3 = \pi_1 \pi_2$. Then the time-delay model for F^{Λ}_{plane} in Eq. 5.3 can be written as,

$$F^{\wedge}_{plane} = \begin{bmatrix} -\pi_3 \\ -\pi_1 - \pi_3 L \\ 0 \\ 0 \end{bmatrix}^T \begin{bmatrix} z(t) \\ \theta(t) \\ w(t) \\ q(t) \end{bmatrix} + \begin{bmatrix} \pi_3 \\ \pi_1 \\ -\pi_1 / V \\ 0 \end{bmatrix}^T \begin{bmatrix} z(t-\tau) \\ \theta(t-\tau) \\ w(t-\tau) \\ q(t-\tau) \end{bmatrix} \tag{5.5}$$

which has affine dependence on π_1 and π_3. Corresponding to the parameter values given in Appendix D, we have $0 \le \lambda_1 \le 0.554$, $\dot{R}_c = -3.2965$, and thus $0 \le \pi_1 \le 865.625$ and $0 \le \pi_3 \le 966.73$. When the vehicle is inside the cavity, $h' = 0$ and thus $\lambda_1 = 0$. This leads to $\pi_1 = 0$, $\pi_3 = 0$ and thus $F_{plane}^{\Lambda} = 0$, so Eq. 5.5 still holds.

Note that M_I and B_I are nonsingular matrices in Eq. 2.32. Substitute Eq. 5.5 into Eq. 2.31 and define,

$$\begin{bmatrix} \delta_f \\ \delta_c \end{bmatrix} = u_0 + u_1, \; u_0 = -B_I^{-1} F_{grav}^{\Lambda} \tag{5.6}$$

then the supercavitating vehicle model can be expressed as,

$$\dot{x}(t) = Ax(t) + A_d x(t-\tau) + Bu_1 \tag{5.7}$$

with $x = \begin{bmatrix} z & \theta & w & q \end{bmatrix}^T$ and

$$A = \begin{bmatrix} 0 & -V & 1 & 0 \\ 0 & 0 & 0 & 1 \\ 0 & 0 & & \\ 0 & 0 & & M_I^{-1} A_I \end{bmatrix} + \begin{bmatrix} & & 0 & 0 \\ & & 0 & 0 \\ & & 0 & 0 \\ M_I^{-1} \begin{bmatrix} -\pi_3 & -(\pi_1 + \pi_3 L) \\ -\pi_3 L & -(\pi_1 + \pi_3 L)L \end{bmatrix} & & 0 & 0 \end{bmatrix} \tag{5.8}$$

$$A_d = \begin{bmatrix} & & & 0 & 0 & 0 & 0 \\ & & & 0 & 0 & 0 & 0 \\ M_I^{-1}\begin{bmatrix} \pi_3 & \pi_1 & -\pi_1/V \\ \pi_3 L & \pi_1 L & -\pi_1 L/V \end{bmatrix} & & & 0 \\ & & & 0 \end{bmatrix}, \quad B = \begin{bmatrix} 0 & 0 \\ 0 & 0 \\ M_I^{-1}B_I \end{bmatrix} \qquad 5.9$$

If assume that π_1 and π_3 are independent, the delay-dependent supercavitating vehicle model in Eq. 5.7 - Eq. 5.9 becomes a time-delay Quasi-LPV system that has affine dependence on the scheduling parameters π_1 and π_3. It is worth pointing out that though conservativeness could be introduced by treating π_1 and π_3 independently, it allows us to apply LPV control with affine dependence on scheduling variables to the supercavitating vehicle model (rather than resorting to bilinear dependence on scheduling variables). Additionally, we would like to point out that the derivation of the model (Eq. 5.7 - Eq. 5.9) is one of many possible ways in deriving a Quasi-LPV model from the original nonlinear system, i.e. Eq. 2.31. The advantages of this Quasi-LPV model lie that it has simple dependence on scheduling parameters, the scheduling variables are positive, and their upper bounds can be easily computed once the vehicle configuration parameters are determined.

5.3 H_∞ Control of Time-delay LPV Systems

In Section 5.3.1, a delay-dependent bounded real lemma for a class of linear time-delay systems from [37] is introduced, based on which we derive H_∞ (L_2-gain) tracking control for the linear time-delay systems and then derive the robust H_∞ tracking control for the time-delay linear uncertain systems. In Section 5.3.2, we extend the results to time-delay LPV systems with affine dependence on scheduling parameters, where we derive matrix inequalities for both nominal and robust H_∞ tracking control for the time-delay LPV systems. In Section 5.4, the extended results/theorems in Section 5.3.2 will be applied to control designs for the Quasi-LPV supercavitating vehicle model.

5.3.1 H_∞ Tracking Control of Time-delay Linear Systems

A delay-dependent bounded real lemma from [37] is given as follows:

Lemma 5.3.1 [37] Consider a class of linear state-delay systems described by,

$$\begin{aligned} \dot{x}(t) &= Ax(t) + A_d x(t-\tau) + B_w w(t) \\ o(t) &= \begin{bmatrix} Cx(t) + D_w w(t) \\ C_1 x(t-\tau) \end{bmatrix} \\ x(t) &= 0,\ t \in [-\tau, 0] \end{aligned} \tag{5.10}$$

where $x(t) \in R^n$ is the state; $w(t) \in R^m$ is the disturbance input that belongs to $L_2[0,\infty)$; $o(t) \in R^l$ is the controlled output. The time delay $\tau \le \bar{\tau}$. The matrices A, A_d, B_w, C,

D_w, and C_1 are known real constant matrices of appropriate dimensions. For a prescribed $\gamma > 0$ and $\bar{\tau} \geq 0$, assume that there exist $P_1 > 0$, P_2, P_3, Q, X_{11}, X_{12}, X_{22}, Y_1, Y_2, and $Z > 0$ such that the following Eq. 5.11 and Eq. 5.12 hold,

$$\begin{bmatrix} \Gamma_{11} & \Gamma_{12} & P_2^T A_d - Y_1 & P_2^T B_w & C^T & 0 \\ * & \Gamma_{22} & P_3^T A_d - Y_2 & P_3^T B_w & 0 & 0 \\ * & * & -Q & 0 & 0 & C_1^T \\ * & * & * & -\gamma^2 I & D_w^T & 0 \\ * & * & * & * & -I & 0 \\ * & * & * & * & * & -I \end{bmatrix} < 0 \qquad 5.11$$

$$\begin{bmatrix} X_{11} & X_{12} & Y_1 \\ * & X_{22} & Y_2 \\ * & * & Z \end{bmatrix} \geq 0 \qquad 5.12$$

where

$$\begin{aligned} \Gamma_{11} &= P_2^T A + A^T P_2 + \bar{\tau} X_{11} + Q + Y_1 + Y_1^T \\ \Gamma_{12} &= P_1 - P_2^T + A^T P_3 + \bar{\tau} X_{12} + Y_2^T \\ \Gamma_{22} &= -P_3 - P_3^T + \bar{\tau} X_{22} + \bar{\tau} Z \end{aligned} \qquad 5.13$$

and $*'s$ in Eq. 5.11 and Eq. 5.12 represent symmetric entries in a matrix. Then the system in Eq. 5.10 is stable and satisfies the H_∞ (L_2-gain) performance $\|o(t)\|_2 < \gamma \|w(t)\|_2$ for all nonzero $w(t) \in L_2[0, \infty)$ and any constant time-delay τ satisfying $0 \leq \tau \leq \bar{\tau}$.

Next we consider a tracking problem, where we consider a time-delay linear system as follows:

$$\dot{x}(t) = Ax(t) + A_d x(t-\tau) + Bu_1(t) \tag{5.14}$$

The objective is to design a state-feedback control $u_1 = K(r(t) - x(t)) \equiv Ke(t)$, where $r(t)$ denotes the reference signal and $e(t)$ denotes the tracking error signal, such that for a prescribed $\gamma > 0$ and $\bar{\tau} \geq 0$, the H_∞ (L_2-gain) performance $\|o(t)\|_2 < \gamma \|r(t)\|_2$ is satisfied corresponding to the controlled output $o(t) = \begin{bmatrix} e & u_1 \end{bmatrix}^T$, for all nonzero $r(t) \in L_2[0,\infty)$ and any constant time-delay τ satisfying $0 \leq \tau \leq \bar{\tau}$.

Insert $u_1 = K(r(t) - x(t))$ into Eq. 5.14, and then we have

$$\begin{aligned} \dot{x}(t) &= Ax(t) + A_d x(t-\tau) + BK(r - x) \\ &= (A - BK)x(t) + A_d x(t-\tau) + BKr(t) \end{aligned} \tag{5.15}$$

Also, the controlled output variable $o(t)$ becomes

$$\begin{aligned} o(t) &= \begin{bmatrix} e \\ u_1 \end{bmatrix} = \begin{bmatrix} r - x \\ K(r - x) \end{bmatrix} = \begin{bmatrix} I \\ K \end{bmatrix} (r - x) \\ &= -\begin{bmatrix} I \\ K \end{bmatrix} x + \begin{bmatrix} I \\ K \end{bmatrix} r \end{aligned} \tag{5.16}$$

where I denotes the identity matrix of appropriate dimension. By applying Lemma 5.3.1 to the system in Eq. 5.15 and Eq. 5.16, we have the following theorem.

Theorem 5.3.1 Consider a class of linear time-delay systems described by,

$$\dot{x}(t) = Ax(t) + A_d x(t-\tau) + Bu_1(t) \tag{5.17}$$

Define a tracking controller $u_1 = K(r(t) - x(t)) \equiv Ke(t)$, where $r(t)$ represents the reference signal. For a prescribed $\gamma > 0$ and $\bar{\tau} \geq 0$, assume that there exist $L_1 > 0$, L_2, L_3, W, M_{11}, M_{12}, M_{22}, N_1, N_2, $S > 0$ and U that satisfy the inequalities in Eq. 5.18 and Eq. 5.19. Then for the controlled output $o(t)$ defined in Eq. 5.17 and $K = UL_1^{-1}$, the closed-loop system is stable and satisfies the H_∞ performance $\|o(t)\|_2 < \gamma \|r(t)\|_2$ for all nonzero $r(t) \in L_2[0,\infty)$ and any constant time-delay τ satisfying $0 \leq \tau \leq \bar{\tau}$.

$$\begin{bmatrix} \Gamma_{11} & \Gamma_{12} & -N_1 & 0 & -L_1 & -U^T & \bar{\tau} L_2^T \\ * & \Gamma_{22} & A_d L_1 - N_2 & BU & 0 & 0 & \bar{\tau} L_3^T \\ * & * & -W & 0 & 0 & 0 & 0 \\ * & * & * & -\gamma^2 L_1^2 & L_1 & U^T & 0 \\ * & * & * & * & -I & 0 & 0 \\ * & * & * & * & * & -I & 0 \\ * & * & * & * & * & * & -\bar{\tau} S \end{bmatrix} < 0 \tag{5.18}$$

$$\begin{bmatrix} M_{11} & M_{12} & N_1 \\ * & M_{22} & N_2 \\ * & * & L_1 S^{-1} L_1 \end{bmatrix} \geq 0 \qquad 5.19$$

with a bit abuse of notations on Γ_{11}, Γ_{12}, and Γ_{22},

$$\begin{aligned} \Gamma_{11} &= L_2 + L_2^T + W + N_1 + N_1^T + \bar{\tau} M_{11} \\ \Gamma_{12} &= (AL_1 - BU)^T - L_2^T + L_3 + N_2^T + \bar{\tau} M_{12} \\ \Gamma_{22} &= -L_3 - L_3^T + \bar{\tau} M_{22} \end{aligned} \qquad 5.20$$

and $*'s$ representing symmetric entries in a matrix.

The proof is given in Appendix A, and part of the proof follows a similar line as the proof of Theorem 5.3.1 in [37]. Note that the conditions in Eq. 5.18 and Eq. 5.19 are not Linear Matrix Inequalities (LMI) conditions due to the terms L_1^2 and $L_1 S^{-1} L_1$. We apply a cone complementarity linearization algorithm, which has been used in multiple papers (e.g., [45, 37]), to handle these two terms. Details of the algorithm are given in Appendix B.

Next Theorem 5.3.1 is extended to robust H_∞ tracking for time-delay linear uncertain systems in the following theorem.

Theorem 5.3.2 Consider a class of time-delay linear uncertain systems described by,

$$\dot{x}(t) = [A + \Delta A]x(t) + [A_d + \Delta A_d]x(t-\tau) + [B + \Delta B]u_1(t) \qquad 5.21$$

where notations are defined in the same way as in Theorem 5.3.1. Assume that uncertainties in A, A_d and B, which are denoted by ΔA, ΔA_d and ΔB, respectively, are time-varying matrices given in the following form,

$$\begin{bmatrix} \Delta A & \Delta A_d & \Delta B \end{bmatrix} = F\bar{\Delta}(t)\begin{bmatrix} E & E_d & E_b \end{bmatrix} \qquad 5.22$$

where F, E, E_d and E_b are constant matrices. The matrix $\bar{\Delta}(t)$ denotes time-varying uncertainty and it is assumed to be in a diagonal form, i.e., $\bar{\Delta}(t) = diag\{\bar{\Delta}_1(t), \cdots, \bar{\Delta}_\nu(t)\}$, with $\bar{\Delta}_i(t) \in R^{p_i \times q_i}$, $i = 1, \cdots, \nu$, satisfying $\bar{\Delta}_i^T(t)\bar{\Delta}_i(t) \le I$, $\forall t \ge 0$. Define a state-feedback tracking controller $u_1(t) = K(r(t) - x(t))$, where $r(t)$ represents the reference signal. For a prescribed $\gamma > 0$ and $\bar{\tau} \ge 0$, assume that there exist $L_1 > 0$, L_2, L_3, W, M_{11}, M_{12}, M_{22}, N_1, N_2, $S > 0$, U and $\Lambda = diag\{\lambda_1 I, \cdots, \lambda_\nu I\} > 0$ that satisfy the inequalities in Eq. 5.19 and Eq. 5.23. Then for the controlled output $o(t)$ defined in Eq. 5.16 and controller $u_1 = K(r(t) - x(t))$ with $K = UL_1^{-1}$, the closed-loop system is stable and

satisfies the H_∞ performance $\|o(t)\|_2 < \gamma \|r(t)\|_2$ for all nonzero $r(t) \in L_2[0,\infty)$ and any constant time-delay τ satisfying $0 \le \tau \le \bar{\tau}$.

$$\begin{bmatrix} \Omega_{11} & \Omega_{12} & -N_1 & 0 & -L_1 & -U^T & \bar{\tau}L_2^T & (EL_1 - E_bU)^T \\ * & \Omega_{22} & A_dL_1 - N_2 & BU & 0 & 0 & \bar{\tau}L_3^T & 0 \\ * & * & -W & 0 & 0 & 0 & 0 & L_1^T E_d^T \\ * & * & * & -\gamma^2 L_1^2 & L_1 & U^T & 0 & U^T E_b^T \\ * & * & * & * & -I & 0 & 0 & 0 \\ * & * & * & * & * & -I & 0 & 0 \\ * & * & * & * & * & * & -\bar{\tau}S & 0 \\ * & * & * & * & * & * & * & -\Lambda \end{bmatrix} < 0 \qquad 5.23$$

with

$$\begin{aligned} \Omega_{11} &= L_2 + L_2^T + W + N_1 + N_1^T + \bar{\tau}M_{11} \\ \Omega_{12} &= (AL_1 - BU)^T - L_2^T + L_3 + N_2^T + \bar{\tau}M_{12} \\ \Omega_{22} &= -L_3 - L_3^T + \bar{\tau}M_{22} + F\Lambda F^T \end{aligned} \qquad 5.24$$

The proof of Theorem 5.3.2 is given in Appendix A. Part of the proof follows a similar line as the proof of Theorem 5.1 in [37].

5.3.2 H_∞ Tracking Control of Time-delay Linear-Parameter-Varying Systems

In this section, we extend the results in Section 5.3.1 to state-feedback control of time-delay Linear-Parameter-Varying systems with affine dependence on scheduling variables.

Lemma 5.3.2 Consider a class of state-delay Linear-Parameter-Varying systems described by,

$$\begin{aligned} \dot{x}(t) &= A(\psi)x(t) + A_d(\psi)x(t-\tau) + B_w(\psi)w(t) \\ o(t) &= \begin{bmatrix} Cx(t) + D_w w(t) \\ C_1 x(t-\tau) \end{bmatrix} \\ x(t) &= 0,\ t \in [-\tau, 0] \end{aligned} \tag{5.25}$$

With a bit abuse of notation, we assume that $A(\psi)$, $A_d(\psi)$ and $B_w(\psi)$ have affine dependence on a time-varying scheduling parameter vector ψ that varies in a polytope of vertices $\mu_1, \mu_2, ..., \mu_r$, i.e.

$$\begin{pmatrix} A(\psi) \\ A_d(\psi) \\ B_w(\psi) \end{pmatrix} = \left\{ \sum_{i=1}^{r} \eta_i \begin{pmatrix} A(\mu_i) \\ A_d(\mu_i) \\ B_w(\mu_i) \end{pmatrix} : \eta_i \geq 0, \sum_{i=1}^{r} \eta_i = 1 \right\} \tag{5.26}$$

For a prescribed $\gamma > 0$ and $\bar{\tau} \geq 0$, assume that there exist common $P_1 > 0$, P_2, P_3, Q, X_{11}, X_{12}, X_{22}, Y_1, Y_2, and $Z > 0$ that satisfy the inequalities in Eq. 5.11 - Eq. 5.13

with $A \to A(\mu_i)$, $A_d \to A_d(\mu_i)$, and $B_w \to B_w(\mu_i)$ for each μ_i, $i = 1, \cdots, r$. Then the system in Eq. 5.25 is stable and satisfies the quadratic performance $\|o(t)\|_2 < \gamma \|w(t)\|_2$ for all nonzero $w(t) \in L_2[0, \infty)$ and any constant time-delay τ satisfying $0 \le \tau \le \bar{\tau}$.

Proof of Lemma 5.3.2 is given in the Appendix A.

By Lemma 5.3.2, we extend the H_∞ tracking control results in Theorem 5.3.1 and Theorem 5.3.2 to LPV systems as follows,

Theorem 5.3.3 Consider a class of time-delay Linear-Parameter-Varying systems described by,

$$\dot{x}(t) = A(\psi)x(t) + A_d(\psi)x(t-\tau) + Bu_1(t) \qquad 5.27$$

where $A(\psi)$ and $A_d(\psi)$, which depend on a time-varying scheduling parameter vector ψ, satisfy Eq. 5.26. The matrix B is constant. Assume that $(A(\psi), B)$ is quadratically stabilizable. Define a state-feedback tracking controller $u_1(t) = K(r(t) - x(t))$, where $r(t)$ represents the reference signal. For a prescribed $\gamma > 0$ and $\bar{\tau} \ge 0$, assume that there exist U_i, $i = 1, ..., r$, and common $L_1 > 0$, L_2, L_3, W, M_{11}, M_{12}, M_{22}, N_1, N_2 and $S > 0$ that satisfy the inequalities in Eq. 5.19 and Eq. 5.28 for each μ_i, $i = 1, ..., r$. Then for the controlled output $o(t)$ defined in Eq. 5.16 and state-feedback controller $u_1(t) = K(r(t) - x(t))$ with $K = \sum_{i=1}^{r} \eta_i K^i$ and $K^i = U_i L_1^{-1}$, where η_i's are defined in Eq. 5.26, the

closed-loop system is stable and satisfies the H_∞ performance $\|o(t)\|_2 < \gamma \|r(t)\|_2$ for all nonzero $r(t) \in L_2[0,\infty)$ and any constant time-delay τ satisfying $0 \le \tau \le \bar{\tau}$.

$$\begin{bmatrix} \Gamma_{11} & \Gamma_{12}^i & -N_1 & 0 & -L_1 & -U_i^T & \bar{\tau} L_2^T \\ * & \Gamma_{22} & A_d(\mu_i)L_1 - N_2 & BU_i & 0 & 0 & \bar{\tau} L_3^T \\ * & * & -W & 0 & 0 & 0 & 0 \\ * & * & * & -\gamma^2 L_1^2 & L_1 & U_i^T & 0 \\ * & * & * & * & -I & 0 & 0 \\ * & * & * & * & * & -I & 0 \\ * & * & * & * & * & * & -\bar{\tau} S \end{bmatrix} < 0, \; i = 1,2,...r \qquad 5.28$$

with

$$\begin{aligned} \Gamma_{11} &= L_2 + L_2^T + W + N_1 + N_1^T + \bar{\tau} M_{11} \\ \Gamma_{12}^i &= (A(\mu_i)L_1 - BU_i)^T - L_2^T + L_3 + N_2^T + \bar{\tau} M_{12} \\ \Gamma_{22} &= -L_3 - L_3^T + \bar{\tau} M_{22} \end{aligned} \qquad 5.29$$

Proof: The proof is straightforward by applying Lemma 5.3.2, Theorem 5.3.1 and its proof.

Theorem 5.3.4 Consider a class of time-delay Linear-Parameter-Varying uncertain systems described by,

$$\dot{x}(t) = [A(\psi) + \Delta A]x(t) + [A_d(\psi) + \Delta A_d]x(t-\tau) + [B + \Delta B]u_1(t) \qquad 5.30$$

where notations are defined in the same way as in Theorem 5.3.3. Assume that ΔA, ΔA_d and ΔB are time-varying uncertainties in $A(\psi)$, $A_d(\psi)$ and B, respectively, and they are given in the following form,

$$\begin{bmatrix} \Delta A & \Delta A_d & \Delta B \end{bmatrix} = F\bar{\Delta}(t)\begin{bmatrix} E & E_d & E_b \end{bmatrix} \tag{5.31}$$

where F, E, E_d and E_b are constant matrices. $\bar{\Delta}(t)$ denotes time-varying uncertainty and it is assumed to be in a diagonal form, i.e., $\bar{\Delta}(t) = diag\{\bar{\Delta}_1(t), \cdots, \bar{\Delta}_\nu(t)\}$, with $\bar{\Delta}_i(t) \in R^{p_i \times q_i}$, $i = 1, \cdots, \nu$, satisfying $\bar{\Delta}_i^T(t)\bar{\Delta}_i(t) \le I$, $\forall t \ge 0$, and I denotes the identity matrix of appropriate dimension. Define a state-feedback tracking controller $u_1(t) = K(r(t) - x(t))$, where $r(t)$ represents the reference signal. For a prescribed $\gamma > 0$ and $\bar{\tau} \ge 0$, assume that there exist U_i, $i = 1, ..., r$, and common $L_1 > 0$, L_2, L_3, W, M_{11}, M_{12}, M_{22}, N_1, N_2 and $S > 0$ that satisfy the inequalities in Eq. 5.19 and Eq. 5.32, for each μ_i, $i = 1, ..., r$. Then for the controlled output $o(t)$ defined in Eq. 5.16 and $K = \sum_{i=1}^{r} \eta_i K^i$ with $K^i = U_i L_1^{-1}$, where η_i's are defined in Eq. 5.26, the closed-loop system is stable and satisfies the H_∞ performance $\|o(t)\|_2 < \gamma \|r(t)\|_2$ for all nonzero $r(t) \in L_2[0, \infty)$ and any constant time-delay τ satisfying $0 \le \tau \le \bar{\tau}$.

$$\begin{bmatrix} \Omega_{11} & \Omega_{12}^{i} & -N_1 & 0 & -L_1 & -U_i^T & \overline{\tau} L_2^T & (EL_1 - E_b U_i)^T \\ * & \Omega_{22} & A_d(\mu_i)L_1 - N_2 & BU_i & 0 & 0 & \overline{\tau} L_3^T & 0 \\ * & * & -W & 0 & 0 & 0 & 0 & L_1^T E_d^T \\ * & * & * & -\gamma^2 L_1^2 & L_1 & U_i^T & 0 & U_i^T E_b^T \\ * & * & * & * & -I & 0 & 0 & 0 \\ * & * & * & * & * & -I & 0 & 0 \\ * & * & * & * & * & * & -\overline{\tau} S & 0 \\ * & * & * & * & * & * & * & -\Lambda \end{bmatrix} < 0, \qquad 5.32$$

$i = 1, 2, \ldots r$

with

$$\begin{aligned} \Omega_{11} &= L_2 + L_2^T + W + N_1 + N_1^T + \overline{\tau} M_{11} \\ \Omega_{12}^{i} &= (A(\mu_i)L_1 - BU_i)^T - L_2^T + L_3 + N_2^T + \overline{\tau} M_{12} \\ \Omega_{22} &= -L_3 - L_3^T + \overline{\tau} M_{22} + F \Lambda F^T \end{aligned} \qquad 5.33$$

The proof is straightforward by applying Lemma 5.3.2 and Theorem 5.3.2.

5.4 Delay-dependent Controller Design for the Supercavitating Vehicle

In this section, we apply the nominal and robust LPV control from Section 5.3.2 to the delay-dependent model of the supercavitating vehicle. Fig. 5-2 shows the controller structure, where G represents the delay-dependent supercavitating vehicle model, which has control input $u(t)$ and state variable $x(t)$. The reference signal is denoted by $r(t)$ and the error signal between the reference and the state is denoted by $e(t)$. We define $e = r - x = \begin{bmatrix} z_r - z & \theta_r - \theta & w_r - w & q_r - q \end{bmatrix}^T$. The control input $u(t)$ consists of two parts:

the feed-forward u_0 is defined in Eq. 5.6 to cancel out the gravity term F_{grav}^{Λ}, and a state-feedback $u_1(t)$ is defined as $u_1(t) = K(r(t) - x(t))$. We assume that all state variables are measurable and available for feedback control.

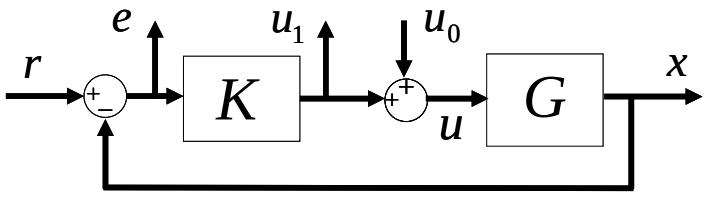

Figure 5-2: Block diagram of the feedback control.

Considering the open-loop supercavitating model in Eq. 5.7 and $u_1(t) = K(r(t) - x(t))$, the closed-loop system is expressed as,

$$\begin{aligned} \dot{x}(t) &= Ax(t) + A_d x(t-\tau) + Bu_1 \\ &= Ax(t) + A_d x(t-\tau) + BK(r - x) \\ &= (A - BK)x(t) + A_d x(t-\tau) + BKr \end{aligned} \qquad 5.34$$

which takes the same form as Eq. 5.15. The matrices A and A_d are affinely dependent on the scheduling parameters π_1 and π_3 as shown in Eqs. 5.8 - 5.9. We are interested in optimizing the H_∞ (L_2-gain) performance from the reference signal r to $\begin{bmatrix} e & u_1 \end{bmatrix}^T$. Hence we define the control output as,

$$o(t) = \begin{bmatrix} e \\ u_1 \end{bmatrix} = \begin{bmatrix} r - x \\ K(r - x) \end{bmatrix} = \begin{bmatrix} I_{4\times4} \\ K \end{bmatrix} (r - x) = -\begin{bmatrix} I_{4\times4} \\ K \end{bmatrix} x + \begin{bmatrix} I_{4\times4} \\ K \end{bmatrix} r \qquad 5.35$$

where $I_{4\times4}$ represents a 4×4 Identity matrix.

First we design a nominal H_∞ controller based on Theorem 5.3.3 in Section 5.3.2. In terms of system parameters given in Appendix D, the time delay $\tau = L/V$ in the supercavitating vehicle model (i.e., Eqs. 2.34 - 2.35) is calculated as $\tau = L/V = 0.024s$. Recall from Section 5.2 that the two scheduling parameters satisfy $0 \le \pi_1 \le 865.625$ and $0 \le \pi_3 \le 966.73$ corresponding to the vehicle configuration parameters given in Appendix D. Hence the four vertices of $\psi = [\pi_1, \pi_2]$ for the polytopic LPV system are,

$$\begin{aligned} &\mu_1 = [0 \quad 0], \mu_2 = [0 \quad 966.73] \\ &\mu_3 = [865.625 \quad 0], \mu_4 = [865.625 \quad 966.73] \end{aligned} \qquad 5.36$$

By solving the inequalities in Eq. 5.19 and Eq. 5.28, we obtain the control

$$u_1 = K(r - x) = \sum_{i=1}^{4} \eta_i K^i e \qquad 5.37$$

where

$$
\begin{aligned}
K^1 &= \begin{bmatrix} 8.7409 & -142.1955 & 1.9579 & -5.7514 \\ -0.1693 & 4.1872 & 0.1655 & 0.2560 \end{bmatrix} \\
K^2 &= \begin{bmatrix} 8.4917 & -137.1596 & 1.8597 & -5.5441 \\ -0.1746 & 4.3034 & 0.1630 & 0.2608 \end{bmatrix} \\
K^3 &= \begin{bmatrix} 8.4389 & -137.4669 & 1.9523 & -5.6055 \\ -0.1776 & 4.3183 & 0.1654 & 0.2599 \end{bmatrix} \\
K^4 &= \begin{bmatrix} 8.7868 & -142.0866 & 1.9872 & -5.7900 \\ -0.1649 & 4.1428 & 0.1670 & 0.2529 \end{bmatrix}
\end{aligned}
\tag{5.38}
$$

and the parameters η_i can be calculated as,

$$
\begin{aligned}
&\eta_1 = (1-\beta_1)(1-\beta_2),\ \eta_2 = (1-\beta_1)\beta_2 \\
&\eta_3 = \beta_1(1-\beta_2),\ \eta_4 = \beta_1\beta_2
\end{aligned}
\tag{5.39}
$$

with β_1 and β_2 defined as follows,

$$
\beta_1 = \frac{\pi_1}{865.625},\ \beta_2 = \frac{\pi_3}{966.73} \tag{5.40}
$$

Next we consider robust control of the delay-dependent LPV model of the supercavitating vehicle. As discussed in Chapter 4, we consider $\frac{C_x}{m}$ and n to be the uncertain parameters used in robust control, which essentially cover variations in control effective coefficients and variation in density ratio of the vehicle and fluid/water.

Based on the parameter values given in Appendix D, the norm of the nominal state matrix and input matrix can be calculated as $\|A_0\|_2 = 80.2$ and $\|B_0\|_2 = 1245.3$. In terms of Eq. 5.8 and Eq. 5.9, corresponding to $\pm 3\%$ variation in system parameters $\frac{C_x}{m}$ and n, the bounds of the uncertain state matrix, delayed-state matrix and input matrix are estimated as $\|\Delta A\|_2 \le 0.5414$, $\|\Delta A_d\|_2 = 0$ (since A_d does not depend on $\frac{C_x}{m}$ and n) and $\|\Delta B\|_2 \le 42.0347$. Then, the matrices F, E, E_d and E_b in Theorem 5.3.4 are defined as follows,

$$F = \begin{bmatrix} 0.5414 I_{4\times 4} & 0_{4\times 4} & 42.0347 \begin{bmatrix} 0_{2\times 2} \\ I_{2\times 2} \end{bmatrix} \end{bmatrix}$$

$$E = \begin{bmatrix} I_{4\times 4} & 0_{4\times 6} \end{bmatrix}^T,\ E_d = 0_{10\times 4},\ E_{b=} \begin{bmatrix} 0_{2\times 8} & I_{2\times 2} \end{bmatrix}^T \qquad 5.41$$

where I and 0 denote identity and zero matrices. We consider the bound of time delay $\bar{\tau}$ to be 20% longer than the nominal time delay given by $\tau = L/V$, i.e., $\bar{\tau} = 1.2\tau$. By solving inequalities in Eq. 5.19 and Eq. 5.32 corresponding to the vertex set of the scheduling variables in Eq. 5.36, we obtain the control $u_1 = K(r - x) = \sum_{i=1}^{4} \eta_i K^i e$, where η_i's are given in Eq. 5.39 and

$$
\begin{aligned}
K^1 &= \begin{bmatrix} 6.9060 & -144.4529 & -9.3538 & -14.9482 \\ 3.1731 & -51.8946 & 2.7338 & 2.1856 \end{bmatrix} \\
K^2 &= \begin{bmatrix} 7.0430 & -142.9997 & -9.2826 & -14.8419 \\ 3.1777 & -51.7201 & 2.7438 & 2.2010 \end{bmatrix} \\
K^3 &= \begin{bmatrix} 6.6390 & -139.9265 & -9.3150 & -14.9303 \\ 3.1429 & -51.3341 & 2.7542 & 2.2154 \end{bmatrix} \\
K^4 &= \begin{bmatrix} 6.8489 & -139.9523 & -9.3447 & -14.9844 \\ 3.1520 & -51.2568 & 2.7577 & 2.2206 \end{bmatrix}
\end{aligned}
\qquad 5.42
$$

Higher percentage values of variations in system parameters $\frac{C_x}{m}$ and n have also been examined, but no feasible solutions could be found for the inequalities in Eq. 5.19 and Eq. 5.32 to guarantee robust stability. This implies the conservativeness of the results in Theorem 5.3.4, particularly when it is applied to the parametric uncertainty problem as we consider here (uncertain parameters $\frac{C_x}{m}$ and n). Nevertheless, simulation results in next section show that the resulting controller can tolerate a much higher percentage of variation in uncertain parameters than guaranteed by Theorem 5.3.4.

5.5 Simulation Results

In this section, we present simulation results for the two QLPV controllers designed in this chapter. For the rest of the chapter, we refer them as the Delay-dependent Nominal LPV-H_∞ Controller (DNHC) and the Delay-dependent Robust LPV-H_∞ Controller (DRHC), respectively. Further we will compare the two controllers with

the Quasi-LPV H_∞ controller (QLPVHC) designed in Chapter 4. In order to offer results that are comparable with those presented in [1] and [4], initial responses are simulated. Additional tracking responses are also simulated to further evaluate controllers' performance. Robustness to variations in $\frac{C_x}{m}$ and n are also evaluated.

In terms of the system parameter values given in Appendix D, the time delay $\tau = L/V = 0.024s$ is used in the simulation. An actuator model with transfer function of $300/(s+300)$, subject to an amplitude limit of 25 degree and a rate limit of 100 rad/s [18], is used for both cavitator and fin control. Different actuator models can be applied for the cavitator and fins if they are needed. In all simulations, planing force memory effect from the Time-Delay Benchmark Model is included, and if one of the control actuators (either the cavitator or the fin but not both) exceeds its amplitude limit, the actuator amplitude compensation designed in Chapter 3 is applied to re-distribute the control effort between the cavitator and the fins.

5.5.1 Simulation Results without the High-gain Observer

A. Nominal performance

In this subsection, we evaluate the nominal performance of the Delay-dependent Nominal LPV- H_∞ Controller (DNHC) and the Delay-dependent Robust LPV- H_∞ Controller (DRHC) via initial responses and tracking responses (z and w tracking), In the initial response simulation, initial conditions are chosen as $z = 0$, $\theta = 0$, $w = 3\,m/s$,

and $q = 0.2\ rad/s$. Then a unit z-step input tracking and w tracking are simulated to further evaluate the controller performance, and the w-tracking reference signal is

$$w_r = 2\sin(2\pi t),\ z_r = 0,\ \theta_r = \frac{w}{V},\ \text{and}\ q_r = \dot{\theta}_r \qquad 5.43$$

Fig. 5-3 shows initial responses of the DNHC and the DRHC controllers. Their corresponding planing force time histories are also given in Fig. 5-3. We can see that the DNHC and DRHC controllers have much better transient performance than the Quasi-LPV H_∞ controller (QLPVHC) designed in Chapter 4 (compare Fig. 5-3 with Fig. 4-4), i.e., faster convergence speed and smaller transient deviations from the origin. It is noted that the assumed actuator rate limit is touched in the two responses shown in Fig. 5-3.

Fig. 5-4 shows simulation results corresponding to a unit z-step input tracking response with zero initial conditions and $\theta_r = w_r = q_r = 0$. Both the DNHC and the DRHC controllers can track the step input signal satisfactorily, though the z-step responses do not have overshoot. Note that neither the DRHC nor the QLPVHC controller induces planing force in the unit z-step input tracking response. Fig. 5-5 shows the w tracking responses, where the reference signals are given in Eq. 5.43. The closed-loop system implemented with either the DNHC or the DRHC controller achieves better performance in terms of smaller tracking errors than the one for the QLPVHC controller (compare Fig. 5-5 with Fig. 4-6).

In summary, nominal performance illustrates that either the DNHC or the DRHC controller has achieved better initial and tracking performance than the QLPVHC controller since the former two controllers are designed based on the Time-Delay Benchmark Model, which explicitly takes time-delay into account.

B. Robustness Evaluation

In this subsection, we evaluate the robustness of the DNHC and the DRHC controller with respect to parameter uncertainties using the unit z-step tracking and w tracking simulations. The reference trajectory used in the w tracking responses is given in Eq. 5.43. In all tracking responses shown in this subsection, + 20% variation (i.e., 4.8 ms variation) in the time delay τ (with nominal value $\tau = L/V = 0.024s$) is used. One hundred Monte Carlo simulations are conducted for each tracking response to evaluate the robustness of the control system with respect to variations in the parameters $\frac{C_x}{m}$ and n. In the Monte Carlo simulations of the unit z-step tracking responses as shown in Figs. 5-6 - 5-7, a set of random samples of $\frac{C_x}{m}$ and n is generated using normal distributions with zero mean and 0.4 std, being truncated within $\pm 40\%$ of the nominal values of $\frac{C_x}{m}$ and n, respectively. Figs. 5-6 - 5-7 show the stochastic envelopes (maximum, mean and minimum) of the 100 Monte Carlo simulations corresponding to the DRHC and the DRHC controller, respectively. To further compare the robustness of the closed-loop systems implemented with the two controllers, another set of random

samples of $\frac{C_x}{m}$ and n is used for w tracking simulations. The new set is generated using normal distributions with zero mean and 0.5 std, being truncated within $\pm 50\%$ of the nominal values of $\frac{C_x}{m}$ and n, respectively. Fig. 5-9 shows the stochastic envelopes corresponding to the w tracking response corresponding to the DRHC controller. We can see that the DRHC controller is able to achieve satisfactory tracking performance in the presence of uncertainty, even though the design is derived with the guarantee of robustness to $\pm 3\%$ variations of $\frac{C_x}{m}$ and n. Same w tracking simulations are also conducted for the DNHC controller and the resulting stochastic envelopes of Monte Carlo simulations are shown in Fig. 5-8. It is noted that the DNHC controller has much worse w-tracking performance than the DRHC controller with the same parameter uncertainty.

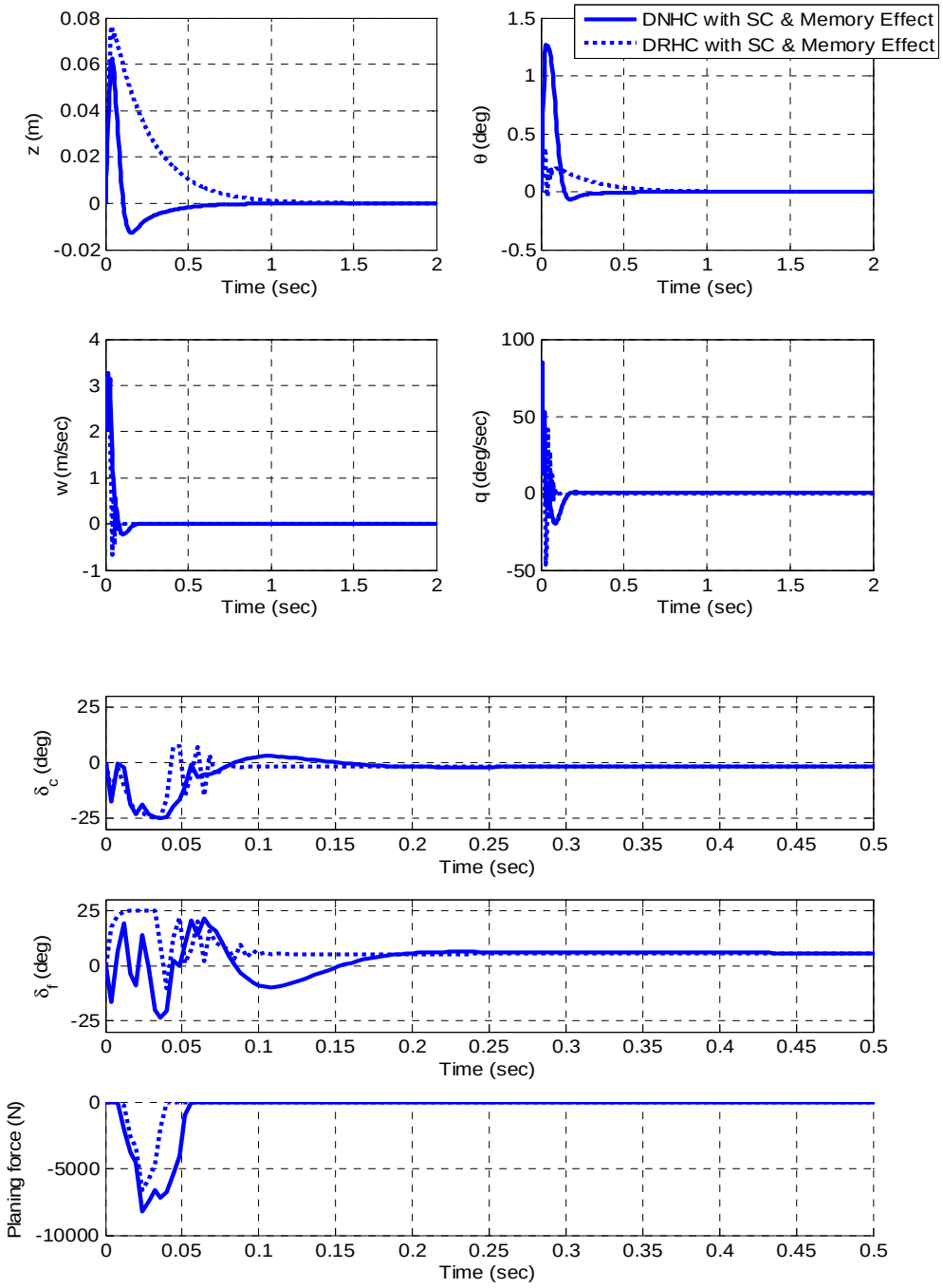

Figure 5-3: Initial response simulations for the nominal system implemented with the Delay-dependent Nominal LPV- H_∞ Controller (DNHC) and the Delay-dependent Robust LPV- H_∞ Controller (DRHC), respectively.

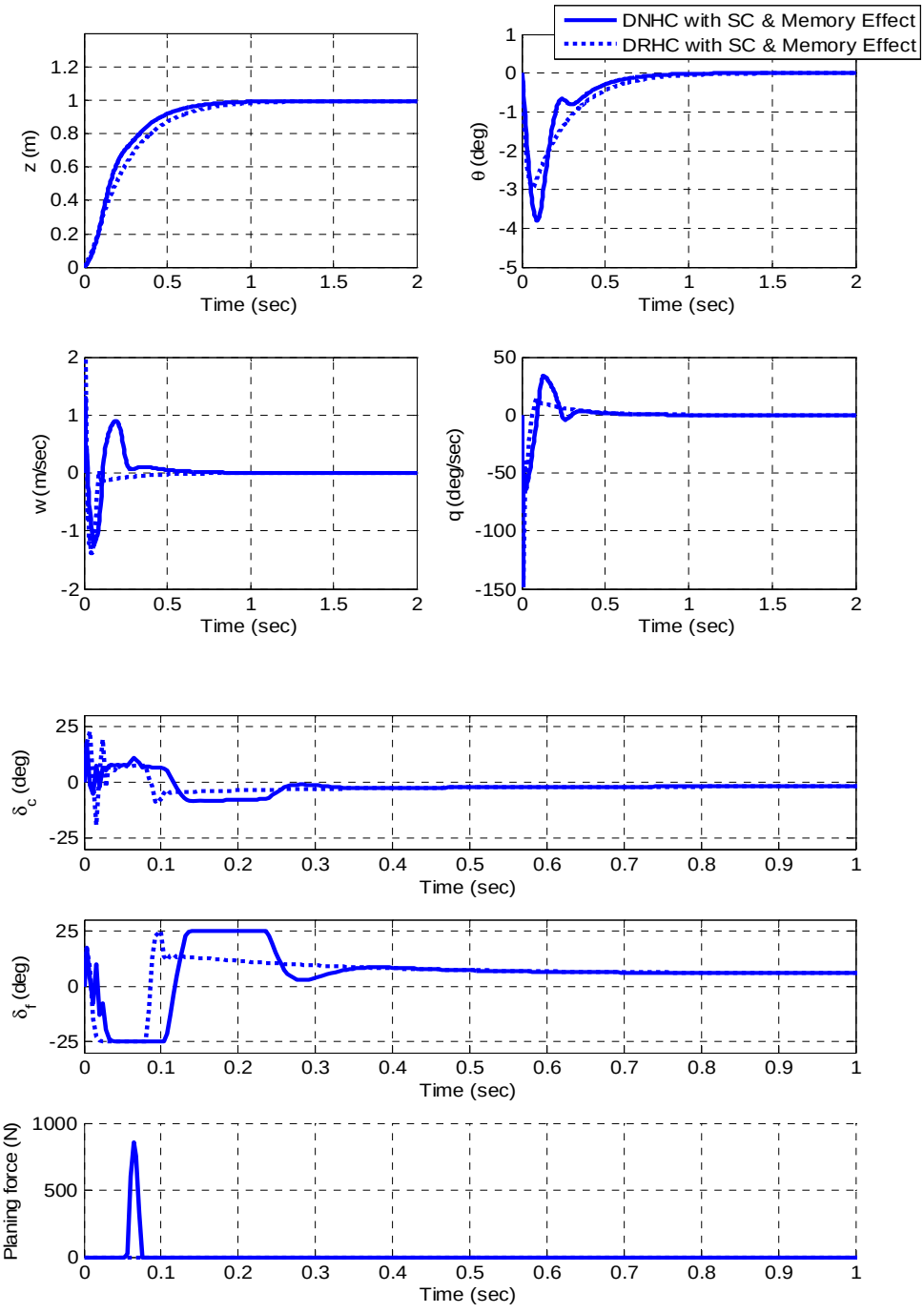

Figure 5-4: z-step responses for the nominal system implemented with the Delay-dependent Nominal LPV-H_∞ Controller (DNHC) and the Delay-dependent Robust LPV-H_∞ Controller (DRHC), respectively.

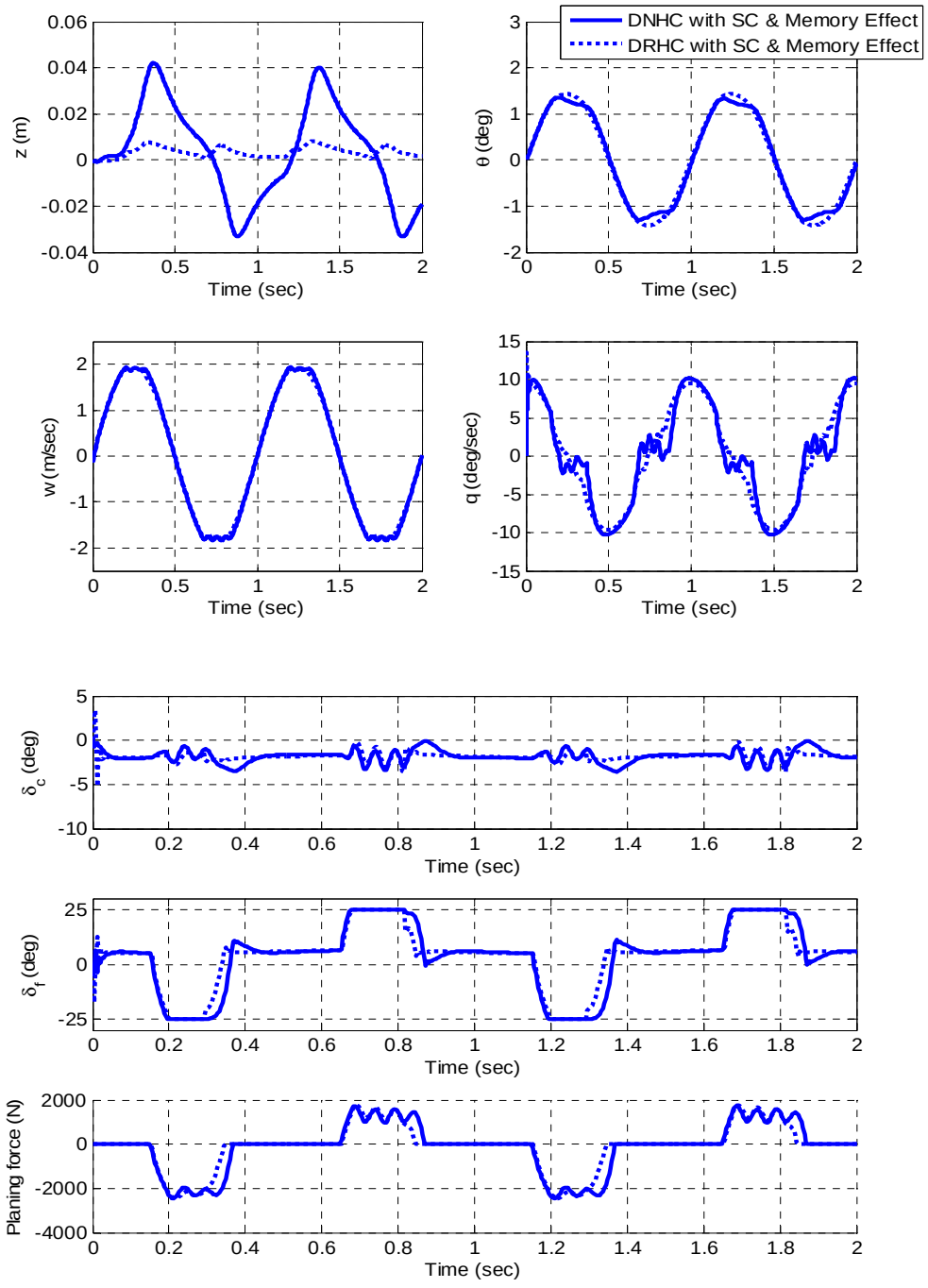

Figure 5-5: w-tracking responses for the nominal system implemented with the Delay-dependent Nominal LPV-H_∞ Controller (DNHC) and the Delay-dependent Robust LPV-H_∞ Controller (DRHC), respectively.

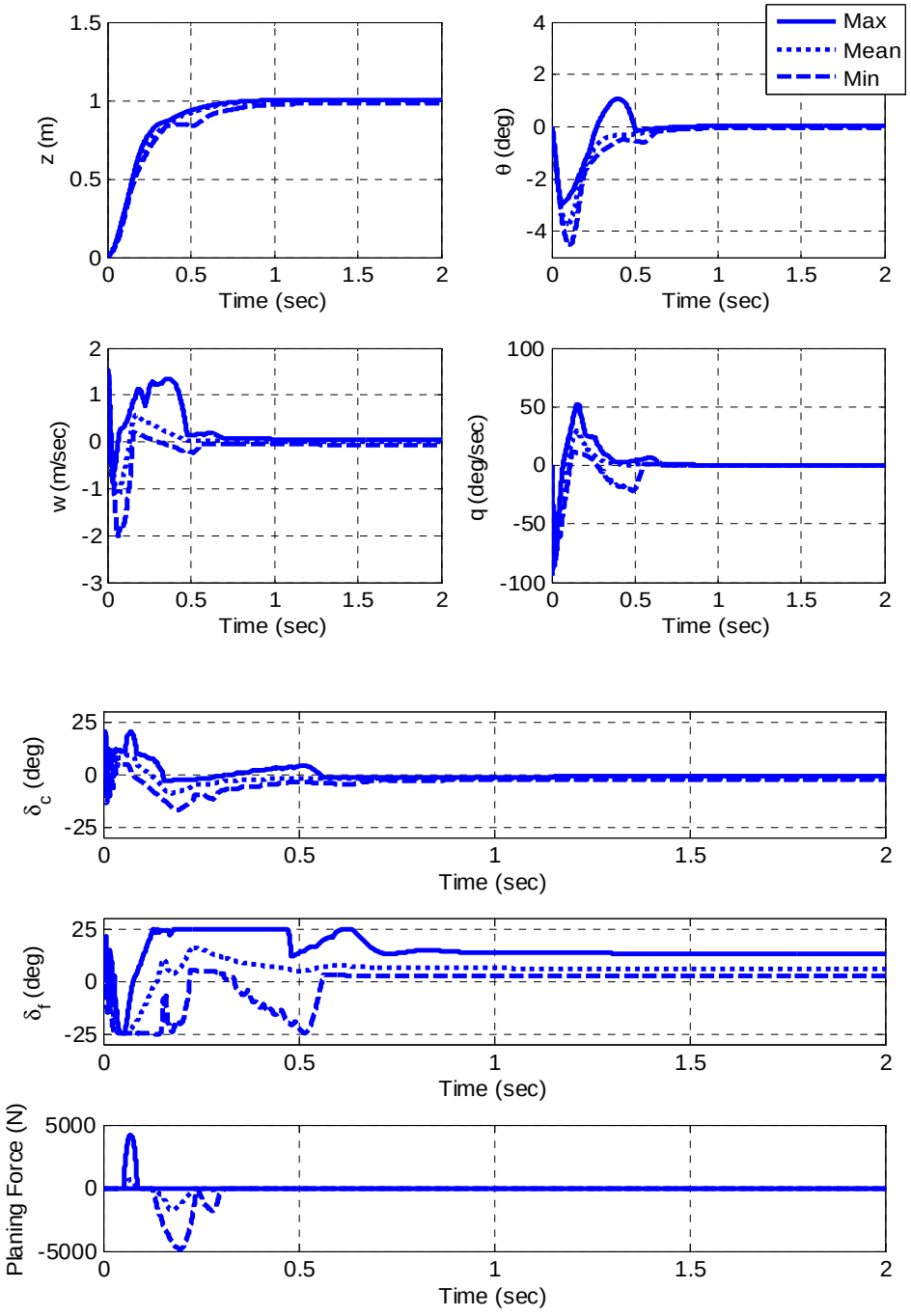

Figure 5-6: Stochastic envelopes of z-step tracking responses, with the Delay-dependent Nominal LPV-H_∞ Controller (DNHC).

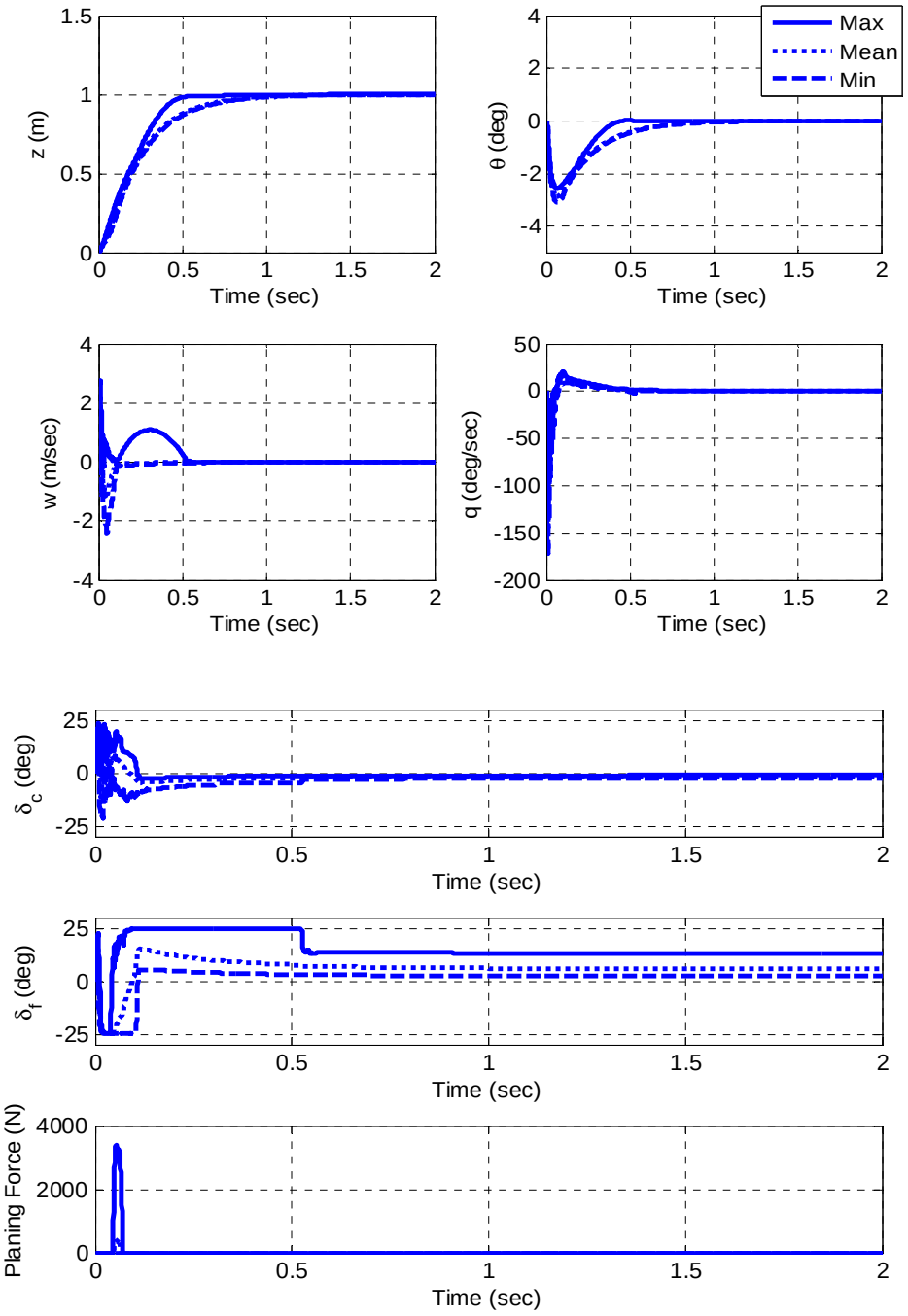

Figure 5-7: Stochastic envelopes of z-step tracking responses, with the Delay-dependent Robust LPV-H_∞ Controller (DRHC).

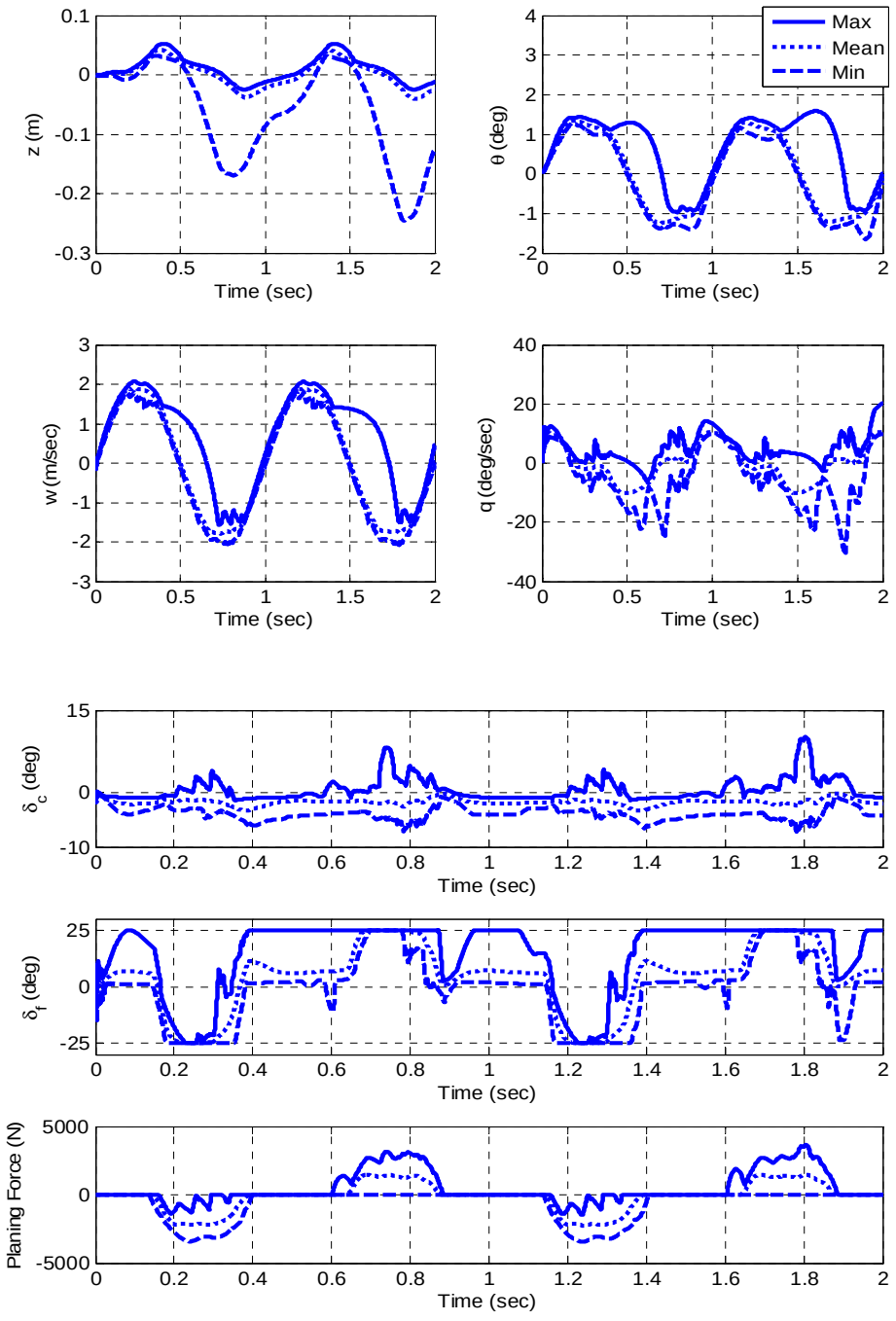

Figure 5-8: Stochastic envelopes of w-tracking responses, with the Delay-dependent Nominal LPV-H_∞ Controller (DNHC).

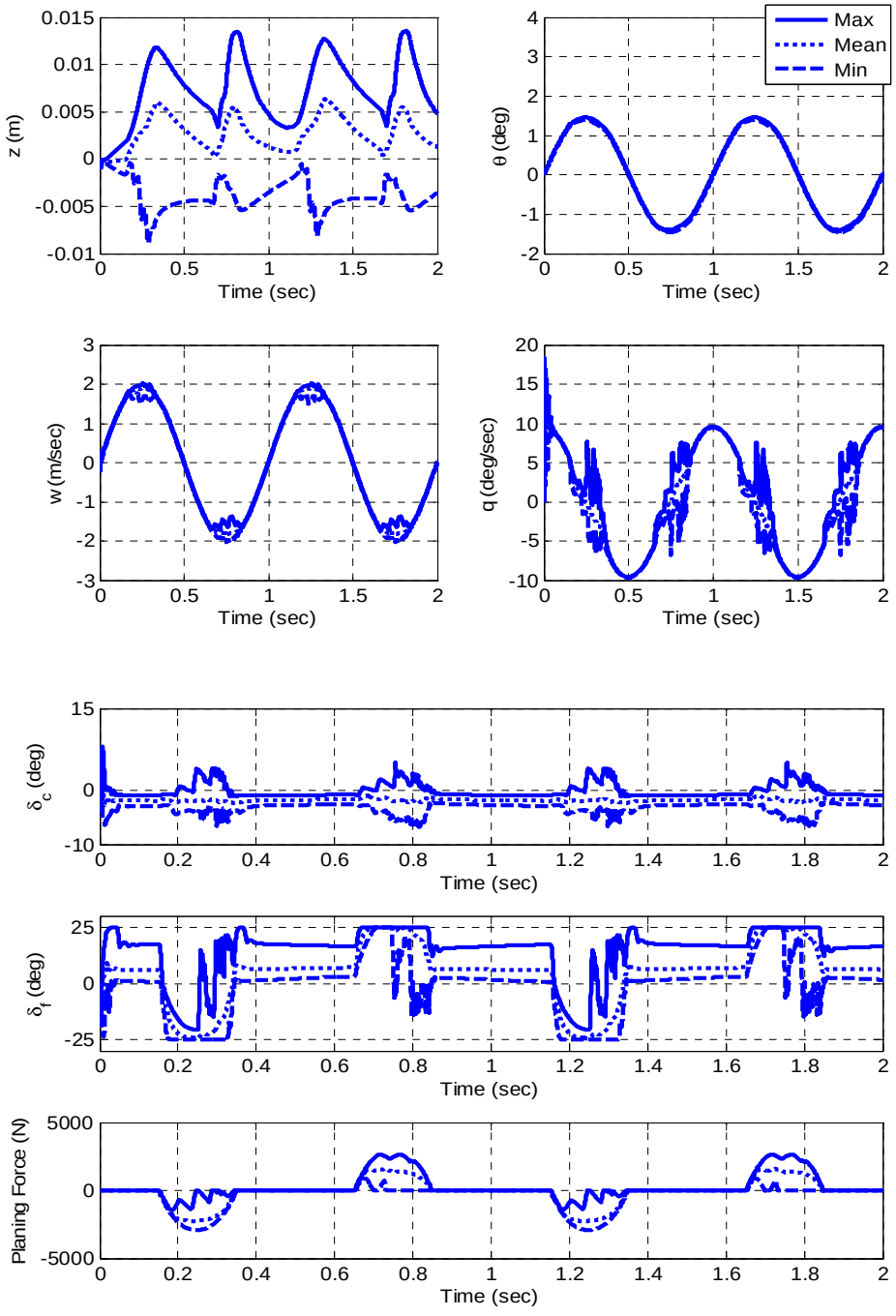

Figure 5-9: Stochastic envelopes of w-tracking responses, with the Delay-dependent Robust LPV-H_∞ Controller (DRHC).

5.5.2 Simulation Results with the High-gain Observer

In this section, we repeat all the simulations shown in the last section for the output feedback controllers. The only difference is that here we include the designed high-gain observer in our consideration assuming an observer is necessary. The high-gain observer parameter is set as ε = 0.00015. For all initial responses, the initial conditions of the high-gain observer are specified as $\hat{z} = 0, \hat{w} = 0$, i.e., the estimated initial $\hat{w}$ is away from its true value.

The simulation results shown in Figs. 5-10 - 5-16 correspond with those shown in Figs. 5-3 - 5-9 respectively. It is clear to see that the closed-loop systems with the high-gain observer can achieve almost the same performance as the closed-loop systems without the observer, in both the nominal performance and the robustness testing simulations.

To further explore the performance of the observer, Fig. 5-17 shows the time histories of the estimation errors e_z and e_w (as defined in Eq. 3.32) when the observer is implemented with the Delay-dependent Nominal LPV-H_∞ Controller (DNHC) or the Delay-dependent Robust LPV-H_∞ Controller (DRHC) controller in initial response, respectively. The high-gain observer parameter is set as ε = 0.00015. Recall that initial conditions of the high-gain observer are specified as $\hat{z} = 0, \hat{w} = 0$; i.e., the estimated initial $\hat{w}$ is away from its true value $w = 3m/sec$. We can see that the state estimation errors converge to zero quickly despite the uncertain nonlinear part $o(z, w, \hat{z}, \hat{w})$ in

Eq. 3.33. This is because the transfer function from $o(z, w, \hat{z}, \hat{w})$ to the estimation errors is almost zero due to the high gain of the observer.

Here we also use simulations to show how the high-gain observer behaves under sensor measurement noise. In the presence of the sensor measurement noise of z, Figs. 5-18 and 5-19 plot the initial responses corresponding to the DNHC and the DRHC combined with a high-gain observer, respectively. The sensor measurement noise used in the simulations is white noise with a power of 10^{-8} and sample time 0.001 sec. Following the discussions in [28], we reset the high-gain observer design parameter $\varepsilon = 0.00001$ for the DNHC controller and $\varepsilon = 0.002$ for the DRHC controller. Note that the ε value is fine tuned for the each controller in order to balance the minimization of state estimation errors against amplification of the sensor measurement noise. It is observed that the controller is still able to stabilize the system, even though the sensor noise causes oscillations in the control inputs δ_c and δ_f. It is also noted that the rate limit for both δ_f and δ_c is reached in both simulations.

Remark 5.5.1: According to the discrete-time and sampled-data implementation of general high-gain observers, addressed in [46] and [47] respectively, the sampling period T could be chosen as $T = \alpha * \varepsilon$ and the parameter $\alpha \in [2, 5]$. Thus, for $\varepsilon = 0.002$ used for the Quasi-LPV H_∞ controller (QLPVHC) designed in Chapter 4 and the Delay-dependent Robust LPV-H_∞ Controller (DRHC), the sample rate is around 100 Hz to 250 Hz; while it seems difficult to implement the observer corresponding to $\varepsilon = 0.00001$ used for the sliding-mode controller (SMC) designed in Chapter 3 and the Delay-dependent Nominal LPV-H_∞ Controller (DNHC).

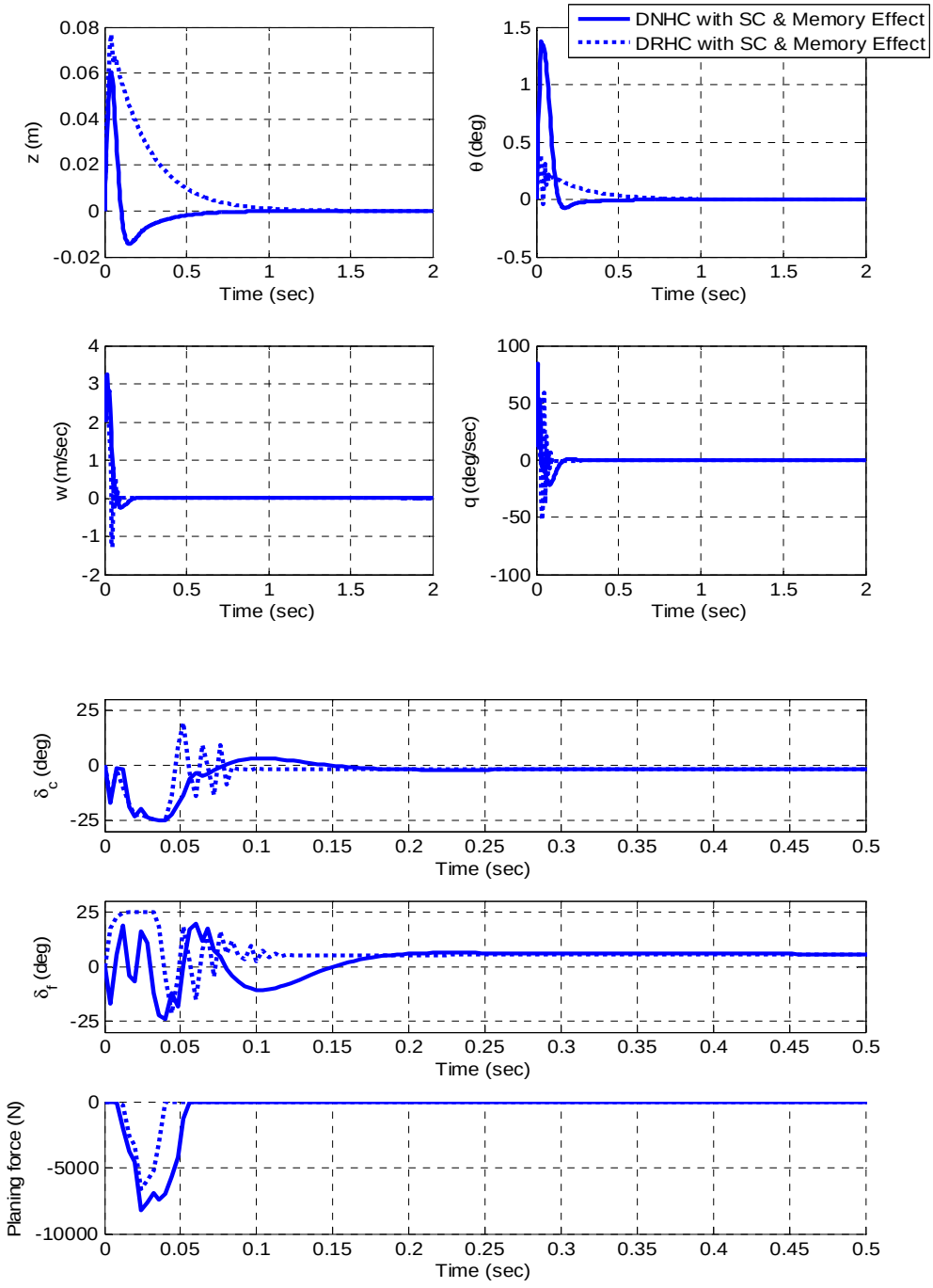

Figure 5-10: Initial response simulations for the nominal system implemented with the Delay-dependent Nominal LPV- H_∞ Controller (DNHC) and the Delay-dependent Robust LPV- H_∞ Controller (DRHC), respectively. The high-gain observer is included.

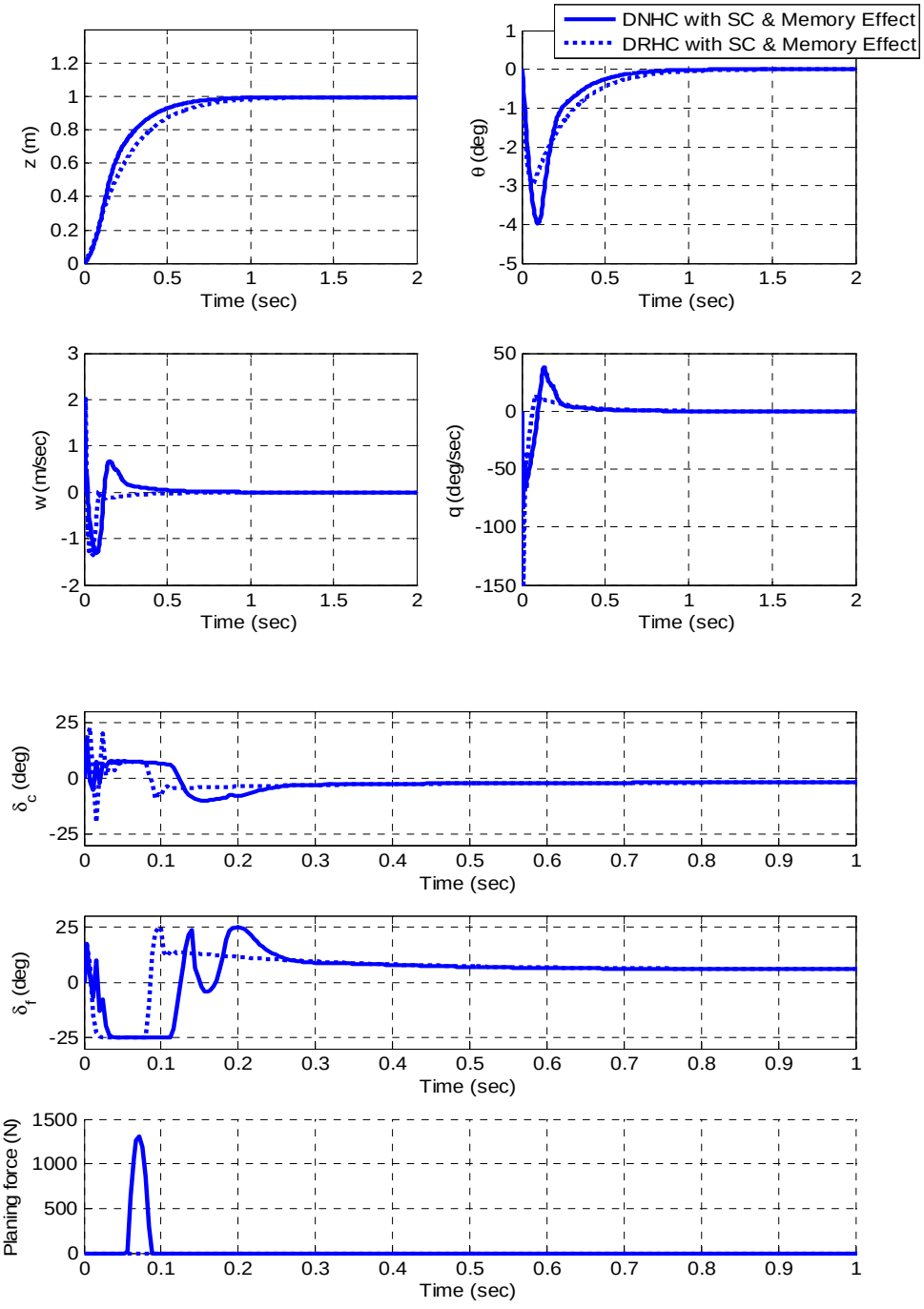

Figure 5-11: z-step responses for the nominal system implemented with the Delay-dependent Nominal LPV-H_∞ Controller (DNHC) and the Delay-dependent Robust LPV-H_∞ Controller (DRHC), respectively. The high-gain observer is included.

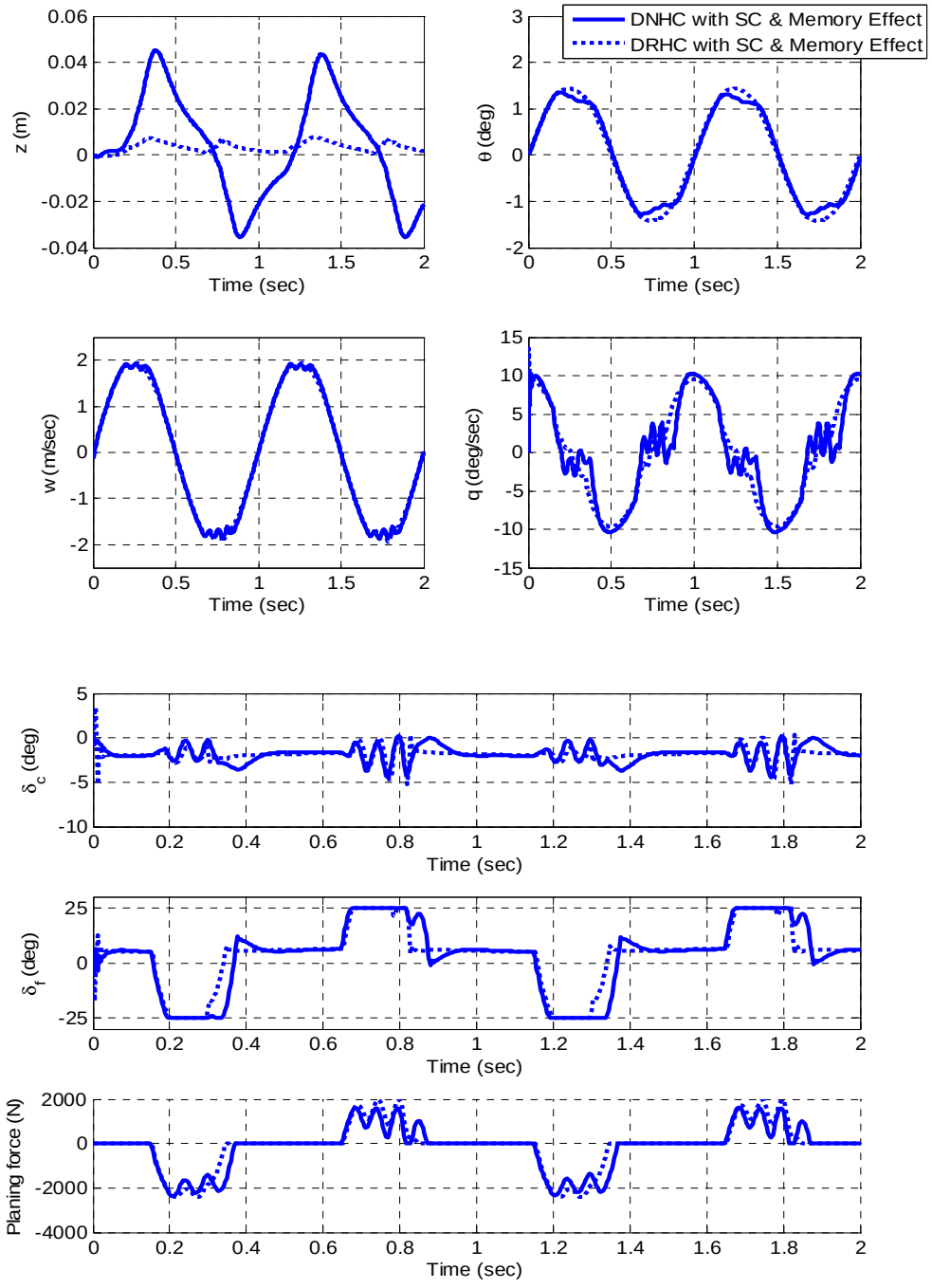

Figure 5-12: w-tracking responses for the nominal system implemented with the Delay-dependent Nominal LPV-H_∞ Controller (DNHC) and the Delay-dependent Robust LPV-H_∞ Controller (DRHC), respectively. The high-gain observer is included.

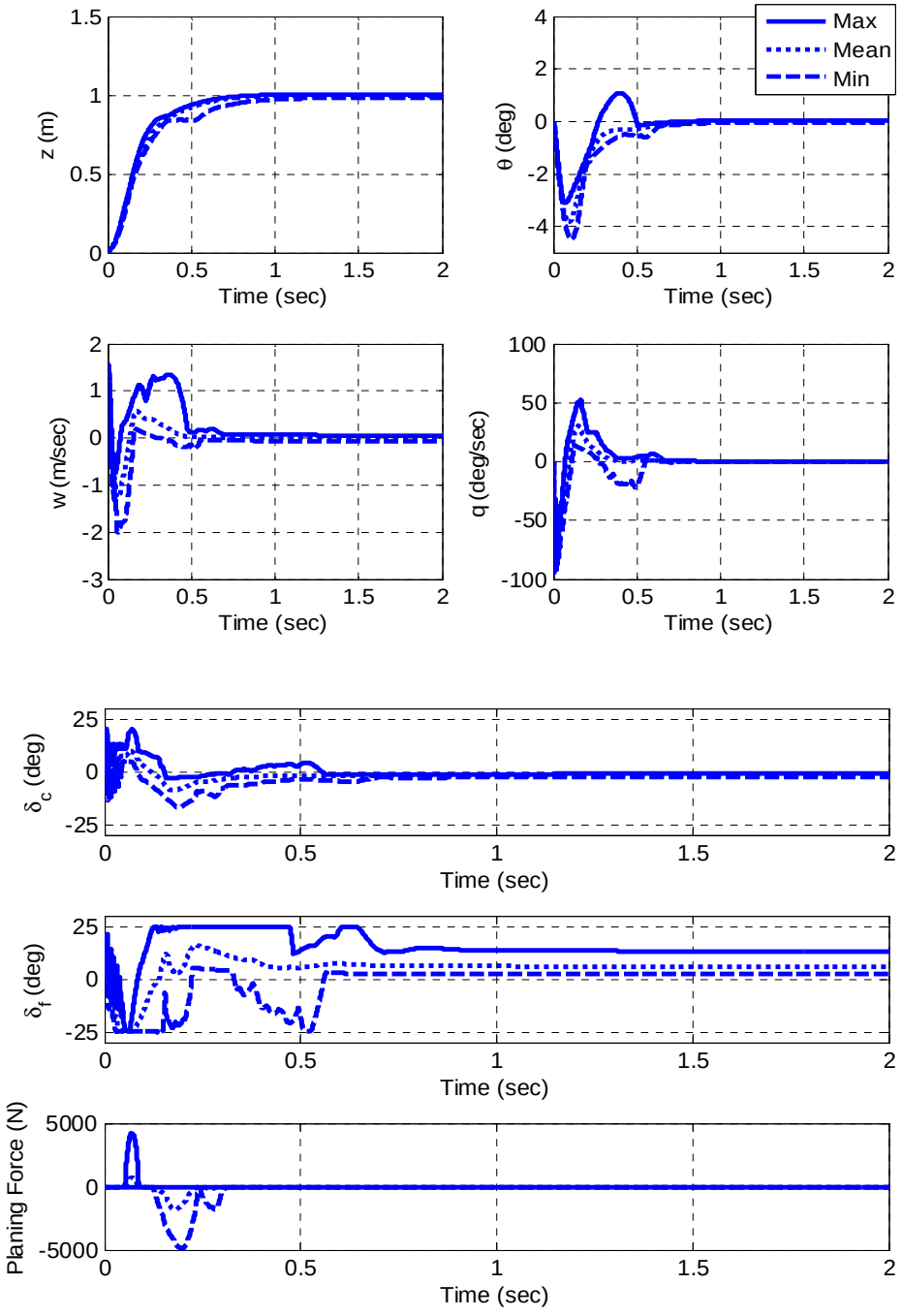

Figure 5-13: Stochastic envelopes of z-step tracking responses, with the Delay-dependent Nominal LPV-H_∞ Controller (DNHC). The high-gain observer is included.

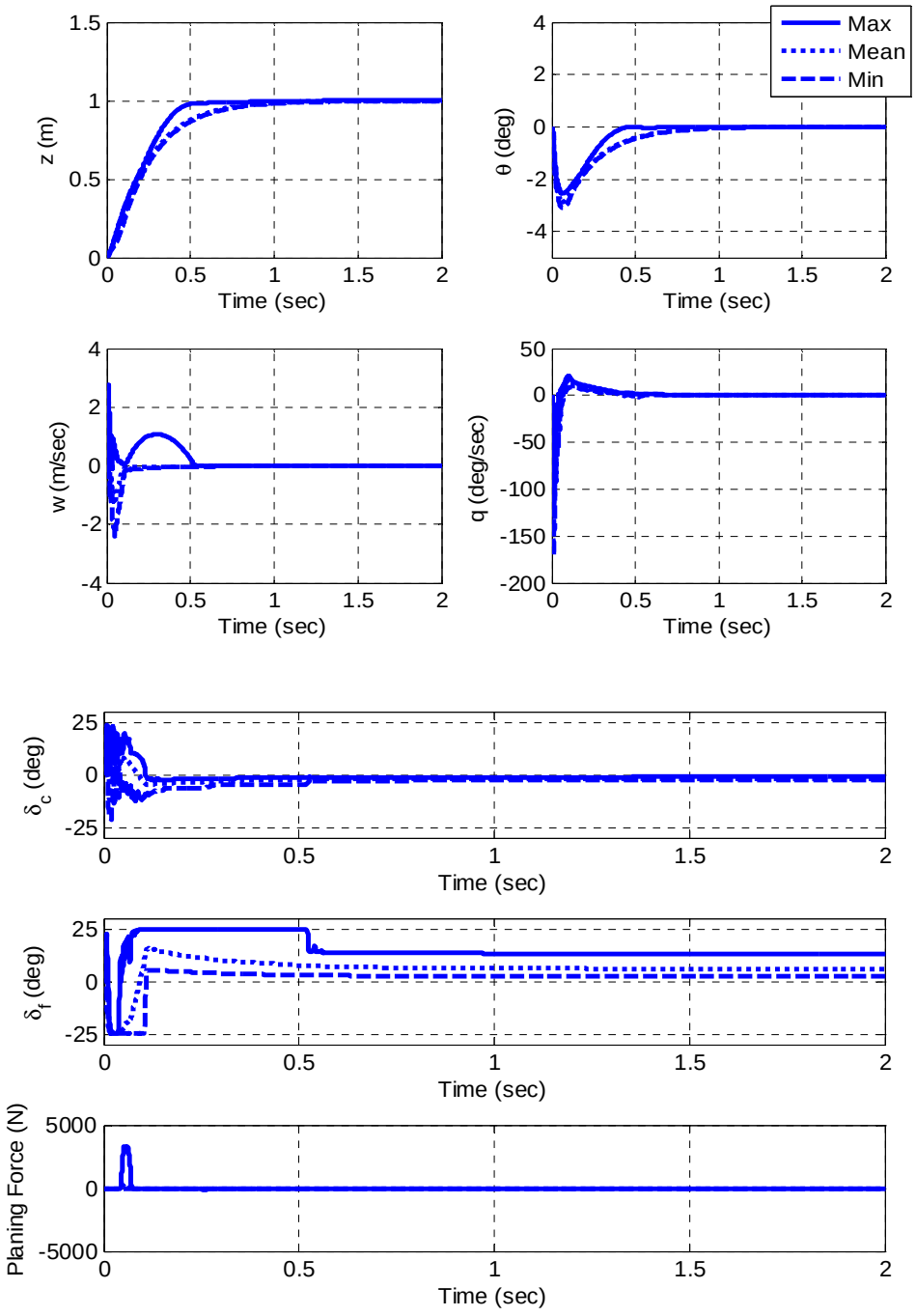

Figure 5-14: Stochastic envelopes of z-step tracking responses, with the Delay-dependent Robust LPV-H_∞ Controller (DRHC). The high-gain observer is included.

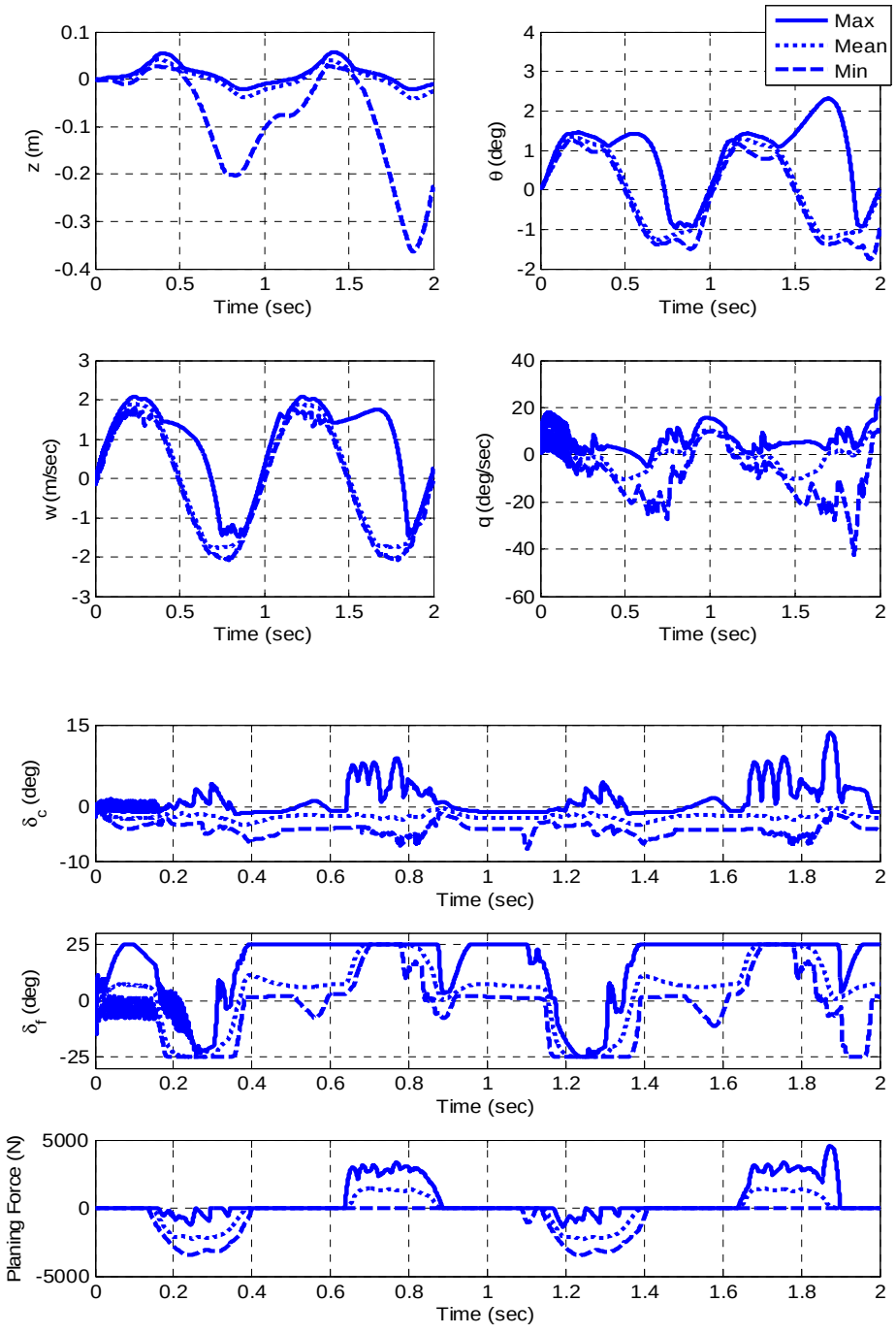

Figure 5-15: Stochastic envelopes of w-tracking responses, with the Delay-dependent Nominal LPV-H_∞ Controller (DNHC). The high-gain observer is included.

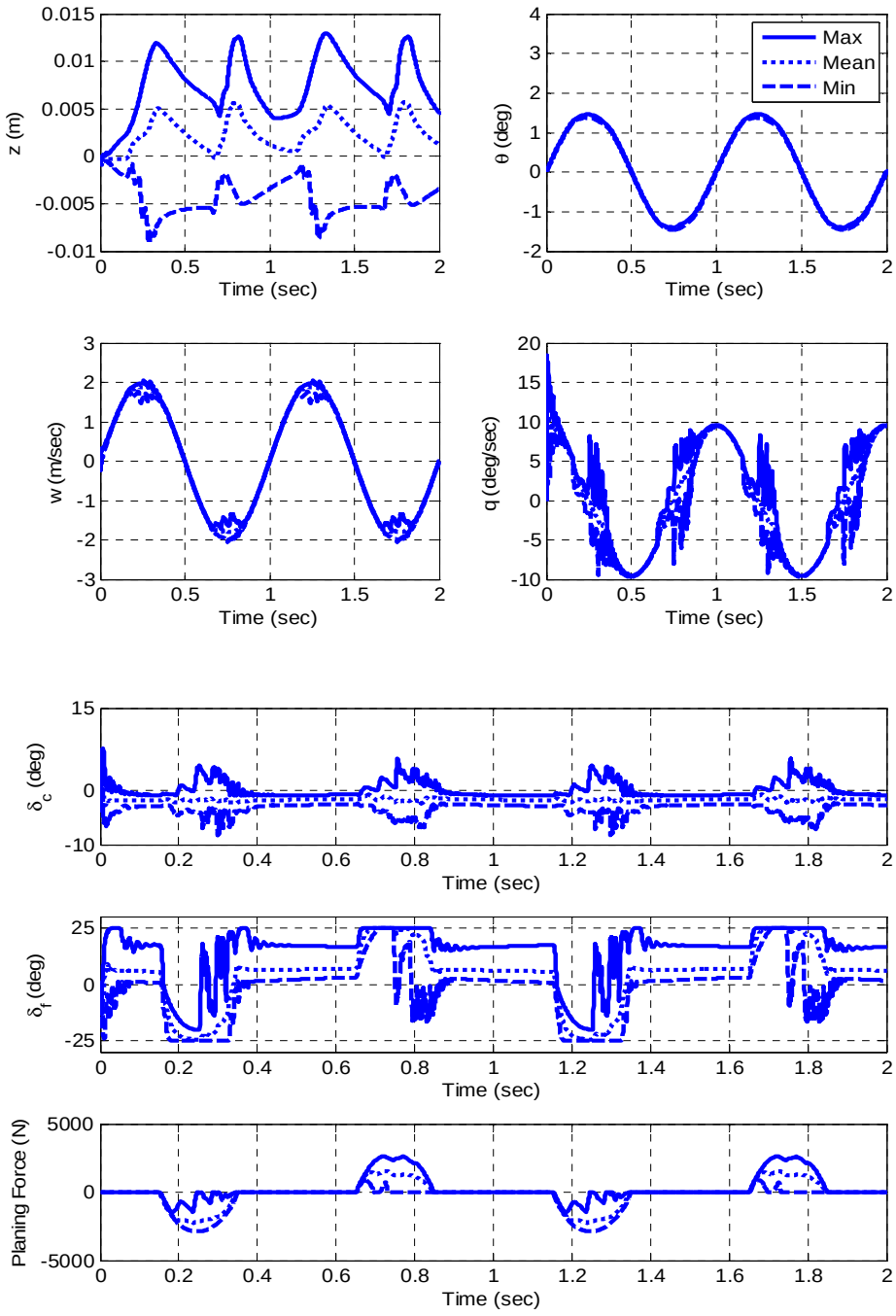

Figure 5-16: Stochastic envelopes of w-tracking responses, with the Delay-dependent Robust LPV-H_∞ Controller (DRHC). The high-gain observer is included.

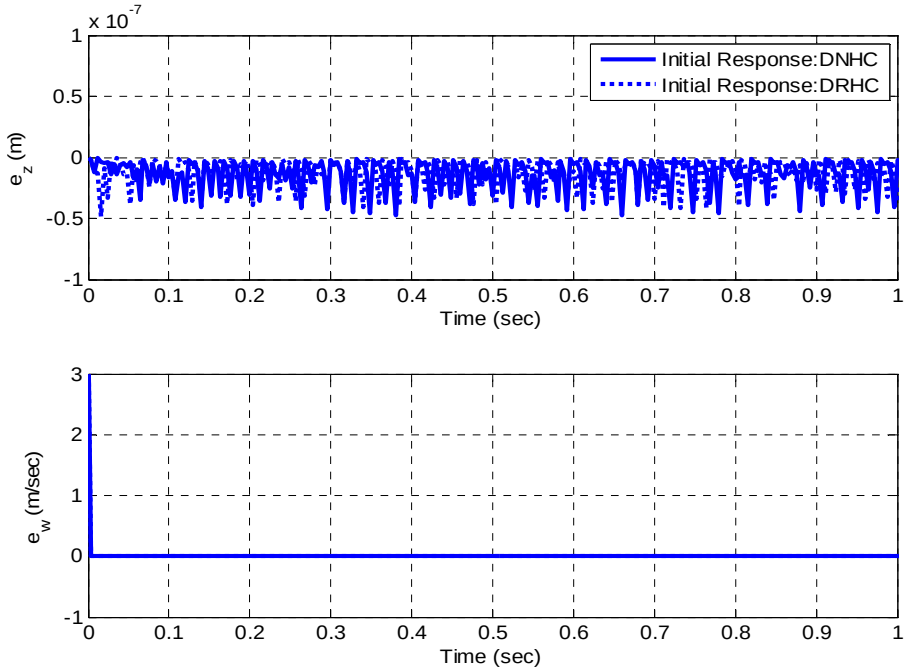

Figure 5-17: Performance of the high-gain observer in closed-loop systems implemented with the Delay-dependent Nominal LPV-H_∞ Controller (DNHC) and the Delay-dependent Robust LPV-H_∞ Controller (DRHC), respectively. No measurement noise is considered.

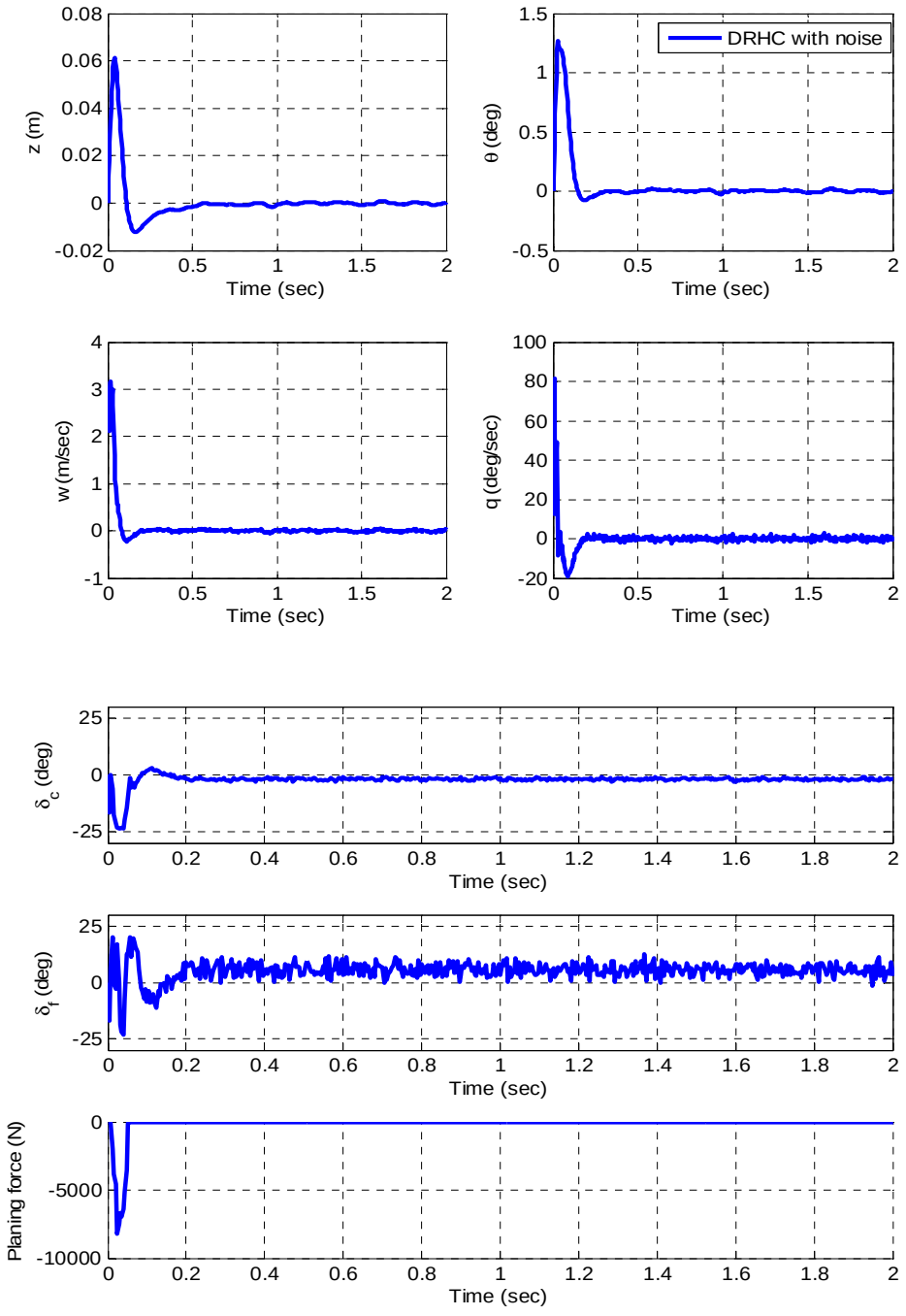

Figure 5-18: Sensitivity of initial response to measurement noise in z, with the Delay-dependent Nominal LPV-H_∞ Controller (DNHC) and the high-gain observer with $\varepsilon = 0.00001$.

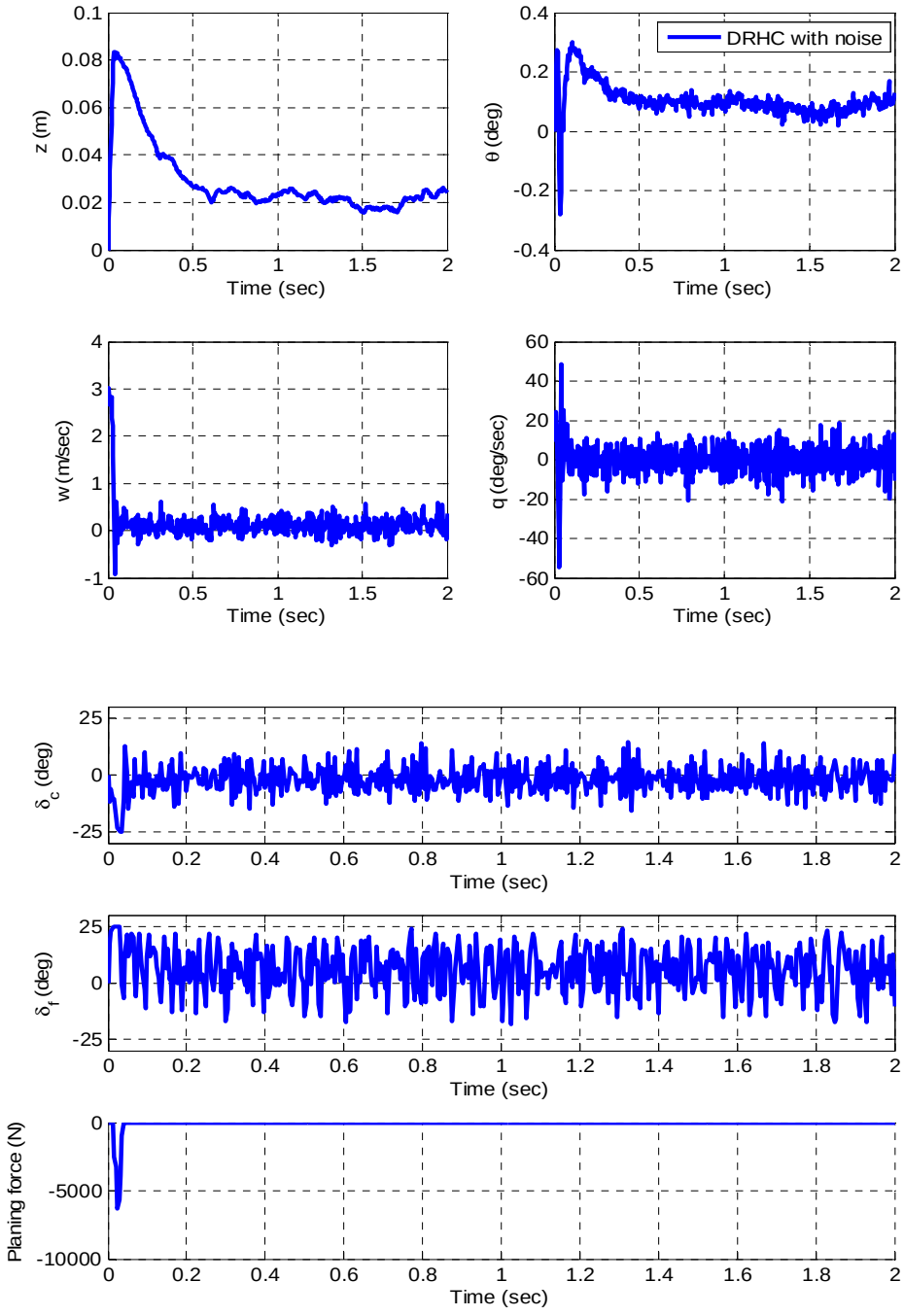

Figure 5-19: Sensitivity of initial response to measurement noise in z, with the Delay-dependent Robust LPV- H_∞ Controller (DRHC) and the high-gain observer with $\varepsilon = 0.002$.

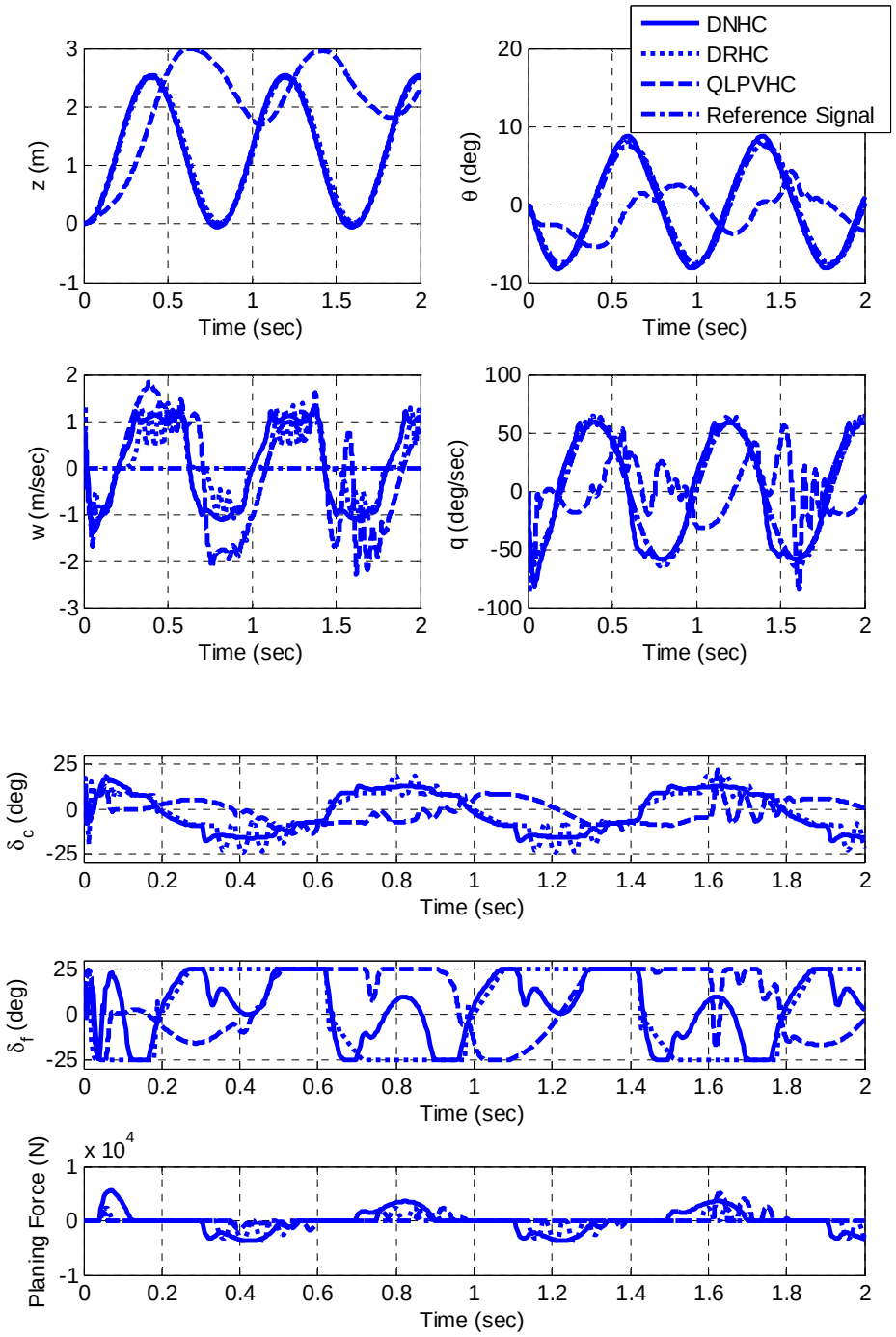

Figure 5-20: Pitch angle tracking responses for the nominal system implemented with the Delay-dependent Nominal LPV- H_∞ Controller (DNHC), the Delay-dependent Robust LPV- H_∞ Controller (DRHC), and the Quasi-LPV H_∞ controller (QLPVHC) respectively.

5.5.3 Compared with the Quasi-LPV H_∞ Controller Designed Based on the Benchmark Model

To further explore the difference between the Delay-dependent Nominal LPV-H_∞ Controller (DNHC), the Delay-dependent Robust LPV-H_∞ Controller (DRHC) and the Quasi-LPV H_∞ controller (QLPVHC) designed in Chapter 4, pitch-angle tracking simulation results are presented in Fig. 5-20. The reference signals for the pitch-angle tracking are $w_r(t) = 0$ and $\theta_r = -\frac{1}{V}\dot{z}_r$, where the reference signal for z is defined as follows,

$$z_r = 1.25 + 1.25\sin(\frac{5\pi}{2}t - \frac{\pi}{2}) \qquad 5.44$$

and by system dynamics, the reference pitch rate q_r is calculated as $q_r = \dot{\theta}_r$.

Fig. 5-20 shows that both the DNHC and DRHC can track the pitch-angle reference signal satisfactorily, while the QLPVHC is not able to achieve satisfactory tracking performance. One possible reason could due to that the QLPVHC is designed based on the Benchmark Model which ignores the memory effect of the cavity-vehicle interaction.

Chapter 6

Conclusions and Future Work

6.1 Conclusions

This dissertation focuses on control designs for two pitch-plane-dynamics models of a supercavitating vehicle: the Benchmark Model, which does not take into account the memory effect of the planing force, and the Time-Delay Benchmark Model, which is a state-delay model that includes the cavity memory effect. Based on the Benchmark Model, a sliding-mode controller (SMC) and a Quasi-LPV H_∞ controller (QLPVHC) are designed to achieve stability and tracking performance of the closed-loop systems. Nominal performance and robustness evaluations of the two controllers are also conducted with the Time-Delay Benchmark Model. The corresponding simulation results show that the performance of the two controllers, though designed based on the non-time-delay Benchmark Model, is satisfactory for unit z-step input tracking and w tracking (though in which the desired θ_r is not well followed). However, the QLPVHC controller designed based on the Benchmark Model has poor performance in the pitch-angle tracking response. This is consistent with the observations of several other papers that ignoring the cavity-vehicle memory in the modeling could hurt the controller performance substantially. Consequently, based on the Time-Delay Benchmark Model, a Delay-dependent Nominal Quasi-LPV H_∞ Controller (DNHC) and a Delay-dependent Robust Quasi-LPV H_∞ Controller (DRHC) are designed. Compared with the QLPVHC,

the DNHC and DRHC show better transient performance and much better tracking performance, especially in the pitch-angle tracking response. When there is uncertainty associated with hydrodynamic coefficients, the designed robust controller DRHC has much better performance in robustness compared with the nominal controller DNHC.

Considering that it is difficult to measure the vertical speed of a supercavitating vehicle for feedback control, a high-gain observer is designed based on the measurement of vehicle depth. The observer shows good nominal estimation performance when the sensor measurement noise is not included. In practice when the sensor measurement noise model is available, different observer gains must be selected to balance estimation performance against noise amplification due to the high gain. The observer gains that are selected will depend on which controller the observer output is fed to. Additionally, the physical amplitude limits of actuators lead us to design a saturation compensation to coordinate the control inputs to actuators of the cavitator and fins. It is observed that, without the compensation, actuator amplitude saturation will result in instability in most simulations. We also show that all closed-loop systems with saturation compensation are stable, although the rate limit of actuators is also touched in most cases.

6.2 Future Work

In the Time-Delay Benchmark Model, the fin effectiveness ratio, i.e. n, is assumed constant. This might be a significant disadvantage of the model. A higher fidelity fin force model would improve the model significantly and be beneficial for control design. The (Time-Delay) Benchmark Models and the corresponding controllers

only address longitudinal dynamics. Modeling and control designs for the full six-DOF supercavitating vehicle will enable more complicated maneuvers.

As shown in Chapter 5, the delay-dependent robust LPV-H_∞ control design is conservative; no feasible solutions could be found for uncertainties higher than 3% in the system parameters and the hydrodynamic coefficients to guarantee robust stability; however, 40% uncertainties can be tolerated in tracking simulations. It is possible to reduce the conservativeness of the control design by constructing a parameter-dependent Lyapunov-Krasovskii functional for the time-delay LPV system.

In addition, the work done so far assumes the reference signals are commanded to a supercavitating vehicle at steady trim velocity. It would be interesting to see the tracking performance when a reference signal is commanded to a vehicle right after launch. As velocity increase and cavity grows, the more complicated cavity-vehicle interaction might make a significant difference in tracking performance.

Bibliography

(1) Dzielski, J. and Kurdila, A., 2003. "A benchmark control problem for supercavitating vehicles and an initial investigation of solutions," *Journal of Vibration and Control*, vol. 9, no. 7, pp. 791-804.

(2) Fine, N. E. and Kinnas, S. A., 1993. "A boundary element method for the analysis of the flow around 3-D cavitating hydrofoils," *Journal of Ship Research*, 37(1).

(3) Kamada, R., 2005. Trajectory Optimization Strategies for Supercavitating Vehicles. MS Thesis, Georgia Tech.

(4) Kirschner, I., Kring, D. C., Stokes, A. W., Fine, N. E., and Uhlman, J. S., 2002. "Control strategies for supercavitating vehicle," *Journal of Vibration and Control*, vol. 8, pp. 219-242.

(5) Kulkarni, S. S. and Pratap, R., 2000. "Studies on the dynamics of a supercavitating projectile," *Applied Mathematical Modeling*, vol. 24, n. 2, pp. 113-129.

(6) Lin, G., Balachandran, B., and Abed, E., 2004. "Dynamics and control of supercavitating bodies," in *Proceedings of ASME IMECE*, Anaheim, CA.

(7) Lin, G., Balachandran, B., and Abed, E., 2005. "Supercavitating body dynamics, bifurcations and control," in *Proceedings of American Control Conference*, Portland, OR.

(8) Lin, G., Balachandran, B., and Abed, E., 2006. "Bifurcation behavior of a supercavitating vehicle," in *Proceedings of ASME IMECE*, Chicago, IL.

(9) May, A., 1974. “Water entry and the cavity-running behavior of missiles,” Naval Sea Systems Command, Arlington, VA, SEAHAC TR 75-82.

(10) Rand, R., Pratap, R., Ramani, D., Cipolla, J., and Kirschner, I., 1997. “Impact dynamics of a supercavitating underwater projectile,” in *Proceedings of DETC’97 ASME Design Engineering Technical Conferences.*

(11) Shao, Y., Mesbahi, M., and Balas, G., 2003. “Planing, switching, and supercavitating flight control,” in *Proceedings of AIAA Guidance, Navigation, and Control Conference and Exhibit*, AIAA 2003-5724, Austin, TX.

(12) Vanek, B., Bokor, J., and Balas, G., 2006. “Theoretical aspects of high-speed supercavitation vehicle control,” in *Proceedings of American Control Conference*, Minneapolis, MN, pp. 5263-5268.

(13) Vanek, B., Bokor, J., and Balas, G., 2006. “High-speed Supercavitation Vehicle Control,” *AIAA Guidance, Navigation and Control Conference and Exhibit*, Keystone, CO.

(14) Lin, G., Balachandran, B., and Abed, E., 2006. “Nonlinear dynamics and control of supercavitating bodies,” in *Proceedings of AIAA Guidance, Navigation, and Control Conference and Exhibit*, Keystone, CO.

(15) Goel, A., 2002. Control Strategies for Supercavitating Vehicles, MS Thesis, Univ. of Florida.

(16) Ahn, S., 2007. An Integrated Approach to the Design of Supercavitating Underwater Vehicles, PhD Thesis, Georgia Institute of Technology.

(17) Zribi, M., and Mahmoud, M., 1999. “ H_∞ -control design for systems with multiple delays,” *Computers and Electrical Engineering*, vol. 25, pp. 451-475.

(18) Vanek, B., Bokor, J., Balas, G., and Arndt, R., 2007. “Longitudinal motion control of a high-speed supercavitation vehicle,” *Journal of Vibration and Control*, vol. 13, n. 2, pp. 159-184.

(19) Levant, A., 2003. “High order sliding modes, differentiation and output feedback control,” *International Journal of Control*, vol. 76, pp. 924-941.

(20) Richards, N. D., Monaco, J. F., and Knospe, C. R., 2006. “Application of robust state and parameter estimation to a supercavitating torpedo model,” in *Proceedings of AIAA Guidance, Navigational, and Control Conference and Exhibit*, Keystone, CO, August 2006. AIAA paper 2006-6444.

(21) Khalil, H., *Nonlinear Systems*, Prentice Hall, 2002.

(22) Vasiljevic, L. and Khalil, H., 2006. “Differentiation with high-gain observers in the presence of measurement noise,” in *Proceedings of the 45th IEEE Conference on Decision & Control*, San Diego, CA, pp. 4714-4722.

(23) Soroush, M. and Valluri, S., 1999. “Optimal directionality compensation in processes with input saturation nonlinearities,” *International Journal of Control*, vol. 72, n. 17, pp. 1555-1564.

(24) Zheng, A., Kothare, M. V., and Morari, M., 1994. “Antiwindup Design for Internal Model Control,” *International Journal of Control*, vol. 60, pp.1015-1024.

(25) Doyle, J. C., Smith, R. S., and Enns, D. F., 1987. “Control of Plants with Input Saturation Nonlinearities,” in *Proceedings of American Control Conference*, pp.1034-1039.

(26) Hanus, R. and Kinnaert, M., 1989. “Control of Constrained Multivariable System Using Conditioning Technique,” in *Proceedings of American Control Conference*, pp.1711-1718.

(27) Mhatre, S. and Brosilow, C., 1996. “Multivariable Model State Feedback,” in *Proceedings of IFAC WC*, San Francisco, pp.139.

(28) Vasiljevic, L. and Khalil, H., 2006. “Differentiation with high-gain observers in the presence of measurement noise,” in *Proceedings of the 45th IEEE Conference on Decision & Control*, San Diego, CA, pp. 4714-4722.

(29) Apkarian, P., Gahinet, P., and Becker, G., 1995. “Self-scheduled H_∞ control of Linear Parameter-varying Systems: a design example,” *Automatica*, vol. 31, n. 9, pp. 1251-1261, 1995.

(30) Wu, F., Yang, H. X., Packard, A., and Becker, G., 1996. “Induced L_2-Norm control for LPV system with bounded parameter variation,” *International Journal of Nonlinear and Robust Control*, vol. 6, pp. 983-998.

(31) Yu, J., Jadbabaie, A., Primbs, J., and Huang, Y., 2001. “Comparison of nonlinear control designs for a ducted fan model,” *Automatica*, vol. 37, n. 12, pp. 1971-1978.

(32) Narendra, K. S. and Balakrishnan, J., 1994. “A common Lyapunov function for stable LTI systems with commuting A-matrices,” *IEEE Transactions on Automatic Control*, vol. 39, No. 12, pp. 2469-2471.

(33) Zribi, M. and Mahmoud, M., 1999. “H_∞-control design for systems with multiple delays,” *Computers and Electrical Engineering*, vol. 25, pp. 451-475.

(34) Kim, J. and Park, H., 1999. " H_∞ state feedback control for generalized continuous/discrete time-delay systems," *Automatica*, 35, pp. 1443-1451.

(35) De Souza, C. E. and Li, X., 1999. "Delay-dependent robust H_∞ control of uncertain linear state-delayed systems," *Automatica*, vol. 35, pp. 1313-1321.

(36) Moon, Y., Park, P., Kwon, W., and Lee, Y., 2001. "Delay-dependent robust stabilization of uncertain state-delayed systems," *International Journal of Control*, vol. 74, n. 14, pp. 1447-1455.

(37) Lee, Y., Moon Y., Kwon, W., and Park, P., 2004. "Delay-dependent robust H_∞ control for uncertain systems with a state-delay," *Automatica*, vol. 40, pp. 65-72.

(38) Nishihira, N. and Yasuda, K., 2003. "LMI approach in stability and control of time-delay systems," *SICE Annual Conference*, Japan.

(39) Richard, J., 2003. "Time-delay systems: an overview of some recent advances and open problems," *Automatica*, vol. 39, pp. 1667-1694.

(40) Zhang, X., Tsiotras, P., and Knospe, C., 2002. "Stability analysis of LPV time-delayed systems," *International Journal of Control*, vol. 75, n. 7, pp. 538-558.

(41) Wu, F. and Grigoriadis, K. M., 2001. "LPV systems with parameter-varying time delays: analysis and control," *Automatica*, vol. 37, 2001, pp. 221-229.

(42) Wu, F., 2001. "Delay-dependent induced L_2 norm analysis and control for LPV systems with state delays," in *Proceedings of the 2001 ASME IMECE*, New York, pp. 597-602.

(43) Sun, M., Jia, Y., Du, J. and Yuan, S., 2007. "Delay-dependent H_∞ control for LPV systems with time delays," in *Proceedings of 46th IEEE Conference on Decision and Control*, New Orleans, LA, pp. 2089-2093.

(44) Lee, Y., Kwon, W., and Park, P., 2007. "Author's reply: comments on delay-dependent robust H_∞ control for uncertain systems with a state-delay," *Automatica*, vol. 43, pp. 572-573.

(45) El Ghaoui, L., Oustry, F., and AitRami, M., 1997. "A cone complementarity linearization algorithm for static output-feedback and related problems," *IEEE Transactions on Automatic Control*, vol. 42, pp. 1171-1176.

(46) Dabroom, A. and Khalil, H. K., 1999. "Discrete-time implementation of high-gain observers for numerical differentiation," *International Journal of Control*, vol. 72, pp. 1523-1537.

(47) Dabroom, A. and Khalil, H. K., 2001. "Output feedback sampled-data control of nonlinear systems using high-gain observers," *IEEE Transactions on Automatic Control*, vol. 46, n. 11, pp. 1712-1725.

(48) Wu, F., 1995. Control of Linear Parameter Varying Systems. Phd Thesis, University of California at Berkeley.

(49) Slotine, J. E. and Li, W., *Applied Nonlinear Control*, Prentice Hall, 1991.

(50) Kirschner, I. N., Uhlman, J. S., Vargheses, A. N., and Kuria, I. M., 1995. "Supercavitating projectiles in axisymmetric subsonic liquid flows," *Amer. Soc. Mech. Eng., Fluids Eng. Div.*, vol. 210, pp. 75-93.

(51) Lindau, J. W., Venkateswaran, S., Kunz, R. F., and Merkle, C. L., 2001. “Development of a fully compressible multi-phase Reynolds-averaged Navier-Stokes model,” AIAA Paper 2001-2648.

(52) Lindau, J. W. and Kunz, R. F., 2004. "Advancement and Application of multiphase CFD modeling to high speed supercavitating flows," Report N00014-01-1-0325, Applied Research Laboratory, Pennsylvania State University.

(53) Ruzzene, M. and Soranna, F., 2002. “Impact dynamics of elastic supercavitating underwater vehicles,” in *Proceedings of the AIAA/ISSMO Symposium on Multidisciplinary Analysis and Optimization*, Atlanta, GA, Sep. 4-6, AIAA Paper 2002-5632.

(54) Ruzzene, M., 2004. “Non-axisymmetric buckling of stiffened supercavitating shells: static and dynamic analysis,” *Computers and Structures*, vol. 82, pp. 257-269.

(55) Alyanak, E., Venkayya, V., Grandhi, R., and Penmetsa, R., 2005. “Structural response and optimization of a supercavitating torpedo,” *Finite Elements in Analysis and Design*, vol. 41, pp. 563-582.

(56) Logvinovich, G. V., 1980. “Some questions about planing,” *Transactions of Central Aerohydrodynamics Institute*, n. 2052, Moscow.

(57) Ruzzene, M., Kamada, R., Botasso, C. L., and Scorcelletti, F., 2008. “Trajectory optimization strategies for supercavitating underwater vehicles,” *Journal of Vibration and Control*, vol. 14, n. 5, pp. 611-644.

(58) Bottasso, C. L., Scorcelletti, F., Ruzzene, M., and Ahn, S. S., 2009. “Trajectory optimization for DDE models of supercavitating underwater vehicles”. *Journal of Dynamic Systems, Measuremen and Control*, vol. 131, n. 1, p 011009.

(59) Logvinovich, G. V., 1972. “Hydrodynamics of Free-Boundary Flow”. Tech. rep., U.S. department of Commerce, Washington, DC, translated from the Russian (NASA-TT-F-658).

(60) Fine, N., 2000. “Six degree-of-freedom Fin Forces for the ONR Supercavitating Test Bed Vehicle”. Anteon Corporation, http://www.anteon.com.

(61) Hassan, S. E., 2004. “Analysis of hydrodynamic planing forces associated with cavity riding vehicles”. private communication.

Appendix A

Proofs of Theorems in Chapter 5

In order to prove the Theorems in Chapter 5, equivalent conditions to Eq. 5.11 are utilized. By [37], Eq. 5.11 is equivalent to $\Xi < 0$ as follows:

$$\Xi = \begin{bmatrix} \varphi_{11} & \varphi_{12} & \varphi_{13} \\ * & -Q + C_1^T C_1 & 0 \\ * & * & -\gamma^2 I + D_w^T D_w \end{bmatrix} < 0 \qquad \text{A.1}$$

with

$$\begin{aligned} \varphi_{11} &= \begin{bmatrix} 0 & I \\ A & -I \end{bmatrix}^T P + P^T \begin{bmatrix} 0 & I \\ A & -I \end{bmatrix} + \overline{\tau} \begin{bmatrix} X_{11} & X_{12} \\ * & X_{22} \end{bmatrix} \\ &\quad + \begin{bmatrix} Q + C^T C + Y_1 + Y_1^T & Y_2^T \\ * & \overline{\tau} Z \end{bmatrix} \\ \varphi_{12} &= P^T \begin{bmatrix} 0 \\ A_d \end{bmatrix} - \begin{bmatrix} Y_1 \\ Y_2 \end{bmatrix} \\ \varphi_{13} &= P^T \begin{bmatrix} 0 \\ B_w \end{bmatrix} + \begin{bmatrix} C^T D_w \\ 0 \end{bmatrix} \end{aligned} \qquad \text{A.2}$$

Proof of Theorem 5.3.1:

By comparing the new system (Eqs. 5.15 - 5.16) to the system (Eq. 5.10) in Lemma 5.3.1, we have $A \to (A - BK)$, $A_d \to A_d$, $B_w \to BK$, $C \to -\begin{bmatrix} I \\ K \end{bmatrix}$, $D_w \to \begin{bmatrix} I \\ K \end{bmatrix}$, and $C_1 \to 0$. Accordingly, Eq. A.1 and Eq. A.2 become

$$\Xi = \begin{bmatrix} \varphi_{11} & \varphi_{12} & \varphi_{13} \\ * & -Q & 0 \\ * & * & -\gamma^2 I + \begin{bmatrix} I_{4\times4} \\ K \end{bmatrix}^T \begin{bmatrix} I_{4\times4} \\ K \end{bmatrix} \end{bmatrix} < 0 \qquad \text{A.3}$$

$$\begin{aligned} \varphi_{11} &= \begin{bmatrix} 0 & I \\ A - BK & -I \end{bmatrix}^T P + P^T \begin{bmatrix} 0 & I \\ A - BK & -I \end{bmatrix} \\ &\quad + \bar{\tau} \begin{bmatrix} X_{11} & X_{12} \\ * & X_{22} \end{bmatrix} + \begin{bmatrix} Q + \begin{bmatrix} I_{4\times4} \\ K \end{bmatrix}^T \begin{bmatrix} I_{4\times4} \\ K \end{bmatrix} + Y_1 + Y_1^T & Y_2^T \\ * & \bar{\tau} Z \end{bmatrix} \\ \varphi_{12} &= P^T \begin{bmatrix} 0 \\ A_d \end{bmatrix} - \begin{bmatrix} Y_1 \\ Y_2 \end{bmatrix} \\ \varphi_{13} &= P^T \begin{bmatrix} 0 \\ BK \end{bmatrix} + \begin{bmatrix} -\begin{bmatrix} I_{4\times4} \\ K \end{bmatrix}^T \begin{bmatrix} I_{4\times4} \\ K \end{bmatrix} \\ 0 \end{bmatrix} \end{aligned} \qquad \text{A.4}$$

Define the following change of variables,

$$L_4 = \begin{bmatrix} L_1 & 0 \\ L_2 & L_3 \end{bmatrix} = \begin{bmatrix} P_1 & 0 \\ P_2 & P_3 \end{bmatrix}^{-1}, \quad \begin{bmatrix} M_{11} & M_{12} \\ * & M_{22} \end{bmatrix} = L_4^T \begin{bmatrix} X_{11} & X_{12} \\ * & X_{22} \end{bmatrix} L_4$$
$$\begin{bmatrix} N_1 \\ N_2 \end{bmatrix} = L_4^T \begin{bmatrix} Y_1 \\ Y_2 \end{bmatrix} L_1, \; W = L_1 Q L_1, \; S = Z^{-1}, \; U = K L_1 \qquad \text{A.5}$$

Pre-multiply Ξ by $diag\{L_4^T \quad L_1 \quad I\}$ and post-multiply Ξ by $diag\{L_4 \quad L_1 \quad I\}$, and then followed by algebraic reductions including Schur complement, Eq. A.3 and Eq. A.4 are reduced to,

$$\begin{bmatrix} \Gamma_{11} & \Gamma_{12} & -N_1 & 0 & -L_1 & -U^T & \bar{\tau} L_2^T \\ * & \Gamma_{22} & A_d L_1 - N_2 & BUL_1^{-1} & 0 & 0 & \bar{\tau} L_3^T \\ * & * & -W & 0 & 0 & 0 & 0 \\ * & * & * & -\gamma^2 I & I & L_1^{-1} U^T & 0 \\ * & * & * & * & -I & 0 & 0 \\ * & * & * & * & * & -I & 0 \\ * & * & * & * & * & * & -\bar{\tau} S \end{bmatrix} < 0 \qquad \text{A.6}$$

and

$$\begin{bmatrix} M_{11} & M_{12} & N_1 \\ * & M_{22} & N_2 \\ * & * & L_1 S^{-1} L_1 \end{bmatrix} \geq 0$$

with

$$\Gamma_{11} = L_2 + L_2^T + W + N_1 + N_1^T + \bar{\tau} M_{11}$$
$$\Gamma_{12} = (AL_1 - BU)^T - L_2^T + L_3 + N_2^T + \bar{\tau} M_{12}$$
$$\Gamma_{22} = -L_3 - L_3^T + \bar{\tau} M_{22}$$

As $L_1 > 0$, pre- and post-multiply Eq. A.6 by $Diag\{I, I, I, L_1, I, I, I\}$, then Eq. A.6 becomes Eq. 5.18. □

Lemma 5.3.3 ([37]) Let F, E and Δ be real matrices of appropriate dimensions with $\Delta(t) = diag\{\Delta_1(t), \cdots, \Delta_\nu(t)\}$, $\Delta_i^T(t)\Delta_i(t) \le I$, $i = 1, \cdots, \nu$. Then, for any real matrix $\Lambda = diag\{\lambda_1 I, \cdots, \lambda_\nu I\} > 0$, the following inequality holds:

$$F\Delta E + E^T\Delta^T F^T \le F\Lambda F^T + E^T\Lambda^{-1}E \qquad \text{A.7}$$

By Lemma 5.3.3 and Theorem 5.3.1, the proof of Theorem 5.3.2 is given as follows:

Let Ψ denote the left hand side of the inequality in Eq. 5.18. Then substitute matrices $A + F\bar{\Delta}(t)E$, $A_d + F\bar{\Delta}(t)E_d$ and $B + F\bar{\Delta}(t)E_b$ for matrices A, A_d and B respectively in Eq. 5.18. It suffices to prove Theorem 5.3.2 if the inequality in Eq. 5.18 still holds after the substitution. After substituting $A + F\bar{\Delta}(t)E$, $A_d + F\bar{\Delta}(t)E_d$ and $B + F\bar{\Delta}(t)E_b$, the inequality in Eq. 5.18 becomes,

$$\Psi + \bar{F}\bar{\Delta}\bar{E} + \bar{E}^T\bar{\Delta}^T\bar{F}^T < 0 \qquad \text{A.8}$$

where

$$\bar{F} = \begin{bmatrix} 0 & F^T & 0 & 0 & 0 & 0 & 0 \end{bmatrix}^T$$
$$\bar{E} = \begin{bmatrix} EL_1 - E_bU & 0 & E_dL_1 & E_bU & 0 & 0 & 0 \end{bmatrix}$$

According to Lemma 5.3.3, Eq. A.8 holds if there exists $\Lambda = diag\{\lambda_1 I, \cdots, \lambda_\nu I\} > 0$ such that

$$\Psi + \bar{F}\Lambda\bar{F}^T + \bar{E}^T\Lambda^{-1}\bar{E} < 0 \qquad \text{A.9}$$

By Schur complement, Eq. A.9 is equivalent to Eq. 5.23. □

Proof of Lemma 5.3.2:

Note that $A(\psi)$, $A_d(\psi)$ and $B_w(\psi)$ have affine dependence on scheduling parameters ψ. Also note that the matrix inequalities in Eqs. 5.11 - 5.13 have affine dependence on A, A_d and B_w. Then with $A \to A(\psi)$, $A_d \to A_d(\psi)$ and $B_w \to B_w(\psi)$, inequalities in Eqs. 5.11 - 5.12 are convex combinations of the vertex inequalities, which are defined in terms of $(A(\mu_i), A_d(\mu_i), B_w(\mu_i))$ corresponding to all vertex values

$(\mu_i, i = 1,...,r)$ of the parameter vector ψ. Consequently if Eqs. 5.11 - 5.13 hold for every $(A(\mu_i), A_d(\mu_i), B_w(\mu_i))$, $i = 1,...,r$, they will hold for all $A(\psi)$, $A_d(\psi)$ and $B_w(\psi)$ with ψ varying in the polytope of vertices $\mu_1, \mu_2, ..., \mu_r$. In addition, following the proof in reference ([37, 44]), if inequalities in Eqs. 5.11 - 5.12 hold for all possible $A(\psi)$, $A_d(\psi)$ and $B_w(\psi)$ for any ψ as has been noted, there exists a common (scheduling-parameter-independent) Lyapunov-Krasovskii functional $V(x(t))$ such that $\dot{V}(x(t)) < 0$ and $\|o(t)\|_2 < \gamma \|w(t)\|_2$. This implies that the closed-loop system is asymptotically stable and the H_∞ performance is satisfied. □

Appendix B

Apply Cone Complementarity Linearization Method to Solve Matrix Inequalities in Chapter 5

Following a cone complementarity linearization method used in references ([45, 37]), the nonconvex feasibility problem characterized by the matrix inequalities in Eqs. 5.18 - 5.19, which include two forms of nonlinearity L_1^2 and $L_1 S^{-1} L_1$, is converted to the following minimization problem subject to Linear Matrix Inequalities:

Minimize $Trace(DT + L_1 J + SH + D_1 T_1)$ subject to

$$L_1 > 0,\ D > 0,\ D_1 > 0,\ \begin{bmatrix} M_{11} & M_{12} & N_1 \\ * & M_{22} & N_2 \\ * & * & D \end{bmatrix} \geq 0 \qquad \text{B.1}$$

$$\begin{bmatrix} T & J \\ J & H \end{bmatrix} > 0,\ \begin{bmatrix} D & I \\ I & T \end{bmatrix} \geq 0,\ \begin{bmatrix} L_1 & I \\ I & J \end{bmatrix} \geq 0,\ \begin{bmatrix} S & I \\ I & H \end{bmatrix} \geq 0,\ \begin{bmatrix} T_1 & J \\ J & I \end{bmatrix} > 0,\ \begin{bmatrix} D_1 & I \\ I & T_1 \end{bmatrix} \geq 0 \qquad \text{B.2}$$

$$\begin{bmatrix} \Gamma_{11} & \Gamma_{12} & -N_1 & 0 & \begin{bmatrix} -L_1 & -U^T \end{bmatrix} & \bar{\tau} L_2^T \\ * & \Gamma_{22} & A_d L_1 - N_2 & BU & 0 & \bar{\tau} L_3^T \\ * & * & -W & 0 & 0 & 0 \\ * & * & * & -\gamma^2 D_1 & \begin{bmatrix} L_1 & U^T \end{bmatrix} & 0 \\ * & * & * & * & -I & 0 \\ * & * & * & * & * & -\bar{\tau} S \end{bmatrix} < 0 \qquad \text{B.3}$$

Then an iterative algorithm given below is used to find a feasible solution to the matrix inequalities in Eqs. 5.18 - 5.19, from which a suboptimal maximum of $\bar{\tau}$ (and a suboptimal minimum of γ) can also be obtained. Iterative Algorithm is given as follows:

i) Choose a sufficiently small initial $\bar{\tau} > 0$ (and choose a sufficiently large initial $\gamma > 0$) such that there exists a feasible solution to Eqs. B.1 - B.3. Set $\bar{\tau}_{s0} = \bar{\tau}$ (set $\gamma_{s0} = \gamma$).

ii) Find a feasible set ($L_1^0, L_2^0, L_3^0, M_{11}^0, M_{12}^0, M_{22}^0, N_1^0, N_2^0, W^0, S^0, U^0, D^0, T^0, J^0,$ H^0, D_1^0, T_1^0) satisfying Eqs. B.1 - B.3. Set $k = 0$.

iii) Solve $(L_1, L_2, L_3, M_{11}, M_{12}, M_{22}, N_1, N_2, W, S, U, D, T, J, H, D_1, T_1)$ for the following LMI problem,

Minimze (subject to Eqs. B.1 - B.3)

$$Trace(D^k T + T^k D + L_1^k J + J^k L_1 + S^k H + H^k S + D_1^k T_1 + T_1^k D_1)$$

Set $D^{k+1} = D, T^{k+1} = T, L_1^{k+1} = L_1, J^{k+1} = J, S^{k+1} = S, H^{k+1} = H, D_1^{k+1} = D_1, T_1^{k+1} = T_1$

iv) If conditions in Eqs. 5.18 - 5.19 are satisfied, then set $\bar{\tau}_{s0} = \bar{\tau}$ (set $\gamma_{s0} = \gamma$) and return to Step ii) after increasing $\bar{\tau}$ (decreasing γ). If conditions in Eqs. 5.18 - 5.19 are not satisfied within a specified number of iterations, say $k_{\max}$, then exit. Otherwise, set $k = k + 1$ and go to Step iii).

For the inequalities in Eq. 5.23, we can find a feasible solution by applying a similar procedure.

Appendix C

Actuator Amplitude Saturation Compensation Design

In the following, we describe in details this control-reallocation-based saturation compensation, which is applied in simulations when needed. We have observed that without this saturation compensation, closed-loop systems may become unstable if control inputs are forced to stay within their physical amplitude limitations. On the other hand, we can imagine that if the required control actuation is so large that both δ_f and δ_c will get saturated even after control reallocation, then additional saturation compensation techniques, e.g., anti-windup based saturation compensation, may be needed; but this is not the case in the dissertation.

Let $\dot{w}_d$ and $\dot{q}_d$ denote the $\dot{w}$ and $\dot{q}$ values achieved by δ_f and δ_c if no actuation limitation exists. When either δ_f or δ_c gets saturated, we derive the updated (reallocated) δ_f and δ_c by minimizing the following metric,

$$D = \left(\dot{w} - \dot{w}_d\right)^2 + \left(\dot{q} - \dot{q}_d\right)^2 \qquad \text{C.1}$$

From Eq. C.1, we can see that when the metric D is minimized, $\dot{w}$ and $\dot{q}$ will approach $\dot{w}_d$ and $\dot{q}_d$ respectively, i.e., the controlled variables, $\dot{w}$ & $\dot{q}$, and hence w & q will recover to the values when there is no actuation limitation. Consequently, there will

be no or minimal performance degradation due to control saturation by reallocating the control effort between δ_f and δ_c to minimize the metric in Eq. C.1.

For the simplicity of explanation, we rewrite the dynamic equations of w and q into a compact form as follows,

$$\begin{aligned} \dot{w} &= k_1(w,q) + a_{11}\delta_f + a_{12}\delta_c \\ \dot{q} &= k_2(w,q) + a_{21}\delta_f + a_{22}\delta_c \end{aligned} \tag{C.2}$$

where, according to Eq. 2.27 and Eq. 2.30,

$$\begin{bmatrix} k_1(w,q) \\ k_2(w,q) \end{bmatrix} = M_I^{-1} \cdot (A_I \begin{bmatrix} w \\ q \end{bmatrix} + F_{grav}^{\Lambda} + F_{plane}^{\Lambda} \begin{bmatrix} 1 \\ L \end{bmatrix}) \tag{C.3}$$

$$\begin{bmatrix} a_{11} & a_{12} \\ a_{21} & a_{22} \end{bmatrix} = M_I^{-1} \cdot B_I \tag{C.4}$$

Now suppose δ_f gets saturated first at the limit value $\overline{\delta}_f$, we design the compensation to adjust δ_c, i.e., reallocate control δ_c to minimize the metric D in Eq. C.1, which is achieved by solving δ_c from $\frac{\partial D}{\partial \delta_c} = 0$. Noting that $\dot{w}_d$ and $\dot{q}_d$ do not depend on the adjusted δ_c, i.e., $\frac{\partial \dot{w}_d}{\partial \delta_c} = 0$ and $\frac{\partial \dot{q}_d}{\partial \delta_c} = 0$, we have,

$$\begin{aligned}&\frac{\partial D}{\partial \delta_c} = 0 \Rightarrow 2\left(\dot{w} - \dot{w}_d\right)\frac{\partial \dot{w}}{\partial \delta_c} + 2(\dot{q} - \dot{q}_d)\frac{\partial \dot{q}}{\partial \delta_c} = 0 \\ &\Rightarrow (k_1(w,q) + a_{11}\overline{\delta}_f + a_{12}\delta_c - \dot{w}_d)\cdot a_{12} \\ &\quad + (k_2(w,q) + a_{21}\overline{\delta}_f + a_{22}\delta_c - \dot{q}_d)\cdot a_{22} = 0\end{aligned} \tag{C.5}$$

which gives,

$$\begin{aligned}\delta_c = &\frac{(\dot{w}_d - k_1(w,q) - a_{11}\overline{\delta}_f)\cdot a_{12}}{a_{12}^2 + a_{22}^2} \\ &+ \frac{(\dot{q}_d - k_2(w,q) - a_{21}\overline{\delta}_f)\cdot a_{22}}{a_{12}^2 + a_{22}^2}\end{aligned} \tag{C.6}$$

If δ_c gets saturated first, the updated value of δ_f can be derived in a similar way as shown below,

$$\begin{aligned}\delta_f = &\frac{(\dot{w}_d - k_1(w,q) - a_{12}\overline{\delta}_c)\cdot a_{11}}{a_{11}^2 + a_{21}^2} \\ &+ \frac{(\dot{q}_d - k_2(w,q) - a_{22}\overline{\delta}_c)\cdot a_{21}}{a_{11}^2 + a_{21}^2}\end{aligned} \tag{C.7}$$

In the special case, when both δ_c and δ_f get saturated at the same time, we determine to keep δ_c at the limit value while adjusting δ_f to approximate desired state derivative values to the most extent. The compensation algorithm proves effective as shown in simulations of the dissertation.

Appendix D

System Parameters for Numerical Simulations

The table below lists the system parameter values used for numerical simulations in this dissertation. The table is originally from [1].

Parameter	Description	Value and Units
g	Gravitational acceleration	$9.81\ \mathrm{ms}^{-2}$
m	Density ratio	2
n	Fin effectiveness ratio	0.5
R_n	Cavitator radius	0.0191 m
R	Vehicle radius	0.0508 m
L	Length	1.8 m
V	Velocity	$75\mathrm{ms}^{-1}$
σ	Cavitation number	0.03
C_{x0}	Lift coefficient	0.82

VITA

Xiaofeng Mao

Xiaofeng Mao received his BE degree in Structural Mechanics in June 2001, and MS degree in Control Theory and Control Application in June 2004 from the Department of Mechanics and Engineering Science at Beijing University. In Aug. 2005, he was enrolled in the graduate program in Mechanical Engineering at the Pennsylvania State University and began to pursue his PhD degree. His research interests include system modeling, nonlinear and robust control theory & application, system identification and fault diagnosis of electric systems.